UNIVERSIDADE FEDERAL DO CEARÁ
CENTRO DE TECNOLOGIA
DEPARTAMENTO DE ENGENHARIA METALÚRGICA E DE MATERIAIS
PROGRAMA DE PÓS-GRADUAÇÃO EM ENGENHARIA E CIÊNCIA DE
MATERIAIS

JORGE LUIZ CARDOSO

EVALUATION OF THE PRECIPITATION OF SECONDARY PHASES ON CO_2 ENVIRONMENT CORROSION RESISTANCE OF AUSTENITIC AND SUPER AUSTENITIC STAINLESS STEELS

FORTALEZA-CE
2016

JORGE LUIZ CARDOSO

JORGE LUIZ CARDOSO

EVALUATION OF THE PRECIPITATION OF SECONDARY PHASES ON CO$_2$ ENVIRONMENT CORROSION RESISTANCE OF AUSTENITIC AND SUPER AUSTENITIC STAINLESS STEELS

Thesis submitted to the Graduate Program in Materials Science and Engineering of the Federal University of Ceará as a partial requirement for the degree of Doctor in Materials Science and Engineering.
Concentration area: Processes of transformation and degradation of materials

Advisor: Prof. Dr. Marcelo José Gomes da Silva.
Co-advisor: Prof. Dr. Pedro de Lima Neto.

FORTALEZA-CE
2016

JORGE LUIZ CARDOSO

Evaluation of the precipitation of secondary phases on CO2 environment
corrosion resistance of austenitic and super austenitic stainless steels

Tese apresentada ao Programa de
Pós-Graduação em Engenharia e
Ciência de Materiais do
Departamento de Engenharia
Metalúrgica e de Materiais da
Universidade Federal do Ceará,
como parte dos requisitos
necessários para a obtenção do
título de Doutor em Engenharia e
Ciência de Materiais.
Área de concentração: Processos de
Transformação e Degradação dos
Materiais.

Aprovado em: 31/ 3 / 2016.

BANCA EXAMINADORA

_____
Prof. Marcelo José Gomes da Silva (Orientador)
Universidade Federal do Ceará (UFC)

_____
Prof. Hamilton Ferreira Gomes de Abreu
Universidade Federal do Ceará (UFC)

_____
Prof. Pedro de Lima Neto
Universidade Federal do Ceará (UFC)

_____
Prof. Sérgio Souto Maior Tavares
Universidade Federal Fluminense (UFF)

_____
Prof. Juan Manuel Pardal
Universidade Federal Fluminense (UFF)

To my grandmother Maria dos Anjos Cardoso who passed away last year.

ACKNOWLEDGMENTS

Das Schönste, was wir erleben können, ist das Geheimnisvolle
(The most beautiful thing we can experience is the mystery)
Albert Einstein

ABSTRACT

Austenitic stainless steels are widely used in several applications including the manufacture of pipelines for the oil and gas industry. This work discusses the corrosion behavior of austenitic and super austenitic stainless steels in CO_2-containing environments. The steels used in this work were the AL-6XN PLUS™ (UNS Designation N08367) and 904L (UNS Designation N08904) super austenitic stainless steels. Two conventional austenitic stainless steels, 316L (UNS S31600/ S31603) and 317L (UNS S31703) were also used for comparison purposes. Potentiodynamic polarization measurements were taken in CO_2-saturated synthetic oil field formation water, deaerated with nitrogen to simulate some conditions in the pre-salt region. Potentiostatic measurements were also carried out to evaluate the corrosive level of the solution without the presence of CO_2. Pressurized experiments using autoclave in CO_2-containing environment and in synthetic air environment were also conducted to evaluate the corrosion resistance of the alloys when pressure and temperature act together. Heat treatments at high temperatures between 600 °C and 760°C in different ranges of time were also conducted to evaluate the possible sigma phase precipitation and its effect on the corrosion resistance. The AL-6XN PLUS™ and 904L super austenitic stainless steels showed a good performance in CO_2-containing environment. The AL-6XN PLUS™ steel also exhibited the best performance in the pressurized experiments. The conventional 316L and 317L steels showed susceptibility to pitting and crevice corrosion. The results showed that the conventional alloys are not suitable for the use in CO_2-containing environment under severe conditions. Pitting potential of the 316L alloy was affected by the pH of the solution in CO_2-saturated solution. No sigma phase precipitated in the heat treatments for the range of time used indicating that its precipitation kinetics in austenitic stainless steels is very slow. This result is an advantage when working with austenitic stainless steels for long periods of exposure at high temperatures.

Key words: materials science, corrosion resistance, austenitic stainless steel

RESUMO

Os aços inoxidáveis austeníticos e super austeníticos são amplamente utilizados na fabricação de tubulações na industria de petróleo e gás. Esse trabalho discute o comportamento da corrosão de aços inoxidáveis austeníticos e super austeníticos em meio contendo CO_2. Os aços usados nesse trabalho foram os aços super austeníticos AL-6XN PLUS™ (Designação UNS N08367) e 904L (Designação UNS N08904). Dois aços austeníticos convencionais, 316L (UNS S31600/ S31603) e 317L (UNS S31703), também foram usados para comparação. Foram realizadas medidas de polarização potenciodinâmica em água artificial de formação de poço de petróleo saturada com CO_2 e desaerada com nitrogênio para simular algumas condições do pré-sal. Foram também realizadas medidas potenciostáticas para avaliar o nível corrosivo da solução sem a presença de CO_2. Experimentos pressurizados usando autoclaves em meio contendo CO_2 e ar sintético também foram realizados para avaliar a resistência à corrosão das ligas quando pressão e temperatura agem juntas. Foram realizados tratamentos térmicos em altas temperaturas entre 600 °C e 760 °C em diferentes faixas de tempo para avaliar a formação de fase sigma e seu efeito na resistência à corrosão. Os aços super austeníticos AL-6XN PLUS™ e 904L mostraram uma boa performance em meio contendo CO_2. O aço AL-6XN PLUS™ também exibiu uma boa performance nos experimentos pressurizados. Os aços convencionais 316L e 317L apresentaram susceptibilidade à corrosão por pites e frestas. Os resultados mostraram que os aços convencionais não são apropriados para uso em meio contendo CO_2 sob condições severas. O potencial de pite do aço 316L foi afetado pelo pH da solução em meio saturado com CO_2. Não houve precipitação de fase sigma nos tratamentos térmicos para as faixas de tempo usadas indicando que sua cinética de precipitação em aços inoxidáveis austeníticos é muito lenta. Esse resultado é uma vantagem ao se trabalhar com aço inoxidáveis austeníticos em logos períodos de exposição em altas temperaturas.

Palavras-chave: ciência dos materiais, resistência à corrosão, aço inoxidável austenítico

LIST OF FIGURES

LIST OF TABLES

LIST OF ABBREVIATIONS

AISI - American Iron and Steel Institute

ASTM - American Society for Testing and Materials

BCC - Body-Centered Cubic

BCT - Body-Centered Tetragonal

CAPES - Coordenação de Aperfeiçoamento de Pessoal de Nível Superior (Improvement Coordination of Higher Education)

CCS - Carbon Capture and Storage

CNPq - Conselho Nacional de Desenvolvimento Científico e Tecnológico (National Council for Scientific and Technological Development)

COPPE - Instituto Alberto Luiz Coimbra de Pós-Graduação e Pesquisa de Engenharia (Alberto Luiz Coimbra Institute of Graduate Studies and Research in Engineering)

CP - Cathodic Protection

CPT - Critical Pitting Temperature

CRA - Corrosion Resistant Alloy

EBSD - Electron Backscatter diffraction

EDS - Energy-Dispersive X-ray Spectroscopy

FCC - Face-Centered Cubic

FH - Fachhochschule (University of Applied Sciences)

FINEP - Financiadora de Estudos e Projetos (Funding of Studies and Projects)

Funcap - Fundação Cearense de Apoio ao Desenvolvimento Científico e Tecnológico (Cearense Foundation for the Support of Scientific and Technological Development)

GB - Grain Boundary

ICDD - International Centre for Diffraction Data

IFCE - Instituto Federal do Ceará (Federal Institute of Ceará)

IPDI - Instituto de Pesquisa Desenvolvimento e Inovação (Institute of Research Development and Innovation)

JCPDS - Joint Committee for Powder Diffraction Data

LNLS - Laboratório Nacional de Luz Synchrotron (Brazilian Synchrotron Light Laboratory)

LACAM - Laboratório de Caracterização de Materiais (Materials Characterization Laboratory)

LPC - Laboratório de Pesquisa em Corrosão (Research Laboratory of Corrosion)

OCP - Open Circuit Potential

PETROBRAS - Petróleo Brasileiro (Brazilian Petroleum Corporation)

PRE_N - Pitting Resistance Equivalent Number

SAE - Society of Automotive Engineers

$SC-CO_2$ - Super Critical CO_2

SEM - Scanning Electron Microscopy

SMS - Surface Measuring System

TP - Triple Point

TTP - Time–Temperature–Precipitation

TTT - Time–Temperature–Transformation

TU BAF - Technische Universität Berkadademie Freiberg (Freiberg University of Mining and Technology)

UFC - Universidade Federal do Ceará (Federal University of Ceará)

UFFluminense - Universidade Federal Fluminense (Fluminense Federal University)

UFRJ - Universidade Federal do Rio de Janeiro (Federal University of Rio de Janeiro)

UNS - Unified Numbering System

wt - Weight

XRD - X-Ray Diffraction

CONTENTS

1   INTRODUCTION

The discoveries made in the pre-salt are among the world's most important in the past decade. The pre-salt province comprises large accumulations of excellent quality, high commercial value light oil. A reality that puts Brazil in a strategic position to meet the great global demand for energy (PETROBRAS, 2015).The discovery of the pre-salt layer also brings several technological challenges for the oil and gas exploration below this layer. In 1974 the search of self-sufficiency in the oil industry has become a state policy. Due to the dependence on imported oil and the previous year's price range, Brazil assumed the challenge of the race to the sea, which led Petrobras to explore the little-known Campos Basin (COPPE, 2011). The era of oil can be considered as the second industrial revolution, once that 90% of oil is used for energy purposes, whether in thermoelectric plants, whether as a fuel for means of transport or industrial purposes. From the remaining 10%, the products that supply industries are extracted. Due to the increase of oil consumption, new deposits of oil began to be explored. These new deposits are located at depths that exceed seven thousand meters and have a total capacity of reservoirs capable of reaching 12 billion barrels of oil and natural gas (COPPE, 2011). The oil of these new reservoirs possesses a good quality but in the pre-salt region, the operating environment is very hostile. This fact is due to high temperatures, pressures, presence of corrosive gases such as carbon dioxide (CO_2) and hydrogen sulfide (H_2S). These gases in contact with water from these reservoirs accelerate the corrosion of metallic materials used for the oil exploration in the pre-salt region (COPPE, 2011). The difficulty in adding corrosion inhibitors for carbon steel pipes in offshore oil extraction at great depths has led to increased use of corrosion resistant alloys (SMITH, 2002). Of all types of corrosion, localized corrosion (pitting) is the most common in marine waters and more difficult to control. Currently, the oil and gas industry is concerned about the environmental impact caused by oil leaks in the marine ecosystem.

There are two types of technological challenges for the exploration of oil and gas contained in the pre-salt region . The vertical challenge that consists in drilling the well as far as the reservoir, crossing water layers, sediment and salt. Each layer with a different behavior at temperatures ranging from 50 °C to 150 °C under high pressures and corrosive gases. The way back to the surface must also be considered, once that all the oil and natural gas extracted from the well will be transported through the pipelines and the material from which the pipes are made must resist all adverse conditions to avoid oil leaks. Figure 1 depicts the vertical

challenge. The second challenge is horizontal and consists in the transportation of oil and gas from the production area to the coast localized about 300 km away from the well location.

Figure 1 - Vertical challenge for the oil extraction from the pre-salt layer.
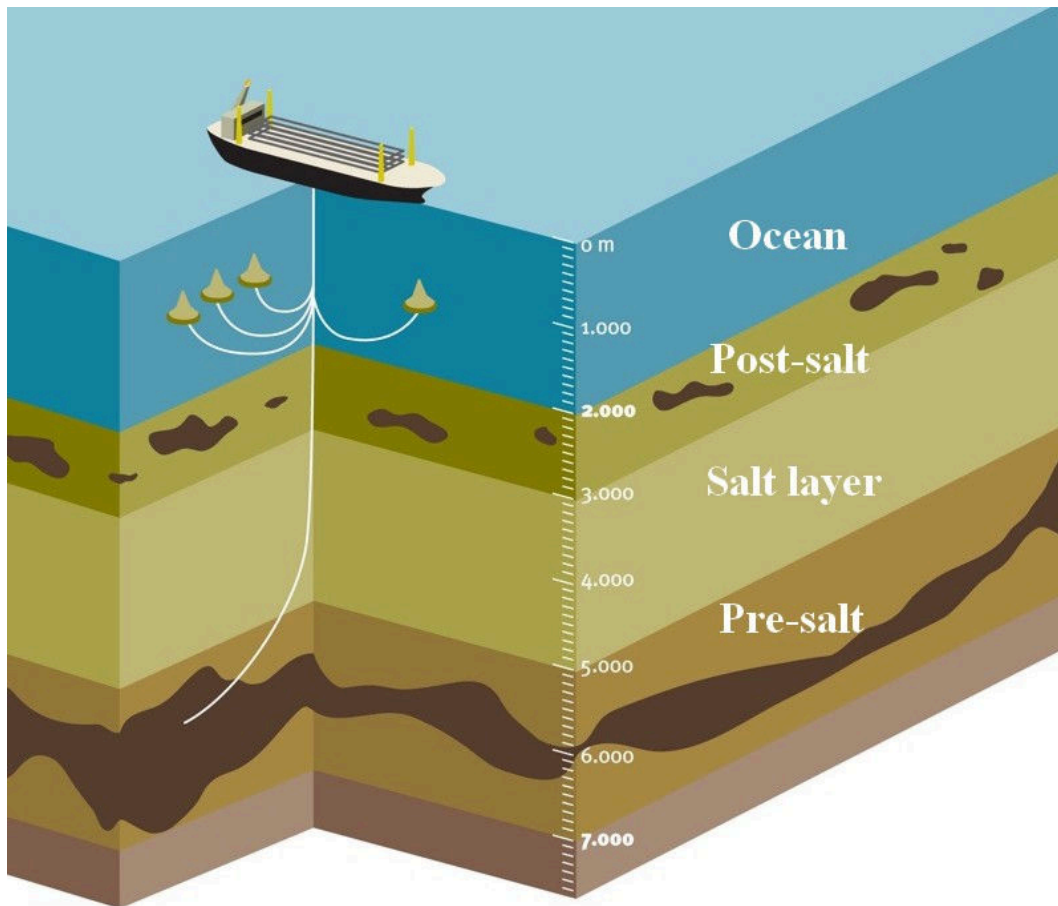
In summary, it is a set of problems that begins with the depth of the well, passing by the coating when drilling into soft sediments through the salt layer to reach a very high temperature and pressure environment saturated with corrosive gases already mentioned (COPPE, 2011).

The greater the depth of the region under the ocean, the higher the pressure and the temperature. Another challenge and perhaps the most crucial is to develop materials that could resist the combination of temperatures (around 150 °C) with the effect of pressures around 400 bar which is equivalent to 400 times the atmospheric pressure in which we live.

These same materials have also to resist the corrosive action of CO_2 and H_2S present in a chemically hostile environment where nothing is static.

Earlier studies have shown that the corrosion in the pre-salt region occurs due to the presence of corrosive gases such as carbon dioxide and hydrogen sulphide in aqueous medium and combined with the factors already mentioned, it becomes a challenge in selecting the correct materials for the oil and gas exploration, once that many materials currently used for these operational conditions do not resist the corrosive attack.

It is necessary to understand the CO_2 corrosion mechanism of corrosion resistant alloys (stainless steels, Ni alloys) for the utilization in pipes in the pre-salt region to maintain the operational safety by increasing production and reducing maintenance costs.

The study of the metallurgical properties of these materials mainly when subjected to high temperatures for long periods of time is also an important feature to be understood. When heat treated at high temperatures, deleterious phases can precipitate in austenitic stainless steels. These phases decrease the corrosion resistance and also some mechanical properties.

2   OBJECTIVES

The objectives of this work were divided in general and specific objectives.

2.1   General Objectives

The aim of this work was to evaluate and compare the corrosion resistance and the influence of heat treatments on austenitic and superaustenitic stainless steels in CO_2-saturated aqueous medium for the utilization in the industrial production sector, refining and storage of oil and natural gas. The work also aimed to evaluate the behavior of these alloys in CO_2 and synthetic air pressurized environments.

2.2   Specific Objectives

Specifically, the objectives were to evaluate the effect of alloying elements (Cr, Mo, Ni) on CO_2 corrosion resistance as well as the effect of heat treatments and their influence on corrosion resistance of austenitic and superaustenitic stainless steels focusing:

- ✓ Computational thermodynamic study for each studied alloy;

- ✓ Heat treatments according to thermodynamic simulations for obtaining deleterious phases;

- ✓ Evaluate the influence of heat treatments on CO_2 corrosion resistance by using electrochemical techniques in order to verify if the corrosion resistance of the heat treated alloys differs from the corrosion resistance of the alloys in the as-received condition.

- ✓ Evaluate the corrosion resistance of the studied alloys in CO_2 and synthetic air pressurized environments by using pressure of the cited gases verifying the state of the alloys surfaces after the pressurized experiments.

3   MOTIVATION

On scientific grounds, the study of the effect of alloying elements as Cr, Mo and Ni on CO_2 corrosion resistance may provide important information about the passive film behavior in CO_2-saturated aqueous medium. The study of CO_2 corrosion mechanism on austenitic stainless steels is an important subject to be understood. The understanding of its mechanism may enable the best choice of the materials that will be used in oil and gas industry in pressurized environments.

An understanding of the precipitation kinetics of sigma phase may enable the best choice of the materials used in oil and gas industry when these materials are exposed to high temperatures. Sigma phase precipitation is slow in austenitic stainless steels making this an advantage when using this class of material at high temperatures for long period of time.

In the technological context, the understanding of the pressure mechanism caused by gases such as CO_2 may enable to create new technologies to generate more resistant materials (so-called corrosion resistant alloys) and improve their properties.

Super austenitic stainless steels are nowadays used in equipments that work at high temperatures and they may eventually substitute the conventional austenitic stainless steels in some applications where the conditions (temperature, pressure, medium) are very aggressive.

Regarding the cost versus benefits, austenitic stainless steels are the best option in many cases because they combine low maintenance costs and better performance in corrosive media. This may lead to an increase in operation time and also may increase the time for maintenances.

Austenitic stainless steels are environmentally friendly because they are recyclable and have greater durability. The use of materials that ensure the integrity of the environment is also an ecological role. When a pipe is drilled by pitting corrosion, for example, harmful substances may leak to the environment. An understanding of the corrosion resistance and metallurgical properties of the alloys used in oil industry is crucial to keep the environment safe.

4 LITERATURE REVIEW

4.1 Stainless steels

Stainless steels, in metallurgy, are steel alloys with a minimum of 12 % (in weight %) chromium content. They are also known as inox steel or simply inox from the French word "*inoxydable*". The addition of chromium increases the resistance to oxidation and corrosion of steels by forming thin films of chromium oxide on the steel surface. This thin film isolates the metallic substrate from the oxidant environment (COSTA & SILVA, 1988). They are also defined as alloys of iron and chromium containing another alloying elements such as nickel and molybdenum and other elements that present the physical-chemical properties superior to ordinary steels (COSTA & SILVA, 1988). Due to its corrosion resistance, such steels possess an important role in engineering. They also have mechanical properties at high temperatures (in the case of austenitic stainless), which makes these type of steels good materials for industrial applicability (COSTA & SILVA, 1988).

The corrosion resistance of stainless steels is associated with the passivation phenomenon, which consists in forming a layer of mixed oxides (from Fe, Cr and other alloying elements), as well as the dissolution of this layer in the corrosive environment. The formation of this layer (or not), its impermeability as well as its rate of dissolution in the corrosive environment will control the corrosion resistance of the material in the considered aggressive environment (COSTA & SILVA, 1988).

The expression "stainless steel" gives us an erroneous idea of a material that is not destroyed in aggressive media. In fact, this type of steel is more resistant to corrosion in aggressive media when compared with other types of steels. The stainless steels are classified according to their microstructure. The main types are: martensitic (including precipitation hardening steels), ferritic, austenitic and duplex, consisting of a mixture of ferrite and austenite (COSTA & SILVA, 1988).

Stainless steels produced in the United States are identified in three general ways: (I) by the Unified Numbering System (UNS) numbers developed by the American Society for Testing and Materials (ASTM) and the Society of Automotive Engineers (SAE) for all commercial metals and alloys, (II) by the American Iron and Steel Institute (AISI) numbering system, and (III) by names based on compositional abbreviations, proprietary designations, and trademarks (SEDRIKS, 1996).

4.1.1 *Austenitic stainless steels*

Austenitic stainless steels were invented in Essen, Germany, in the beginning of the 20th century and represent 2/3 of the total stainless steel world production (PADILHA, 2002). They play a very important role in the modern world because they correspond to most of the world production of stainless steel (OLIVEIRA SILVA, 2005). The popularity of these steels is related to high corrosion resistance in several environments. This characteristic is due to the formation of a passive film of chromium oxide. However, their mechanical characteristics are relatively low (GONTIJO *et al*, 2008).

Austenitic stainless steels are non-magnetic materials with face-centered cubic structure (FCC) and cannot be hardened by heat treatments. They are very ductile and possess excellent weldability. They can be classified as stable austenitic (presenting an austenitic structure even after a large cold deformation) and metastable austenitic (those that transform to martensite structure when subjected to cold deformation) (COSTA & SILVA, 1988).

They possess wide applications, such as in the chemical, pharmaceutical and food industry, biotechnology, bioengineering and nuclear applications. They are also used in cutlery, table ware, sinks, lifts coatings and other applications.

In certain environments, especially those containing chloride ions, these steels are susceptible to a form of localized corrosion called pitting corrosion. The addition of alloying elements such as molybdenum has the role of reducing the susceptibility to this form of corrosion, since this element incorporates into the passive film by the formation of complex oxides in different oxidation states (PADILHA, 2002).

Table 1 shows the standard composition for the austenitic series classified according to the American Iron and Steel Institute (AISI) (SEDRIKS, 1996).

Table 1 - Composition (in weight %) of the 300 series of austenitic stainless steels.

Type	UNS designation	C	Mn	Si	Cr	Ni	Mo	N	Others
AISI 201	S20100	≤0.15	5.50-7.50	≤1.00	16.00-18.00	3.50-5.50	-	0.25	-
AISI 202	S20200	≤0.15	7.50-10.0	≤1.00	17.00-19.00	4.0-6.0	-	0.25	-
AISI 205	S20500	0.12-0.25	14.0-15.5	≤1.00	16.50-18.00	1.0-1.75	-	0.32-0.40	-
AISI 301	S30100	≤0.15	≤2.00	≤1.00	16.00-18.00	6.0-8.0	-	-	-
AISI 302	S30200	≤0.15	≤2.00	≤1.00	17.00-19.00	8.0-10.0	-	-	-
AISI 303	S30300	≤0.15	≤2.00	≤1.00	17.00-19.00	8.0-10.0	0.6	-	-
AISI 304	S30400	≤0.08	≤2.00	≤1.00	18.00-20.00	8.0-10.5	-	-	-
AISI 304H	S30409	0.04-0.10	≤2.00	≤1.00	18.00-20.00	8.0-10.5	-	-	-
AISI 304L	S30403	≤0.03	≤2.00	≤1.00	18.00-20.00	8.0-12.0	-	-	-
AISI 304N	S30400	≤0.08	≤2.00	≤1.00	18.00-20.00	8.0-10.5	-	0.10-0.16	-
AISI 304LN	S30451	≤0.03	≤2.00	≤1.00	18.00-20.00	8.0-12.0	-	0.10-0.16	-
AISI 308	S30800	≤0.08	≤2.00	≤1.00	19.00-21.00	10.0-12.0	-	-	-
AISI 309	S30900	≤0.20	≤2.00	≤1.00	22.00-24.00	12.0-15.0	-	-	-
AISI 310	S31000	≤0.25	≤2.00	≤1.00	24.00-26.00	19.0-22.0	-	-	-
AISI 316	S31600	≤0.08	≤2.00	≤1.00	16.00-18.00	10.0-14.0	2.0-3.0	-	-
AISI 316H	S31609	≤0.08	≤2.00	≤1.00	16.00-18.00	10.0-14.0	2.0-3.0	-	-
AISI 316L	S31603	≤0.03	≤2.00	≤1.00	16.00-18.00	10.0-14.0	2.0-3.0	-	-
AISI 316LN	S31653	≤0.03	≤2.00	≤1.00	16.00-18.00	10.0-14.0	2.0-3.0	0.10-0.16	-
AISI 316N	S31651	≤0.08	≤2.00	≤1.00	16.00-18.00	10.0-14.0	2.0-3.0	0.10-0.16	-
AISI 317	S31700	≤0.08	≤2.00	≤1.00	18.00-20.00	11.0-15.0	3.0-4.0	-	-
AISI 317L	S31703	≤0.03	≤2.00	≤1.00	18.00-20.00	11.0-15.0	3.0-4.0	-	-
AISI 321	S32100	≤0.08	≤2.00	≤1.00	17.00-19.00	9.0-12.0	-	-	Ti≥5 x %C
AISI 321H	S32109	0.04-0.10	≤2.00	≤1.00	17.00-19.00	9.0-12.0	-	-	Ti≥5 x %C
AISI 347	S34700	≤0.08	≤2.00	≤1.00	17.00-19.00	9.0-13.0	-	-	Nb≥10 x %C
AISI 347H	S34709	0.04-0.10	≤2.00	≤1.00	17.00-19.00	9.0-13.0	-	-	1.0≥Nb≥10 x %C
654 SMO®	S32654	≤0.02	2.00-4.00	≤0.50	24.0-25.0	21.0-23.0	7.0-8.0	0.45-0.55	Cu = 0.30-0.60

(AISI = american iron and steel institute; UNS = unified numbering system).

Source: ASM Speciality Handbook: Stainless Steels, 1994.

4.1.1.1 Application of austenitic stainless steels

Austenitic stainless steels combine mechanical strength properties and corrosion resistance which make them excellent candidates for use in the oil refining process. From the 304 austenitic stainless steel arose the other austenitic steels as depicted in Figure 2. The scheme shows that the 316 and 317 austenitic steels are derived from the 304 austenitic steel by adding molybdenum to improve the pitting corrosion resistance. These steels are widely used in oil refinery components. The low carbon versions of austenitic stainless steels are designated by the letter L in the end of the number that identifies them. In these steels, the carbon content is reduced to prevent sensitization (carbide formation) to temperatures in the range of 425 °C-815 °C (COSTA & SILVA, 1988).

Figure 2 - Evolution of austenitic stainless steels derived from the 304 austenitic steel.

Source: Sedriks, 1996.
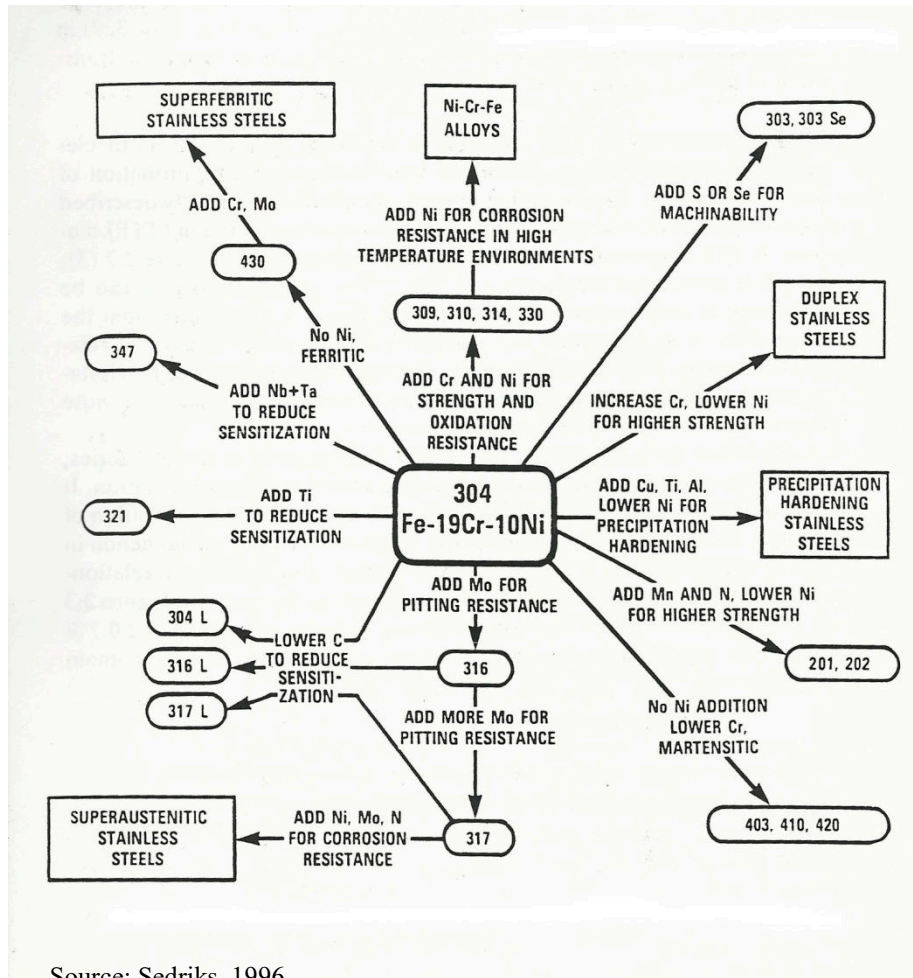
Below it follows a brief description of the 300 series of austenitic stainless steels studied in this work and their applications.

4.1.1.2 AISI 316L

316/316L alloy (UNS S31600/ S31603) is a chromium-nickel-molybdenum austenitic stainless steel developed to provide improved corrosion resistance to 304/304L alloy in moderately corrosive environments. It is often utilized in process streams containing chlorides or halides. The addition of molybdenum improves general corrosion and chloride pitting resistance. It also provides higher creep, stress-to-rupture and tensile strength at elevated temperatures. It is common practice for 316L to be dual certified as 316 and 316L. The low carbon chemistry of the 316L combined with an addition of nitrogen enables 316L to

meet the mechanical properties of the 316 (SPECIFICATION SHEET: ALLOY 316/316L, 2015).

Applications:

✓ Chemical and Petrochemical Processing, pressure vessels, tanks, heat exchangers, piping systems, flanges, fittings, valves and pumps
✓ Food and Beverage Processing
✓ Marine
✓ Medical
✓ Petroleum Refining
✓ Pharmaceutical Processing
✓ Power Generation, nuclear
✓ Pulp and Paper
✓ Textiles
✓ Water Treatment

4.1.1.3   AISI 317L

317L alloy (UNS S31703) is a low-carbon corrosion resistant austenitic chromium-nickel-molybdenum stainless steel. The high levels of these elements assure the alloy has superior chloride pitting and general corrosion resistance to the conventional 304/304L and 316/316L grades. The alloy provides improved resistance relative to 316L in strongly corrosive environments containing sulfurous media, chlorides and other halides. The low carbon content of 317L alloy enables it to be welded without intergranular corrosion resulting from chromium carbide precipitation enabling it to be used in the as-welded condition. With the addition of nitrogen as a strengthening agent, the alloy can be dual certified as 317L alloy (UNS S31700). (SPECIFICATION SHEET: ALLOY 317/317L, 2015).

Applications:

✓ Air Pollution Control, flue gas desulfurization systems (FGDS)
✓ Chemical and Petrochemical Processing
✓ Explosives
✓ Food and Beverage Processing

✓ Petroleum Refining

✓ Power Generation, condensers

✓ Pulp and Paper

4.1.2 Super austenitic stainless steels

Historically, super austenitic stainless steels were developed in the early 1980s. Therefore, there was no accurate definition about them until today. Sedriks defines them as high molybdenum steels (SEDRIKS, 1996). Sequeira defines them as steels with high levels of chromium, molybdenum and nitrogen (SEQUEIRA, 2001). Superaustenitic stainless steels are derived from the 317 austenitic stainless steel by increasing the content of chromium, nickel, molybdenum and nitrogen to increase the corrosion resistance, according to the scheme of Figure 2. It is expected that this new class of steel has better performance in corrosive environments when compared with the 300 series of austenitic stainless steels. Currently super austenitic stainless steels are used in components that require high temperatures, such as boilers, super heaters, chemical reactors. They possess high levels of chromium, nickel, molybdenum and nitrogen. The iron content is around 50% (PADILHA, 2002). These levels of alloying elements give them a good performance on the pitting corrosion resistance.

4.1.2.1 AL-6XN PLUS™ Alloy

AL-6XN PLUS™ alloy is an enhanced version of the standard AL-6XN® alloy. Both satisfy the composition requirements of UNS N08367, but the AL-6XN PLUS alloy contains a greater concentration of alloying elements (Cr, Mo, and N) which promote corrosion resistance. They are also known for having up to 6% molybdenum (ALLEGHENY-LUNDLUM, 2002).

Applications:

✓ Air Pollution Control Coal-fired power plant FGD systems

✓ Chemical Processing Equipment

✓ Food and Beverage Process Equipment

✓ Mining - Coal mining wastewater brine treatment

✓ Offshore Oil and Gas Production

✓ Pharmaceuticals and Biotechnology

✓ Process equipment and piping systems

✓ Power Generation, condensers, pumps, feed-water heaters, piping systems

✓ Pulp and Paper

✓ Chlorine dioxide bleaching plants

✓ Seawater Treatment

✓ Desalination systems

4.1.2.2 904L Alloy

904L alloy (UNS N08904) is a superaustenitic stainless steel that is designed for moderate to high corrosion resistance in a wide range of process environments. The combination of high chromium and nickel content, coupled with additions of molybdenum and copper, assure good to excellent corrosion resistance. With its highly alloyed chemistry 25% nickel and 4.5% molybdenum, 904L provides good chloride stress corrosion cracking resistance, pitting and general corrosion resistance superior to 316L and 317L molybdenum enhanced stainless steels. 904L alloy was originally developed to withstand environments containing dilute sulfuric acid. It also offers good resistance to other inorganic acids such as hot phosphoric acid as well as most organic acids (SPECIFICATION SHEET: ALLOY 904L, 2015).

Applications:

✓ Air Pollution Control, scrubbers for coal-fired power plants

✓ Chemical Processing

✓ Metallurgical Processing, pickling equipment using sulfuric acid

✓ Oil and Gas Production — offshore process equipment

✓ Pharmaceutical Industry — process equipment

✓ Pulp and Paper — processing equipment

✓ Seawater and Brackish Water — condensers, heat exchangers and piping systems

4.1.3 Influence of alloying elements

Austenitic and super austenitic stainless steels possess high levels of alloying elements present in their chemical composition where each element added to the steel has its own characteristics that contribute to improvements in the material properties. The main alloying elements for stainless steels and their benefits are described below.

4.1.3.1 Chromium (Cr)

This alloying element is the main element in stainless steels. It is responsible for corrosion resistance and also responsible for the formation of a protective oxide layer which causes the passivity of stainless steels. The higher the chromium content, the greater the resistance to various forms of corrosion. The operational limit temperature also increases with increasing of chromium content as shown in Figure 3. When added to the alloy in high concentrations, even ensuring an increase in corrosion resistance, this element may have a harmful effect when the alloy undergoes heat treatments at high temperatures. This effect may be caused by the precipitation of deleterious phases such as sigma and chi phases. Chromium is also ferrite stabilizer (COSTA & SILVA, 1988).

Figure 3 - Influence of the chemical composition (in wt %), especially the Cr content, on the oxidation resistance of steels.
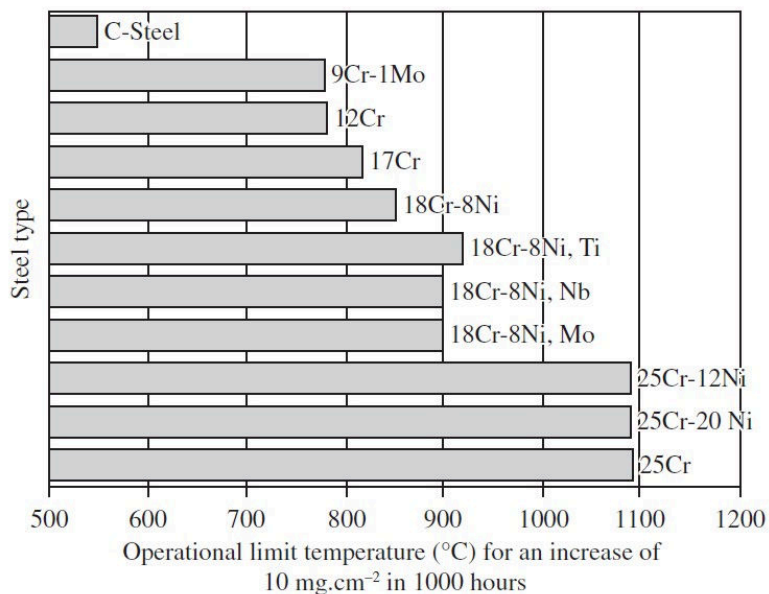
Source: Plaut, 2007

4.1.3.2 Molibdenum (Mo)

Like chromium, molybdenum is also ferrite stabilizer. When this element is dissolved in solid solution in the alloy, it promotes increased resistance to localized corrosion (pitting and crevice) in chloride containing media. This is due to greater stability of the passive film (SEDRIKS, 1996). For concentrations above 4%, there may be the possibility of formation of intermetallic compounds in stainless steels.

4.1.3.3 Nickel (Ni)

Unlike chromium and molybdenum, nickel is austenite stabilizer. Its function in stainless steels is to promote the balance of the elements to develop the desired microstructure. It is also responsible for delaying the formation of undesirable intermetallic compounds in austenitic stainless steels. Another function of nickel is to promote an increase on corrosion resistance. An economic disadvantage of using high nickel content in stainless steels is the fact that nickel has a high market value that undergoes several changes every year and has already reached very high values (GOMES SILVA, 2012). When the use of nickel in stainless steels becomes infeasible, one searches other alternatives that satisfy the technical and economic conditions of the engineering projects.

4.1.3.4 Nitrogen (N)

This element has several beneficial functions for stainless steels. Like nickel, nitrogen is also austenite stabilizer. Nitrogen also increases pitting corrosion resistance of stainless steels and it acts against the formation of harmful phases such as sigma and chi. In the austenite phase, this element has high solubility (GOMES SILVA, 2012). It is added in greater amounts in low carbon alloys to compensate for the loss of mechanical strength due to removal of carbon.

4.1.3.5 Other elements

Other elements possess positive and negative influence on stainless steels, such as manganese, copper and tungsten.

Manganese is austenite stabilizer that when combined correctly with nitrogen, promotes better resistance to wear and abrasion. It also improves the pitting corrosion resistance. When added to higher levels, it may decrease the corrosion resistance of the steel by increasing the formation of inclusions (GOMES SILVA, 2012).

Copper, when added in stainless steel, reduces corrosion rate in non-oxidizing media such as in sulfuric acid containing media. It is austenite stabilizer and can be added until a maximum content of 2% to avoid deleterious phases of high copper content (GOMES SILVA, 2012).

Tungsten promotes an increase on pitting corrosion resistance due to the increased stability of the passive film on the steel surface. Its addition in stainless steels should be done

in correct concentrations, as this element favors the formation of intermetallic compounds during cooling in the temperature range between 900 °C and 700 °C (GOMES SILVA, 2012).

4.2 Deleterious phases

Deleterious phases are phases that when precipitated on metallic materials decrease some mechanical properties and the corrosion resistance. The three intermetallic phases most frequently found in austenitic stainless steels are sigma, chi and Laves. However, other intermetallic phases and carbides can also occur during heat treatments (PADILHA, 2002). Precipitation of intermetallic phases from austenite is normally associated with undesirable consequences like matrix impoverishment of alloying elements such as chromium, molybdenum, and niobium as well as loss of ductility, toughness and corrosion resistance. (PADILHA, 2002).

Table 2 summarizes the main intermetallic phases formed in austenitic stainless steels.

Table 2 - The main intermetallic phases and types of steels in which they can precipitate as well as their crystallographic parameters.

Phase	Unit cell	Atoms/cell	Network Parameters (nm)	Composition	Occurrence
Sigma (σ)	BCT	30	a = 0,87-0,92; c= 0,4554-0,48	$(Fe,Ni)_x(Cr,Mo)_y$	AISI: 304, 304L, 316, 316L, 321, 347
Chi (χ)	BCC	58	a = 0,881-0,895	$(Fe,Ni)_{36}Cr_{12}Mo_{10}$	AISI: 316, 316L, 321
Laves (η)	hex.	12	a = 0,473-0,483; c = 0,772-0,786	Fe_2Mo; Fe_2Nb; FeTa; Fe_2Ti; Fe_2W	AISI: 316, 316L, 321, 347
G	BCC	116	a = 1,115-1,120	$Ni_{16}Nb_6Si7$; $Ni_{16}Ti_6Si7$; $(Ni,Fe,Cr)_{16}(Nb,Ti)_6Si7$	AISI: 308, 310S, 329, Fe-20Cr-25Ni-Nb
R	hex.	53 (159)	a = 1,090; c = 1,934	$Fe_{22}Mo_{18}Cr_{13}$; $(Fe,Ni)_{10}Cr5Mo_3Si_2$	Duplex Fe-22Cr-8Ni-3Mo; Superaustenitic UNSS32654; Maraging Fe-12Cr-9Ni-4Mo
Mu (μ)	Rhombohedral	13	a = 0,4762; c = 2,5015	$(Fe,Co)_7(Mo,W)_6$; $(Cr,Fe)_7(Mo)_2(Cr,Fe,Mo)_4$	Fe-17Cr-14Ni-6W; Fe-15Cr-40Ni-4W-2Mo-Al-Ti
γ'	FCC	4	a = 0,3565-0,3601	$(Ni,Co,Fe,Cr)3(Al,Ti)$	Iconel 800 and alloy A-286
γ''	BCT	8	a = 0,3624; c = 7406	Ni_3Nb	Iconel 718
η	hex.	8	a = 0,5109; c = 0,8299	Ni_3Ti	Iconel 800 super aged A-286
δ	Orthorhombic	8	a = 0,5116; b = 0,4259; c = 0,4565	Ni_3Nb	Iconel 718 super aged

Source: Padilha, 2002.

4.2.1   *Sigma phase (σ)*

Sigma phase is perhaps the most undesirable phase in austenitic steels and for this reason, the most studied one. It is an intermetallic compound of tetragonal unit cell (BCT), hard and non-magnetic (MURRAY, 2004). The precipitation of this phase is a serious problem when using austenitic steels at elevated temperatures, because this phase is rich in important alloying elements such as chromium and molybdenum. These elements are removed from the austenitic matrix and precipitated mainly on grain boundaries, especially on triple junctions, and on incoherent twin boundaries and intragranular inclusions leaving the austenite impoverished of these elements (PADILHA, 2002).

Sigma phase appears in several binary, ternary and quaternary systems such as Fe–Cr, Fe–Mo, Fe–V, Fe–Mn, Fe–Cr–Ni, Fe–Cr–Mo, Fe–Cr–Mn e Fe–Cr–Ni–Mo. Its precipitation in austenitic stainless steels occurs between 550 °C and 900 °C. The composition of sigma phase in austenitic stainless steels can be approximately written as: $(Fe, Ni)_3(Cr, Mo)_2$. Alloying elements such as chromium, manganese, molybdenum, tungsten, vanadium, silicon, titanium, niobium, and tantalum favors sigma phase formation, whereas nickel, cobalt, aluminum, carbon and nitrogen hinder its precipitation (PADILHA, 2002). Sigma phase precipitation has a very slow kinetics and its precipitation can take hundreds and sometimes thousands of hours. There are at least three reasons for the slow kinetics: (i) carbon and nitrogen are insoluble in sigma phase; as a consequence, sigma phase normally appears only after carbide and nitride precipitation has already taken place and the matrix is impoverished in carbon and nitrogen; (ii) its nucleation is difficult on account of its crystal structure being complex and very different from the austenitic matrix; and (iii) it is very rich in substitutional elements thus requiring long diffusion times. (PADILHA, 2002). Furthermore, the rate of sigma phase precipitation in the ferrite is 100 times faster than in the austenite (RAMIREZ-LONDOÑO, 1997). The presence of sigma phase increases toughness, but reduces the ductility and pitting corrosion resistance of stainless steel. Due to its low rate of formation, sigma phase is usually a problem when using stainless steels at high temperatures for extended periods of time (SEDRIKS, 1996). The sigma phase can be dissolved by heat treatment at 1050 ºC or above (SEDRIKS, 1996).

The time–temperature–transformation/precipitation (TTT/TTP) diagrams are mainly used to represent the sequence of precipitation and the competition among different phases. The available diagrams for these steels are normally isothermal TTT diagrams and

only show the curves corresponding to the start of the precipitation. Time–temperature–precipitation diagram for type 316 stainless steel is shown in Figure 4.

Figure 4 – Time-temperature-precipitation diagram for type 316 stainless steel containing 0.066% carbon.
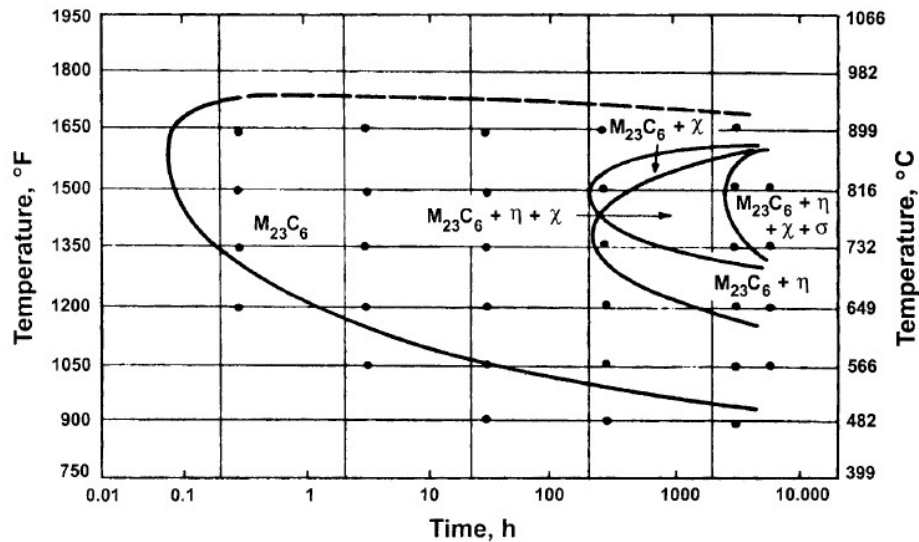
Source: B. Weiss, 1972.

Figure 5 shows a scanning electron microscopy (SEM) of a super austenitic steel AL-6XN®. The sigma phase precipitated at grain boundaries and inside the austenitic grain. Lewis defends that the sigma phase can form in the ferrite/austenite (δ/γ) interface (LEWIS *et al*, 2006).

Figure 5 – Sigma phase precipitation in an AL-6XN® super austenitic stainless steel.
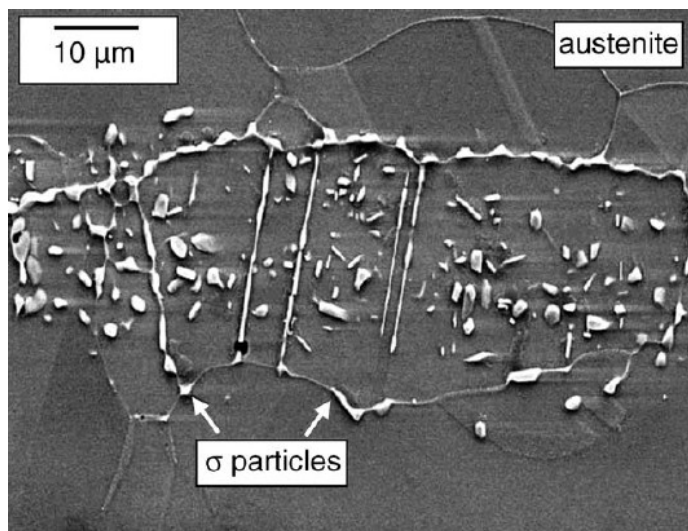
Source: Lewis *et al*, 2006

Figure 6 shows an Electron Backscatter diffraction (EBSD) on the surface of AL-6XN® steel showing sigma phase (indicated by dark regions) located on the grain boundary of austenite or in ferrite delta/austenite (δ/γ) interface as defends Lewis. The regions marked in 1 and 2 are grain 1 and grain 2, respectively.

Figure 6 – EBSD of AL-6XN® steel showing sigma phase in austenitic grain boundaries.

Source: Lewis *et al,* 2006.
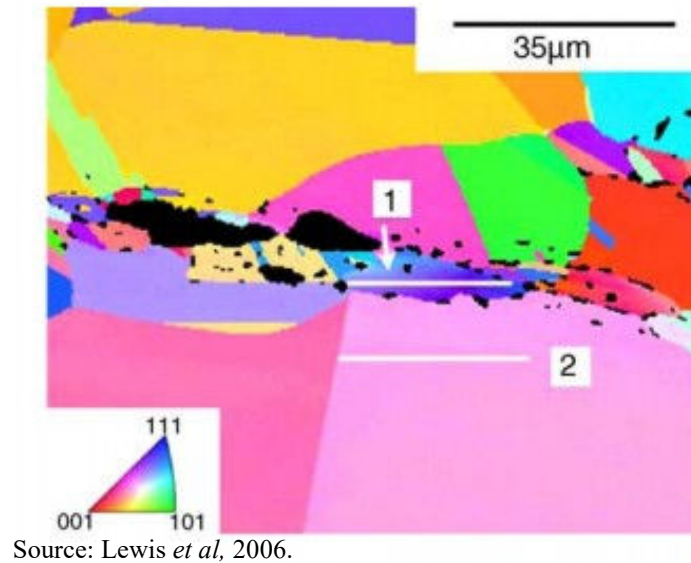
Phase equilibrium diagrams are important tools to predict the phases present in the austenitic stainless steels. Nevertheless they possess limitations due to the complexity of multicomponent thermodynamic calculations and also due to the transformation kinetics that may prevent the attainment of the equilibrium phases (PADILHA, 2002). Figure 7 shows a diagram for the binary Cr-Fe system. The diagram shows the temperature range depending on the Cr content for which the sigma phase will precipitate. In the diagram, it can be concluded that the sigma phase is formed from the ferrite in a temperature range of 500 °C - 800 °C.

Figure 8 shows a three-dimensional phase diagram for Fe-Ni-Cr system. These diagrams are complex and show a variety of phases in equilibrium as a function of composition and temperature. In all of the phase diagrams it can be seen sigma phase in equilibrium with other phases to a certain temperature range. Iron may be present in the form of ferrite (α), austenite (γ) or mixture of them.

In the diagram of Figure 8 it is observed the element chromium as a ferrite (α) stabilizer. Its presence tends to reduce the austenitic field. In the diagram of Figure 7 it is

observed the presence of three solid phases: austenite, ferrite and sigma phase. The sigma phase will be present to temperatures between 600 °C and 900 °C.

Figure 7 - Binary iron-chromium equilibrium diagram showing the sigma phase precipitation field
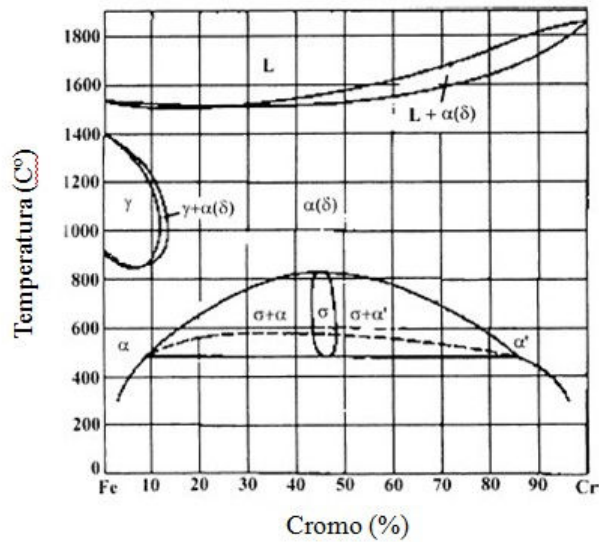
Source: ASM Handbook vol. 3 (1992).

Figure 8 - Three-dimensional view of the Fe–Cr–Ni equilibrium diagram
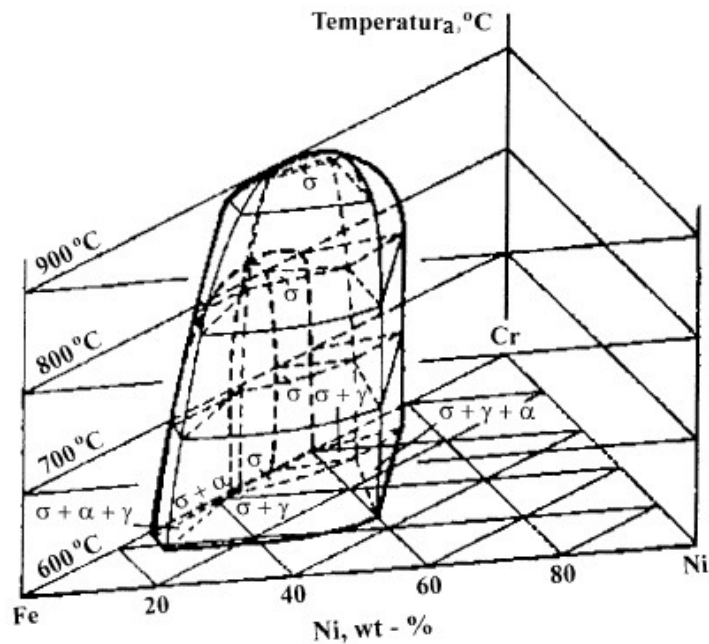
Source: ASM Handbook vol. 3, 1992.

Figure 9 shows the phase diagram for Fe-Cr-Mo system to a temperature of 650 °C. For this diagram, besides the sigma phase it is also observed the presence of chi-phase (χ).

This phase is not found in the binary diagrams and it is frequently found during the aging of austenitic stainless steels containing Mo (PADILHA, 2002).

Figure 9 - Phase equilibrium diagram for the Fe-Cr-Mo system in an isotherm of 650 °C
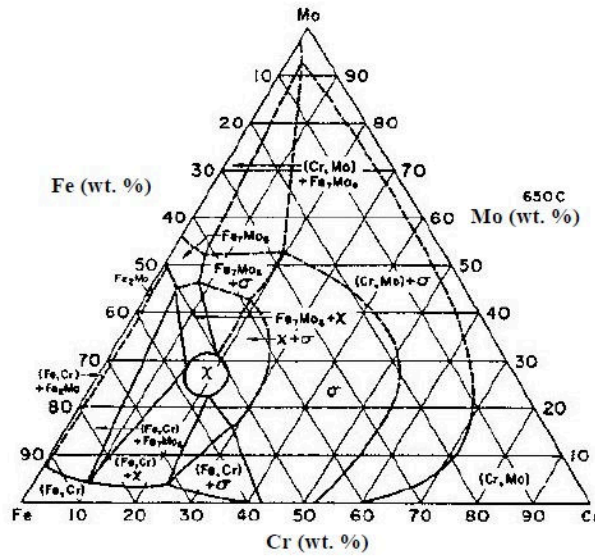
Source: ASM Handbook vol. 3, 1992.

4.3 Corrosion

Corrosion is a phenomenon in which there is the deterioration of materials by chemical or electrochemical action of the medium, and may or may not be associated with mechanical stress (GENTIL, 2011; NUNES, 2007). It can occur on various types of materials (metals, ceramics, polymers), but it is more commonly on metallic materials, such as metal alloys. In the case of metals, corrosion may also be defined as the loss of mass due to removal of electrons from the metal during corrosion. It can also be defined as a redox process, where the metal that loses electrons is the reducing agent.

On the corrosion process, the metals react with non-metallic elements present in the environment (oxygen, sulfur, etc) by forming compounds similar to those found in nature, from which they were extracted (NUNES, 2007). Hence, it is concluded that, corrosion is the opposite of the metallurgical process.

In nature, in form of compounds, the metals are more stable and have the lowest energy state. For a metal to be obtained from the nature, it is necessary to give energy to the compound (ore) through the metallurgical processes. In this case, the metal energy level is higher than the ore energy level found in nature. Thus, the metal is in a metastable equilibrium state. The corrosion reactions return the metal to its original form of ore found in nature by releasing energy (DUTRA & NUNES, 1999). This process is illustrated in Figure 10.

Figure 10 - Metallurgical cycle of the metals in nature.
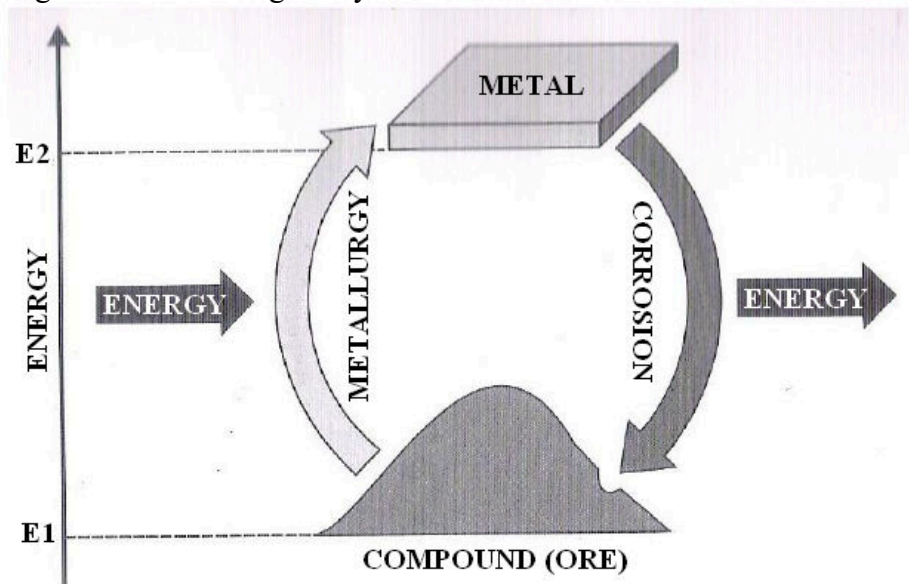
Source: adapted from Nunes, 2007.

The corrosion processes can be classified in two groups, depending on the type of the corrosive environment.

➢ Electrochemical corrosion
➢ Chemical corrosion

Table 3 shows the main features for the two types of corrosion process cited above.

Table 3 - Types of corrosion process found in nature.

Nature of the corrosion process	Characteristics
Electrochemical corrosion (aqueous corrosion)	Presence of liquid water
	Temperature below the dew point
	Formation of electrochemical cells
Chemical corrosion	Absence of liquid water
	Temperature above the dew point
	Direct interaction between the metal and the medium

Source: Nunes, 2007.

4.3.1 Forms of corrosion

To understand the corrosive processes and the application of appropriate security measures, it is necessary to know the fundamental characteristics of the different forms of corrosion.

The most common types of corrosion are listed below (GENTIL, 2011)

- ✓ General attack corrosion;
- ✓ Localized corrosion (pitting, crevice)
- ✓ Intergranular (intercrystalline);
- ✓ Intragranular;
- ✓ Filiform;
- ✓ Exfoliation;
- ✓ Graphitic;
- ✓ Dezincification;
- ✓ Hidrogen blistering;
- ✓ Corrosion fatigue;

4.3.2 CO_2 corrosion

The researches related to carbon dioxide corrosion (CO_2) began in the late 1960s. Since 1980, depth studies on CO_2 corrosion were done in order to understand its effects and

models of corrosion rate. In the same period, it was found out that the corrosion of steels in deaerated (oxygen free) CO_2 containing aqueous medium is of electrochemical nature. Moisseva e Kuksina analyzed the CO_2 corrosion products formed on the surfaces of metals and they concluded that the passive film was composed of iron carbonate (MOISSEVA & KUKSINA, 2003).

The first problems associated with CO_2 corrosion occurred in the North Sea in 1976 when there was a failure of various subsea systems in less than two years of operation. Since then, several studies on CO_2 corrosion mechanism were done to define forms of protection. The parameter used at that time to analyze the damage caused by CO_2 corrosion was the CO_2 partial pressure. Even for low pressure (0.76 bar), CO_2 corrosion can be harmful for the metals (FERREIRA, PEDRO A. E FERREIRA, CRISTINA V. M, 2003).

4.3.3   Carbon dioxide (CO_2)

Corrosion caused by CO_2 gas is called CO_2 corrosion or sweet corrosion. This form of corrosion is influenced by a complex interaction of parameters including the environment, pH, temperature, CO_2 partial pressure and the presence of organic acids (KERMANI & MORSHED, 2003).

The carbon dioxide itself does not interfere on corrosion of pipelines, but in contact with water, it forms carbonic acid (H_2CO_3). The carbonic acid reacts with the metal and it is very corrosive to the materials used in the oil and gas industry (ZHANG & CHENG, 2011).

CO_2 corrosion may present different morphologies: uniform corrosion, localized (pitting) corrosion, weld corrosion. Each type of corrosion depends on the operating conditions such as temperature and flow rate. Many of the problems involving CO_2 corrosion are localized corrosion where parts of the pipe walls suffer pitting corrosion. Depending on the fluid condition, the pit may develop at accelerated rates leading to premature failure of the pipe (GUILLÉN NÚÑES, 2006). The understanding of CO_2 corrosion of materials used in the oil and gas industry has increased in the last 20 years but the complete knowledge of its mechanism is not yet fully mastered (GUILLÉN NÚÑES, 2006, GUENTER SCHMITT; 2006).

In oil and gas production, the most prevalent form of corrosion is CO_2 corrosion. This gas is highly corrosive to carbon steel pipes as well as for the equipment used in the oil and gas production. The main concern is on corrosion control of costs relating to programs of material control and material substitution. It is estimated that 60% of corrosion failures are related to CO_2 corrosion (LOPEZ, D.A; PÉREZ, T; SIMISON, S. N, 2003). To minimize the problems caused by CO_2 corrosion, a new class of materials have been used. These materials are called Corrosion Resistant Alloys (CRA). Among these alloys one can cite the super duplex steels, superaustenitic stainless steels and nickel alloys which possess excellent resistance to corrosive environments (CUI *et al*, 2011).

CO_2 containing Systems are the most common in oil and gas extraction environments and one can recognize the occurrence of this type of corrosion by the presence of pits on the steel surface (CHOI *et al*, 2011; LING *et al*, 2011; SONG, 2010).

Song developed a carbon dioxide corrosion model to predict steel corrosion rate in oil and gas production and transportation systems (SONG, 2010). The model was based on the temperature of 25 °C, CO_2 partial pressure of 1 atm and a saturated boundary layer of 0.55 mm in thickness and validated with significant amount of published experimental data given elsewhere (SONG *et al*, 2004 and SONG *et al*, 2002). The developed model covered the following three scenarios: (1) deaerated CO_2 corrosion, (2) aerated CO_2 corrosion, and (3) CO_2 corrosion with cathodic protection. The model validation was performed for two systems: (1) a solution with dissolved CO_2 alone and (2) a solution with both dissolved CO_2 and O_2. The main conclusions of this model were: (1) CO_2 hydration has an important role in the corrosion process, (2) the dependence of H^+ diffusion on that of H_2CO_3 is included in the model to reflect the fact that H^+ results from H_2CO_3 dissociation, (3) the effects of O_2 and cathodic protection (CP) on CO_2 corrosion rate have been for the first time included in a mechanistic CO_2 corrosion model, (4) steel corrosion rate in H_2CO_3 is greater than in HCl at the same pH due to H_2CO_3 reduction, which, as an additional cathodic reaction, enhances iron oxidation. H^+ reduction rate in H_2CO_3 is less than in HCl because in H_2CO_3, reduction of H_2CO_3 competes with that of H^+ for electrons released from iron oxidation, (5) increasing temperature can increase CO_2 corrosion rate substantially, (6) for a given O_2 pressure, CO_2 can have a little effect on steel corrosion rate when CO_2 pressure is low, while this effect becomes progressively more significant as CO_2 pressure increases, (7) imposed CP decreases

steel corrosion rate most effectively near the free corrosion potential and this decrease becomes less effective as the steel potential shifts in the more negative direction.

4.3.4 CO₂ corrosion Mechanism

Several chemical reactions work together in the corrosion process, some may be homogeneous (occurring in the solution) and others can be heterogeneous (occurring on the metal surface). On CO_2 corrosion, hydration and dissolution processes are typically homogeneous chemical reactions while iron carbonate precipitation is considered heterogeneous (NORDSVEEN & NESIC, 2003)

The reaction (1) shows the hydration of CO_2 in water producing carbonic acid:

$$CO_2 + H_2O \rightarrow H_2CO_3 \qquad \text{(eq. 1)}$$

The carbonic acid is then dissociated in two types:

$$H_2CO_3 \rightarrow H^+ + HCO_3^- \qquad \text{(eq. 2)}$$

$$HCO_3^- \rightarrow H^+ + CO_3^{2-} \qquad \text{(eq. 3)}$$
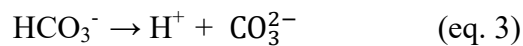
When the concentration of Fe^{2+} and CO_3^{2-} ions exceed the solubility limit, they can combine to form solid iron carbonate films according to equation 4:

$$Fe^{2+} + CO_3^{2-} \rightarrow FeCO_3(s) \qquad \text{(eq. 4)}$$

Other types of incrustations can precipitate on the metal surface, such as oxides, sulfides and other carbonates. In a practical situation, on CO_2 corrosion, many other species are present in the solution generating a larger number of additional chemical reactions (NORDSVEEN & NESIC, 2003).

Chemical reactions are often faster when compared with other processes that take place when the balance of the solution is maintained. When the reactions are slow, other fast processes such as electrochemical reactions or diffusion cannot unite with the balance of the solution altering the rate of electrochemical processes on the metal surface and the corrosion rate. When the solubility limit is reached as a result of high concentrations of species, it occurs the precipitation of a film on the metal surface. In a precipitation process, the heterogeneous nucleation occurs first on the metal surface or in pores of an existing film if the

homogeneous nucleation of the solution volume has a greater concentration of species. Nucleation is followed by the crystalline growth of the film. This film may act as a protective barrier against the diffusion of the species involved in corrosion reaction (GUILLÉN NÚÑES, 2006).

4.3.5 Factors that influence the CO_2 corrosion

As previously mentioned, the main factors that influence the CO_2 corrosion are: pH, temperature, steel microstructure, CO_2 partial pressure.

4.3.5.1 Influence of pH

The uniform corrosion rates of CO_2-saturated medium decreases with increasing pH. That is, the more basic the solution, the lower will be the corrosion rate. This decrease can be attributed to the formation of carbonate salts such as $FeCO_3$ and bicarbonates as well as the reduction of the solubility of the $FeCO_3$ (NESIC & LUNDE, 1994). For the same pH value, carbonic acid has more aggressive effect than the strong acids as hydrochloric acid (HCl) as shown in Figure 11. This is due to the ability of H_2CO_3 in dissociating rapidly on the metal surface promoting the necessary generation of hydrogen ions at the cathode allowing the occurrence of anodic reaction at the anode (NESIC, 1996)

Figure 11 - Corrosion rate versus pH at the steel surface for different acids.
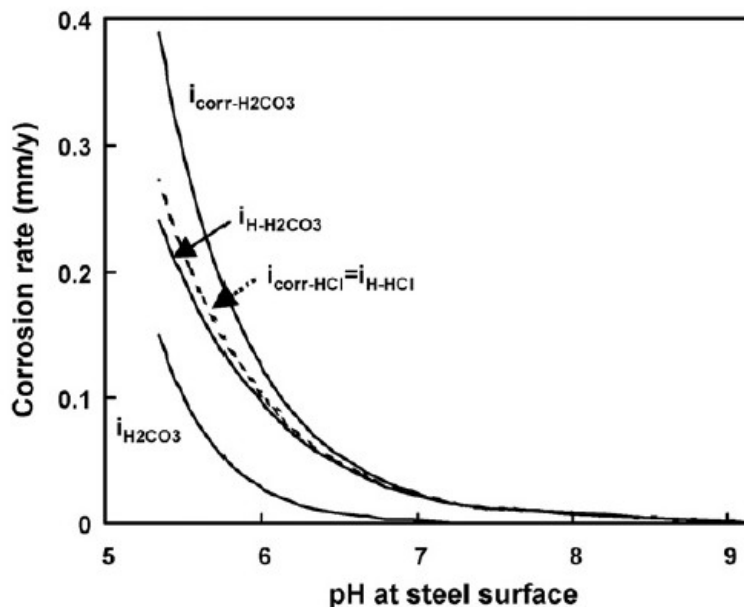
Source: Nesic, 1996.

4.3.5.2   Influence of temperature

The temperature is another important parameter to evaluate the formation and stability of passive films of CO_2-saturated media.

Some authors have studied the passive film formed from $FeCO_3$. Das e Khama studied the influence of temperature in a range of 30 °C to 120 °C for the formation of $FeCO_3$ in low-carbon steels. They observed that, at low temperatures, corrosion rates were increased by the dissolution of Fe^{2+} ions in the solution as a result of the formation of a porous and not protective film of FeCO3. They observed that the corrosion rate increased significantly to the temperature of 90 °C by increasing of the porosity of the film. They also observed that above 90 °C, a more dense film was formed and at 120 °C the corrosion rates decreased significantly (DAS e KHANNA, 2004).

Song *et al*, as previously mentioned, built a model to determine the CO_2 corrosion mechanisms and concluded that the corrosion rate increases with increasing temperature. The model is consistent with experimental data of De Waard *et al* (DE WAARD, 1993). The results are depicted in Figure 12. At each CO_2 pressure, the corrosion rate increases progressively with increasing temperature up to 90 °C. Since the corrosion rate increases with increasing temperature more strongly at higher temperatures, it suggests that for a buried pipeline corrosion would be more severe near a gas compressor station where the temperature is higher (could reach as high as 75 °C) (SONG, 2004).

Figure 12 - Effect of temperature on corrosion rates at five different CO_2 pressures.
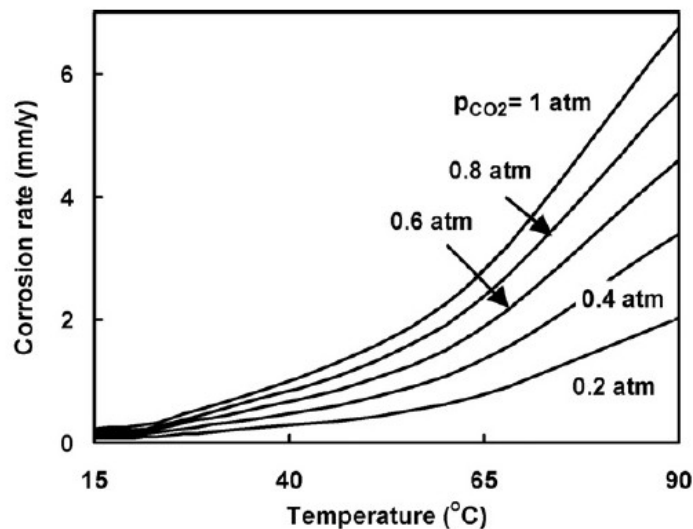
Source: De Waard, 1993.

Dunstad studied the protective mechanism of the passive film on carbon steel for a temperature range of 40 °C to 120 °C. The author observed that for temperatures higher than 60 °C, the precipitation rate for the formation of the passive film is fast. The film is not easily formed to temperatures below 40 °C because the precipitation rate is very slow. The author also observed that a passive film formed at 120 °C was less resistant than for a film formed at 80 °C (DUGSTAD, 1998).

4.3.5.3 *Influence of alloy composition*

In recent years, the influence of alloy composition has been investigated intensively. The highest effect against corrosion is encountered with additions of chromium. The corrosion rate is significantly decreased with increasing Cr content (BURKE; 1984; SCHMITT; 19849). The interest in low alloy steels with increased Cr content in the order of 3 to 5% Cr has increased in recent years mainly because of the applications in oil and gas industry. A number of investigations were devoted not only to the chromium content but also to the influence of microalloying elements such as V, Ti, Nb, Mo, Cu and Si (DUGSTAD *et al*, 2001; NOSE *et al*, 2001). Some works were carried out in order to study the effect of reducing carbon aiming to avoid the formation of carbides like chromium carbide. This can be achieved by reducing the carbon content and by adding elements that form more stable carbides such as V, Ti, Nb and Mo.(BOSCH, 2003; AL-HASSAN, 1998).

A study was carried out with 3% Cr steels to see the effect of Cr when compared with another steel, L80, that has no Cr in its composition (SCHMITT *et al*, 2006; KERMAN *et al*, 2003). With this study it was observed that microalloying influences the corrosion performance of 3% Cr steels significantly. Specifically alloys with vanadium yielded excellent results. For the 3% Cr, the corrosion resistance increases with increasing temperature while for the L80 it was observed the opposite as shown in Figure 13. Compared with the L80 steel, the corrosion rate of 3% Cr is decreased by factors of 3 to 40 depending on the temperature and alloying elements.

Figure 13 - Influence of temperature on the corrosion rate of different steels in buffered CO_2 containing 10% NaCl solution.
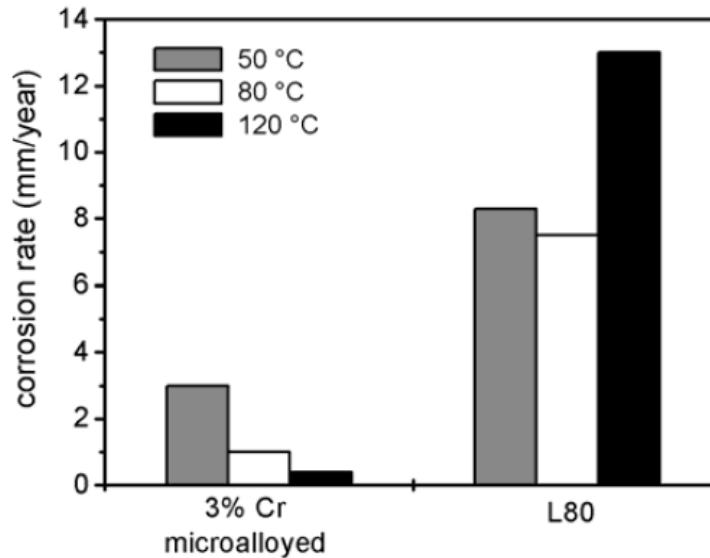
Source: Kermani, 2003.

Kermani *et al* studied the effect of microalloying on the CO_2 corrosion rate for some steels. The result is summarized in Figure 14 (KERMANI *et al*, 2003; KERMANI *et al*, 2004). However, for the effect of Cu in carbon steels, controversial results were obtained which indicated that increased Cu and Ni contents may accelerate mesa attack and additionally increase the general corrosion rate (KIMURA *et al*, 1994). In earlier investigation, Dugstad *et al* reported similar results (DUGSTAD, 1991).

Stainless steels are more resistant in severe sweet and mildly sour production conditions and have been used for effective corrosion control (KERMANI, 2005; KIMURA, 2007). Some authors observed that stainless steels exhibited less resistance to localized corrosion at elevated temperature and may be susceptible to stress corrosion cracking (AMAYA, 1998; KERMANI, 2005; KIMURA, 2004).

Figure 14 - Schematic presentation of relative effects of additional microalloying elements on corrosion rate of 3% Cr steels.
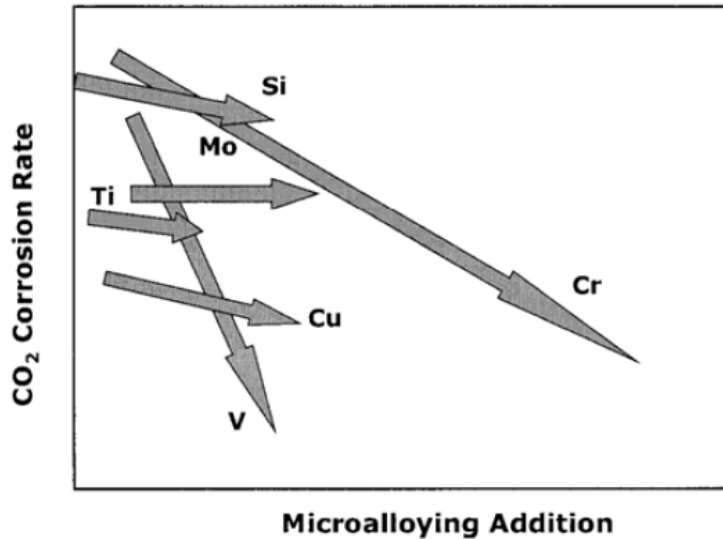
Source: Kermani, 2001.

4.3.5.4 *influence of steel microstructure*

The microstructure of the steels also influences the corrosion resistance. Several authors have studied the influence of steel microstructure on the corrosion process in CO_2 containing aqueous solutions, although there is no general agreement on this issue (UEDA, 1999; PALACIOS, 1991; UEDA, 1996; NICE, 1998; DUGSTAD, 2000; NESIC, 1994). According to Lopes *et al*, the final microstructure of the steels is determined by the chemical composition, mechanical and heat treatments during the manufacturing process (LOPEZ *et al*, 2003). The author studied the characteristics of the corrosive layer formed on carbon steel focusing its morphology, thickness and composition. The film characteristics were evaluated by SEM and X-ray diffraction (XRD). The electrolyte used was a CO_2-saturated aqueous solution of 5% NaCl. The pH and temperature of the solution were 6 and 40 ºC, respectively. The author concluded that the microstructure of the steel influence the properties of corrosive layer, as well as morphology and proportion of various chemical components (LOPEZ *et al*, 2003).

Some phases present in the metal during the corrosion process become sites for cathodic and anodic reactions. The study of the shape, size and distribution of these phases on

the corrosion rate is very important. The literature reports that the presence of carbides such as cementite (Fe_3C) assist in formation of non-protective films. The literature also reports that cementite is more cathodic than the ferrite leading to formation of a galvanic microcell between cementite and ferrite. In a corrosive process, this results in severe attacks in the bands of pearlite (DUGSTAND *et al*, 2001).

5   MATERIALS AND METHODS

5.1   Material

The materials used in this research were the AL-6XN PLUS™ super austenitic stainless steel provided by the American company Allegheny Ludlum Corporation, the 904L superaustenitic stainless steel provided by the Fluminense Federal University and the 300 series austenitic stainless steels AISI 316L and 317L provided by the Federal University of Ceará (UFC). Table 4 presents the chemical composition of the studied steels measured in an Optical Emission Spectrometer (PDA-7000 SHIMADZU).

Table 4 - Composition (in wt%) and PRE_N of the studied alloys.

Alloys	C	N	Mn	Si	Cr	Ni	Mo	PRE_N
316L	0.030	0.05	1.65	0.41	17.2	10.7	2.2	26
317L	0.024	0.06	1.49	0.40	17.8	12.3	3.5	31
904L	0.027	0.10	0.74	0.66	19.5	24.3	4.5	37
AL-6XN PLUS^{TM}	0.021	0.24	0.35	0.32	21.8	25.8	7.6	54

Source: the author.

The index that measures the pitting corrosion resistance for the studied alloys are also shown in Table 4. The Pitting Corrosion Resistance can be expressed in terms of some alloying elements such as Cr, Mo and N. This expression is known as PRE_N (Pitting Resistance Equivalent Number) and expresses the ability of the alloy to resist pitting corrosion. In chloride-containing media, the PRE_N of austenitic stainless steels can be expressed by the equation 5 (Allegheny-Lundlum, 2002).

$$PRE_N = \%Cr + 3.3\%Mo + 30\%N \qquad (eq.\ 5)$$

5.2   Methodology

The methodology used in this research was divided in the following steps:

- ✓ 1st Step: Thermodynamic study of the alloys;
- ✓ 2nd Step: Heat treatments based on the thermodynamic simulations;
- ✓ 3rd Step: Metallographic preparation of the samples;
- ✓ 4th Step: Microstructural characterization of the samples;
- ✓ 5th Step: Analysis of the samples using XRD by Synchrotron Light to detect sigma phase;
- ✓ 6th Step: CO_2 corrosion tests using the electrochemical techniques (cyclic polarization and potential step);
- ✓ 7th Step: Pressurized corrosion tests using CO_2 gas, synthetic air and a mixture of them,
- ✓ 8th Step: Characterization after corrosion tests using optical microscopy and SEM.

1st Step: Thermodynamic study of the alloys

A thermodynamic study was performed using the software Thermocalc® to predict the possible phases that could form during heat treatments. As input it was used the chemical composition of each alloy and the temperature range was set to between 500 °C and 1200 °C. This temperature range is considered as being of high temperatures for austenitic stainless steels (ANBURAJ *et al,* 2012). The software predicts the phases present at each studied temperature as well as their percentages. The database used for calculating the percentages of each phase was the TCFE6 database. Based on these simulations, the first chosen temperature was 760 °C.

2nd Step: Heat treatments based on the thermodynamic simulations

Based on the thermodynamic simulation, the samples were solution annealed at 1150 °C. The time used for the solution annealing was 30 min followed by water quenching. This first heat treatment had the goal to obtain only the matrix phase (austenite). After solution annealing, samples underwent heat treatments at 760 °C for a period of 72 h followed by water quenching. Another temperatures (600 °C and 700 °C) and time (120 h and 960 h) were also used.

3rd Step: Metallographic preparation of the samples

After heat treatments, the samples were mounted in bakelite and ground with silicon carbide paper up to grade 1200. Furthermore, the samples were polished with diamond paste down to 1 μm for the acquisition of their surface micrographs. Sample dimensions were on average of 5.8 mm x 5.5 mm x 3.3 mm.

4th Step: Microstructural characterization of the samples

After the heat treatment, the samples of the steels were etched with potassium hydroxide reagent K(OH) 20% (3 V for 50 s) in an attempt to reveal sigma phase. The samples were also etched with oxalic acid 10% (3 V for 50 s) to reveal the microstructure. Generally, the precipitation of deleterious phases such as sigma phase occurs at grain boundaries in small amounts. Phases such as sigma phase, laves, chi, carbides, nitrides exhibit similar morphologies making it very difficult to distinguish from one another. EBSD technique to identify the presence or not of sigma phase was used as an auxiliary measurement.

5th Step: Analysis of the samples using XRD by Synchrotron Light to detect sigma phase

Some of the heat treated samples were analyzed by Synchrotron Light to detect the presence of deleterious phases from heat treatments. The samples in the as-received condition were also analyzed to be compared with the heat treated samples. The selected samples of the alloys heat treated at 600 °C for 120 h were examined at Brazilian Synchrotron Light Laboratory shown in Figure 15.

Figure 15 - LNLS - Brazilian Synchrotron Light Laboratory in Campinas-SP.

Source: the author.

Samples of the 316L and AL-6XN PLUS™ were analyzed by XRD using Synchrotron Light (energy 12 keV). These two alloys were selected because they represent the less and the most corrosion resistant materials of this research. The samples were named according to Table 5. The 316L alloy was named of J and the AL-6XN PLUS™ alloy was named of C.

Table 5 - Samples name and conditions used in the tests.

sample name	alloy	condition
J3	316L	heat treated at 600 °C for 120 h
C1	AL-6XN PLUS™	as-received
C3	AL-6XN PLUS™	heat treated at 600 °C for 120 h
C4	AL-6XN PLUS™	C3 *in situ* at 700 °C for 8 h

Source: the author.

Prior to testing, a simulation of the sigma peaks for austenitic stainless steels using the PowderCell software was done. The result is shown in Figure 16. From the simulation, the sigma phase peaks appeared between 25° and 35° (2 theta). Despite of the

specimens shape, the tests did not involve tensions on the specimens. The XRD simulation was carried out for a wavelength of 0.10332 nm.

Figure 16 - Sigma peaks simulation using synchrotron light for austenitic stainless steels.
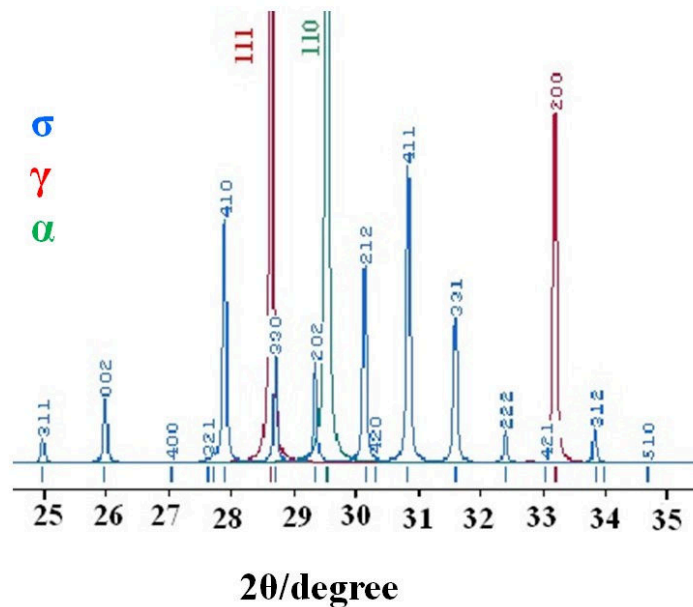
Source: the author.

An *in situ* experiment was also carried out on the AL-6XN PLUS™ sample. The sample was renamed of C4 and the goal of this test was to complement the attempts to precipitate sigma phase. The sample was welded on the center with a thermocouple of Cromel (Ni90%Cr10%)/ Alumel (Ni95%Al5%) (Figure 17) in order to measure the temperature during the experiment. The sample was fixed inside a device called gleeble as shown in Figure 18. No stress was applied on the sample. The sample was heat treated at 700 °C for 8 h by joule effect with a heating rate of 100 °C/min. Two detectors acquired images of the sample. The total of 10 images were acquired during the experiment. The experiment was also monitored by a camera positioned inside the gleeble (Figure 19).

Figure 17 - Photograph of the sample of the *in situ* experiment showing the thermocouple chromel/alumel.
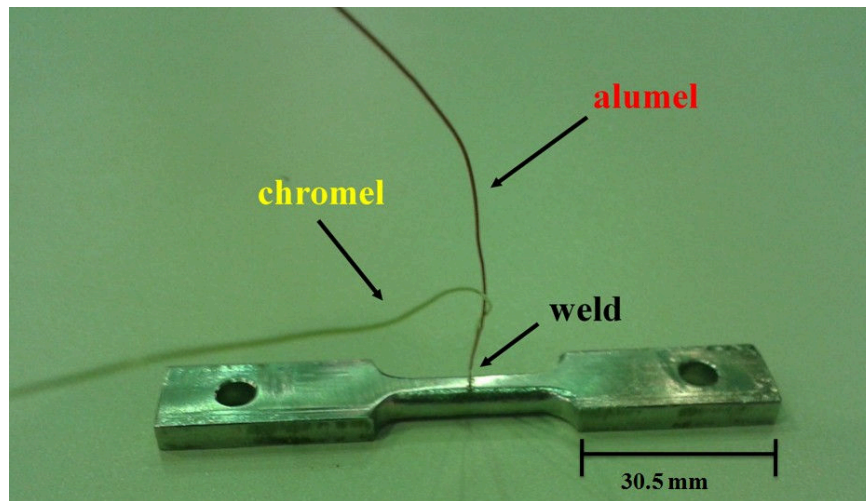
Source: the author.

Figure 18 - Photograph of the sample fixed inside the gleeble for the XRD measurements.
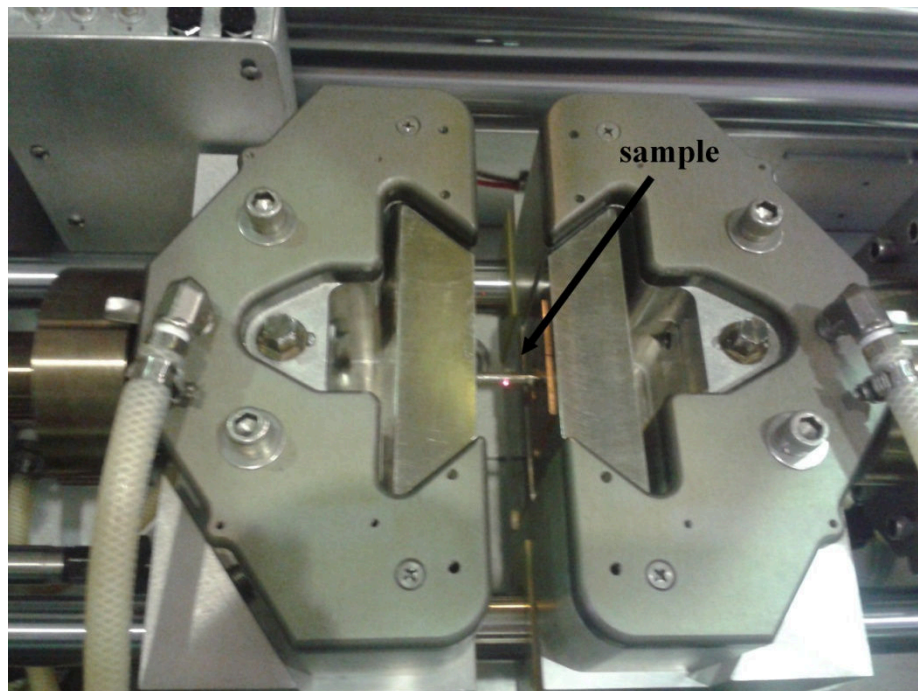
Source: the author.

Figure 19 - Live view configuration of the sample in the *in situ* experiment.
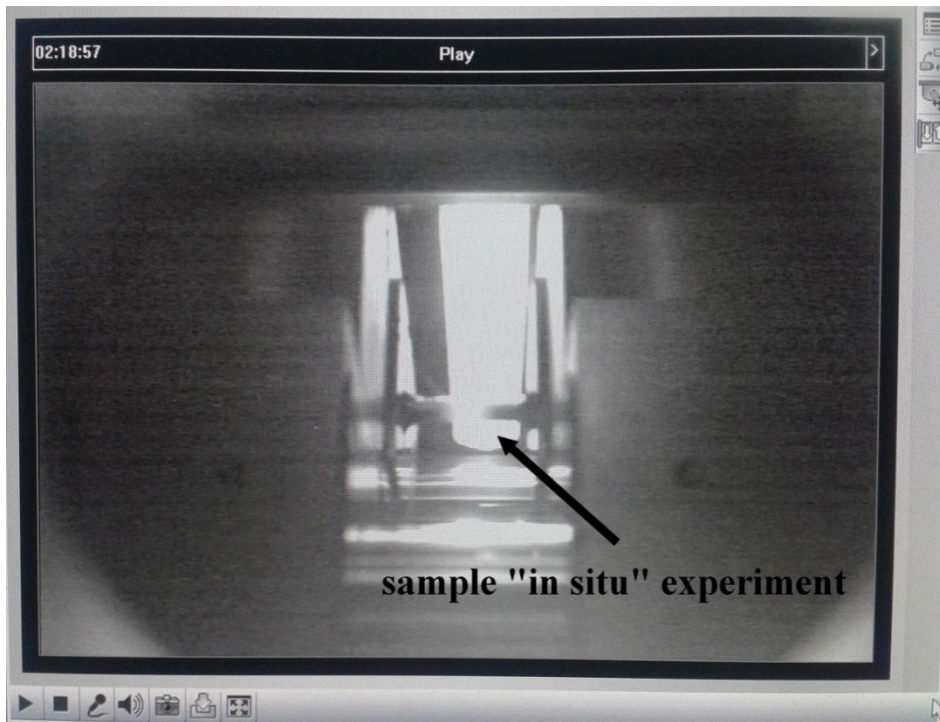
Source: the author.

6th Step: CO_2 corrosion tests using electrochemical techniques

The electrochemical measurements were carried out at room temperature using the cyclic polarization technique. In the preparation for the electrochemical tests, the samples were mounted in cold curing epoxy resin, ground with 600 grade sandpaper, rinsed with ethanol and blow-dried before each measurement. The dimensions of the samples were on average 8.0 mm x 8.0 mm x 3.5 mm. The samples were coated with a lacquer to reduce crevice corrosion on the epoxy/steel edges leaving an average exposed area of 39 mm². All the samples were investigated in the as-received condition and heat treated. For the electrochemical polarization tests, a three adapted electrode cell configuration was used as shown in Figure 20.

Figure 20- Schematic illustration of the cell for the CO_2 corrosion tests showing all the electrodes used.
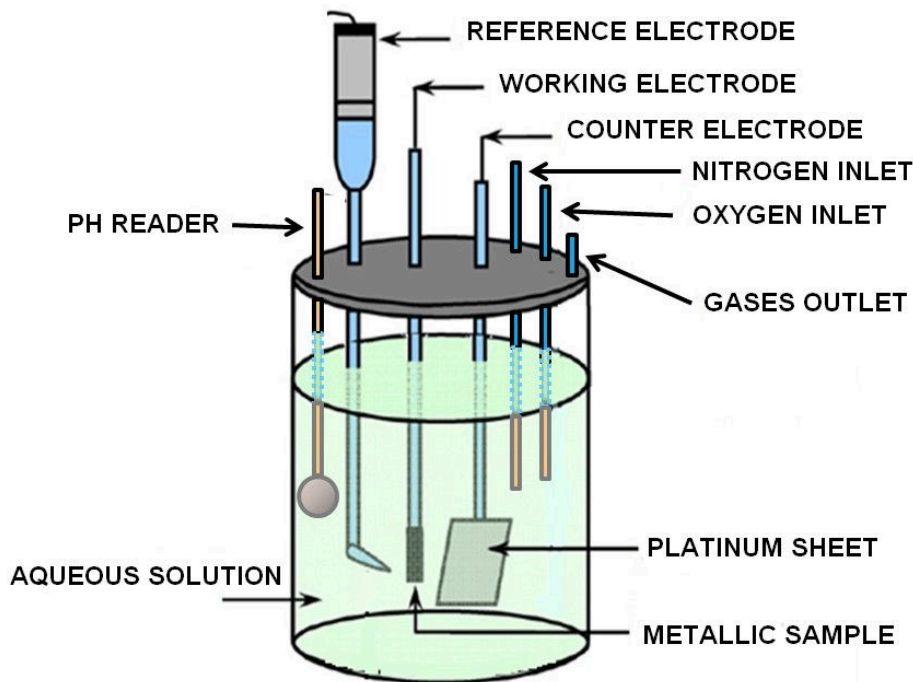
Source: adapted from Ferreira Italiano, 2012.

A saturated silver/silver-chloride (Ag/AgCl) as reference electrode was used while a platinum electrode as counter electrode was used. A pH reader was also used. The electrolyte used was CO_2-saturated synthetic oil field formation water named TQ 3219 which composition is shown in Table 6.

Table 6 - Chemical composition of the electrolyte used calculated for 1 L of water.

Reagent	$CaSO_4$	$MgCl_2$	$NaHCO_3$	NaCl
Content (g/L)	0.516	4.566	0.425	29

Source: PETROBRAS/CENPES, 2007

A potentiostat (AUTOLAB PGSTAT302N) connected to a microcomputer was used. The software NOVA 1.9 was used to obtain data from the cyclic polarization curves. Before the electrochemical tests, the electrolyte was deaerated with nitrogen to simulate pure oxygen-free environment below the pre-salt layer. Upon reaching a pH of approximately 8.2 ± 0.1, the solution is deaerated. Soon after, the nitrogen flow is decreased and the solution is

bubbled with carbon dioxide until the pH is stabilized indicating the moment at which the solution is saturated with carbon dioxide (pH of approximately 5.1 ± 0.1). The final pH of the solution is acid as shown in Figure 21.

Figure 21 - pH of the TQ 3219 solution as a function of the bubbling time with N_2 and CO_2.
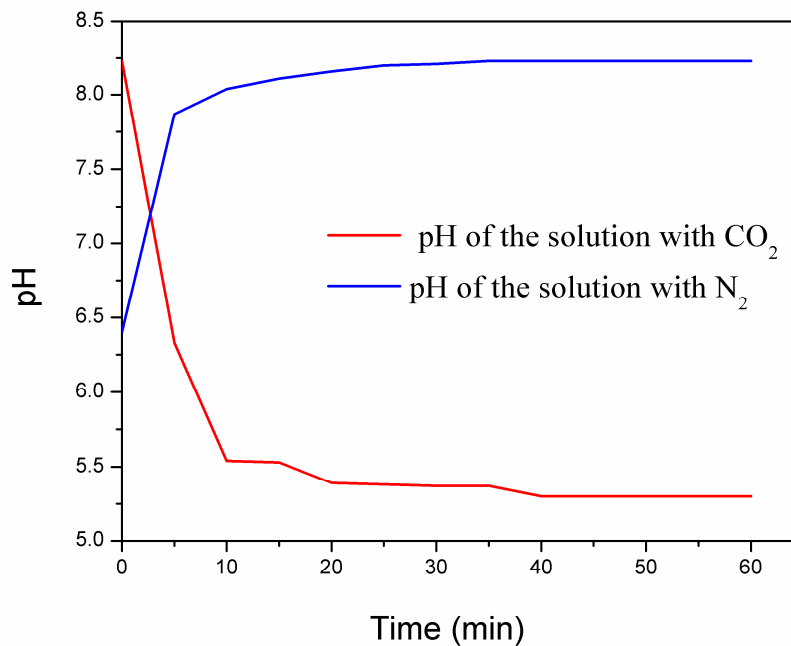
Source: the author.

After the saturation of the solution with carbon dioxide, the samples were immersed for 30 min in the solution to determine the open circuit potential (OCP). After the immersion tests, it starts the cyclic polarization tests. The samples were investigated in a potential range of -0.5 V/Ag/AgCl to 1.2 V/Ag/AgCl versus OCP with a scan rate of 0.33 mV/s. After the cyclic polarization tests, the samples were cleaned once again with water, rinsed with ethanol and dried. Micrographs of the samples surfaces after electrochemical test were obtained by scanning electron microscope (SEM) for comparison. The electrochemical tests were reproduced in triplicate.

For the Potential Step tests, the samples were tested in the as-received condition. They were mounted in cold curing epoxy resin, grinded with P600 grit paper, rinsed with

ethanol and dried before each measurement. The exposure area of the samples was 1 cm². The solution used for the tests was the same solution used for the cyclic polarization tests (TQ3219). This time, the solution was aerated and not saturated with CO_2. The solution was basic (pH = 8.1). The aim of this test was to evaluate only the effect of the solution without the effect of CO_2 gas. A potentiostatic pitting corrosion test called Potential Step was used. A saturated Ag/AgCl reference electrode and Pt counter electrode were also used. The OCP was monitored until the stable condition. Subsequently the potential was increased in steps of 50 mV every 1 h until a breakthrough current density was attained. The pitting corrosion initiation potential was defined when the current density reached values above 0.1 mA/cm² (EIDHAGEN & KIVISÄKK, 2011). After the tests, the samples were examined by SEM to confirm the presence of pits on the alloys surfaces. The tests were carried out at room temperature (25°C).

7th Step: Corrosion testing pressurized with CO_2 gas, synthetic air and the mixture of them.

For pressurized testing, a high pressure system was used and it comprises of the following components: gas supply system, a thermostat (BTC-3000) and a high-pressure laboratory reactor (BR-300, 1.4571). Two gases, synthetic air (80% N_2 and 20% O_2) and carbon dioxide gas (99.995% of purity) were used. In the first tests, the effect of the gases pressure on the samples were investigated separately. In the last test, the gases were mixed. The samples were cut in sheets with the following dimensions: 3.2 cm x 6.6 cm x 0.19 cm (316L), 3.0 cm x 8.2 cm x 0.30 cm (317L) and 3.2 cm x 8.2 cm x 0.59 cm (AL-6XN PLUS™) as shown in Figure 22. The 904L steel was not investigated in the pressured experiments due to the limitation of the material in manufacturing the samples. The samples were investigated in the as-received condition. The experiments were carried out in duplicate.

Figure 22 - Sample sizes (cm) of the 316L, 317L and AL-6XN PLUS^{TM} steels, respectively.
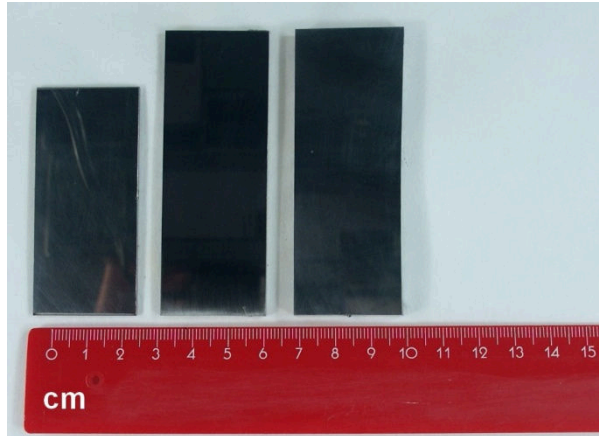
Source: the author.

Before the test, the samples were cleaned with distilled water, rinsed with ethanol and dried. Afterwards the samples were fixed on a support (Figure 23a) and sprayed with the TQ3219 solution as shown in Figure 23b. The support with the samples fixed on the base was placed in an autoclave (Figure 23c). In Figure 24, a schematic drawing depicts the positions of the samples within the autoclave. The pressures and temperature used in this study were 5 MPa, 8 MPa and 80 °C, respectively. The tests were performed during one week (10080 min). The pressure and the temperature were monitored daily. After the exposure tests, the samples were analyzed by optical microscopy, cleaned with HCl 20% to remove the corrosion products and analyzed with a SEM (TESCAN, MIRA3 XMU9). The corrosion products were analyzed by XRD and the peaks were identified by the FIZ/NIST Inorganic Crystal Database software. The surface topography was investigated by an Optical White Light Interferometric Surface Measuring System (SMS Oberflächen-Messsystem, Breitmeier Messtechnick).

Figure 23 - Samples a) fixed on the specimen holder, b) sprayed with the TQ3219 solution and c) inside the autoclave.
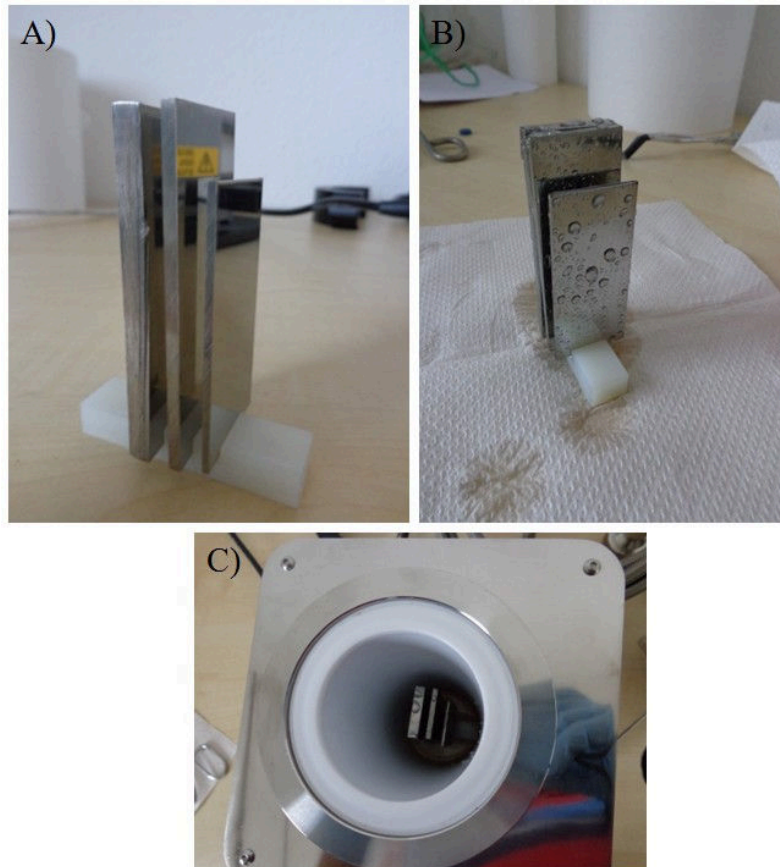
Source: the author.

Figure 24 - Scheme of the samples inside the autoclave for the pressurized experiments..
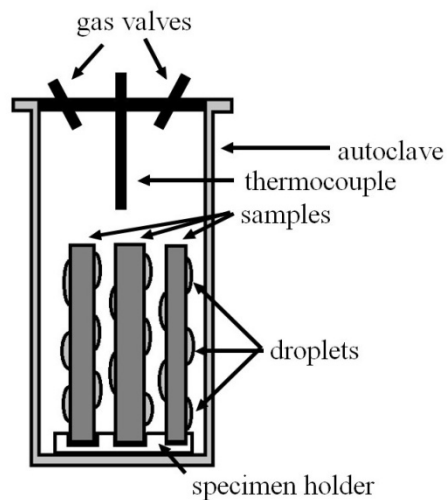
Source: the author.

All the pressurized tests using CO_2 and synthetic air were done at Freiberg University of Mining and Technology in Germany. Figure 25 depicts the flowchart of the experiments.

Figure 25 - Flowchart of the experiments and measurements used in this research.
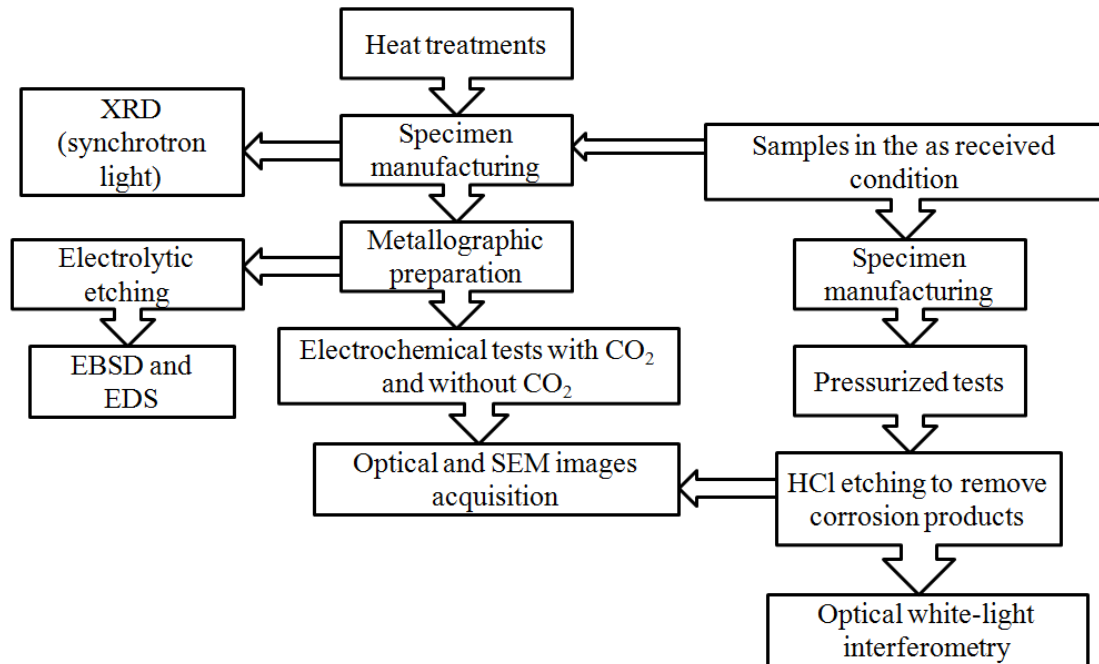
6   RESULTS AND DISCUSSION

6.1   Thermodynamic Study and heat treatments

The percentage of the predicted phases for each alloy are shown from Figure 26 to Figure 29. The graphics represent the content (wt%) of the main phases that can precipitate in austenitic stainless steels. The phases provided by the Thermo Calc® software for the temperature range used in this work are mainly austenite, ferrite, sigma, laves and $M_{23}C_6$ carbide. Figure 26 shows the content of sigma phase for the studied alloys and Figure 27 shows the content of carbide ($M_{23}C_6$) for the studied alloys. It is observed that the sigma phase and the $M_{23}C_6$ carbide are present in these simulations for the temperature range of 500 °C to 900 °C and their content decrease with the increase of temperature with time. Figure 28 shows the content of laves phase for the 317L, 904L and AL-6XN PLUS™. It was not predicted laves phase for the 316L for this rage of temperature. Figure 29 shows the content of ferrite phase for the conventional austenitic steels (316L and 317L). It was also predicted the precipitation of chi phase for the super austenitic alloys . The calculated percentages of the predicted phases are listed in Table 7. The fraction of $M_{23}C_6$ carbide is predicted to be low for all the studied alloys. The percentage of sigma phase is higher for the super austenitic stainless steel. This phase is a deleterious Mo and Cr-rich phase and increases with the Mo and Cr content of the alloys. For the same heat treatment at the same temperature range, it is more likely that the sigma phase precipitates in super austenitic stainless steels than in the conventional austenitic ones. The precipitation of this phase may deplete the matrix of these important alloying elements and lead to a degradation of the desired properties, such as corrosion resistance and mechanical strength. It is well known that the formation of sigma phase is more favorable in alloys with higher Mo content (MITCHELL, 2001, DA SILVA *et al*, 2015). The most probable phase that can precipitate in all studied alloys at 600 °C is sigma phase. As the temperature increases, this phase tends to dissolve as seen in Figure 26. Between 700 °C and 800 °C the sigma phase content is also considerable mainly for super austenitic stainless steels. As all the studied alloys of this work are low carbon alloys, so the carbide formation is more difficult but not impossible.

Thermodynamic simulations are a powerful tools to predict the phase formation for a specific alloy at a specific temperature or temperature range but no information is given

about the time that certain phases may precipitate. During the heat treatments, the samples were heat treated in different temperatures and ranges of time. The temperatures of each heat treatments are shown in Table 7. According to Barbosa *et al*, the 904L super austenitic stainless steel could precipitate sigma phase at 760 °C (BARBOSA, 2012). So, the first heat treatment was done at 760 °C for 72 h. This was the 1st attempt to precipitate sigma phase in all alloys mainly in AL-6XN PLUS™.

Figure 26 – Sigma content (wt%) versus temperature for the studied alloys.
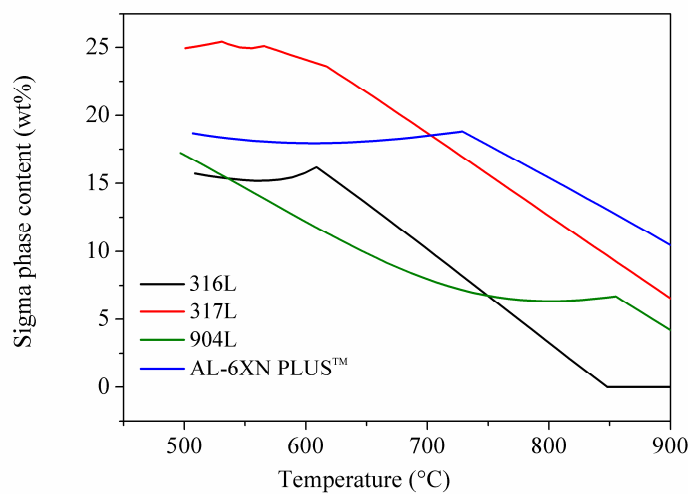
Source: the author.

Figure 27 - Carbide $M_{23}C_6$ content (wt%) versus temperature for the studied alloys.
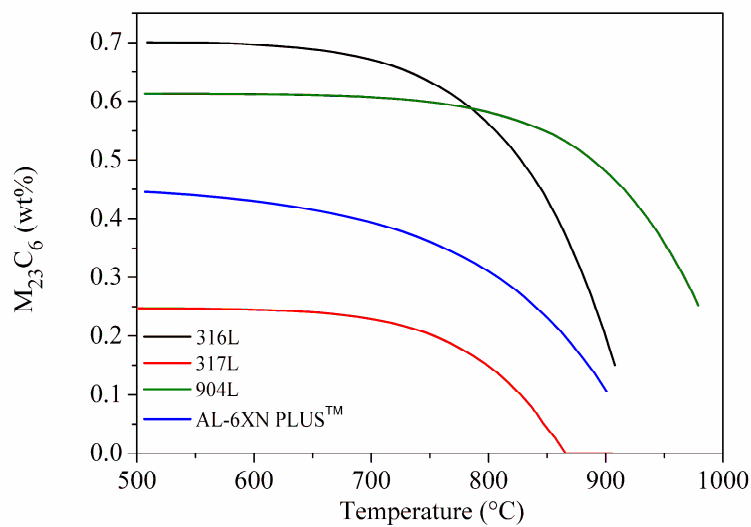
Source: the author

Figure 28 - Laves content (wt%) versus temperature for the studied alloys.
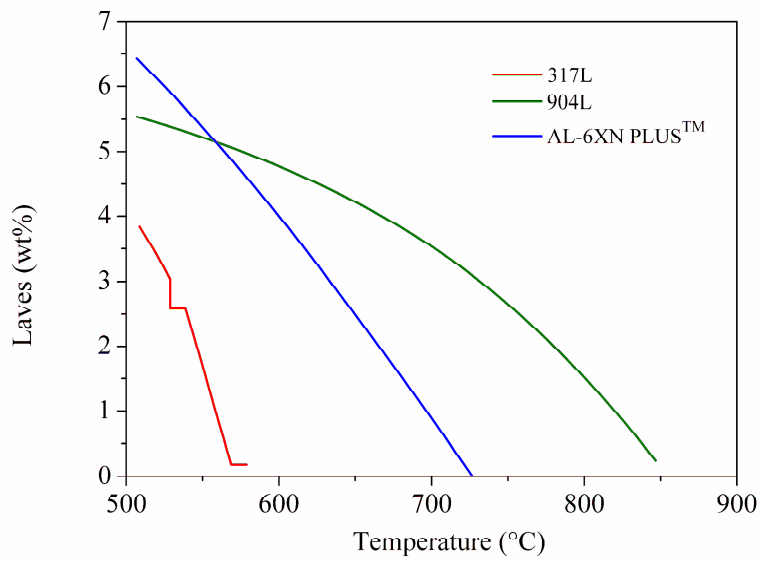
Source: the author.

Figure 29 - Ferrite content (wt%) versus temperature for the 316L and 317L alloys.
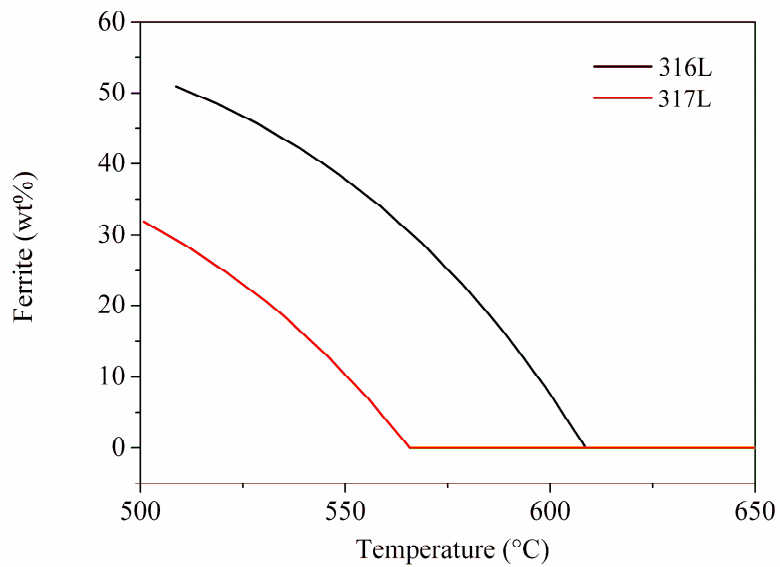
Source: the author.

Table 7 - Thermocalc® calculated phases present in the 316L, 317L, 904L, and AL-6XN PLUS™ alloys and their corresponding calculated percentages (wt%) at each studied temperature.

Temperature (°C)	Alloy	$M_{23}C_6$	sigma	Fe α	Fe ϒ	Chi	Laves
600	316L	0.70	15.7	8.7	74.9	0	0
	317L	0.24	23.9	0	75.5	0.34	0
	904L	0.61	11.8	0	82.8	0	4.7
	AL-6XN PLUSTM	0.43	18	0	75.2	0	3.8
700	316L	0.67	10.4	0	89	0	0
	317L	0.23	18.9	0	80.9	0	0
	904L	0.61	8.1	0	87.7	0	3.6
	AL-6XN PLUSTM	0.40	18.5	0	77.2	0	0,7
760	316L	0.63	6.2	0	93.1	0	0
	317L	0.20	15.2	0	84.6	0	0
	904L	0.60	6.6	0	90.2	0	2.5
	AL-6XN PLUSTM	0.35	17.4	0	79.3	0	0
1150	316L	0	0	0	100	0	0
	317L	0	0	0	100	0	0
	904L	0	0	0	100	0	0
	AL-6XN PLUSTM	0	6.1	0	93.8	0	0

Source: the author.

EBSD measurements were carried out on the AL-6XN PLUS™ and 904L alloys. The EBSD measurement region are shown in Figure 30. Figure 31 shows the EBSD image of the map of the phases for the AL-6XN PLUS™ alloy treated at 760 °C for 72 h. As observed in Figure 31, no sigma phase was detected for the heat treatment at 760 °C for 72 h. Only the austenite matrix (in red) was detected. The sample of 904L exhibited a similar result. The possible phases that can occur in a material can be predicted from calculated phase diagrams as discussed before, but some limitations apply and the results must be interpreted with care. Under some conditions, equilibrium is not reached on a timescale compatible with the heat treatment applied to the material.

Figure 30 - EBSD region on the alloys a) AL-6XN PLUS™ and b) 904L both treated at 760 °C for 72h.
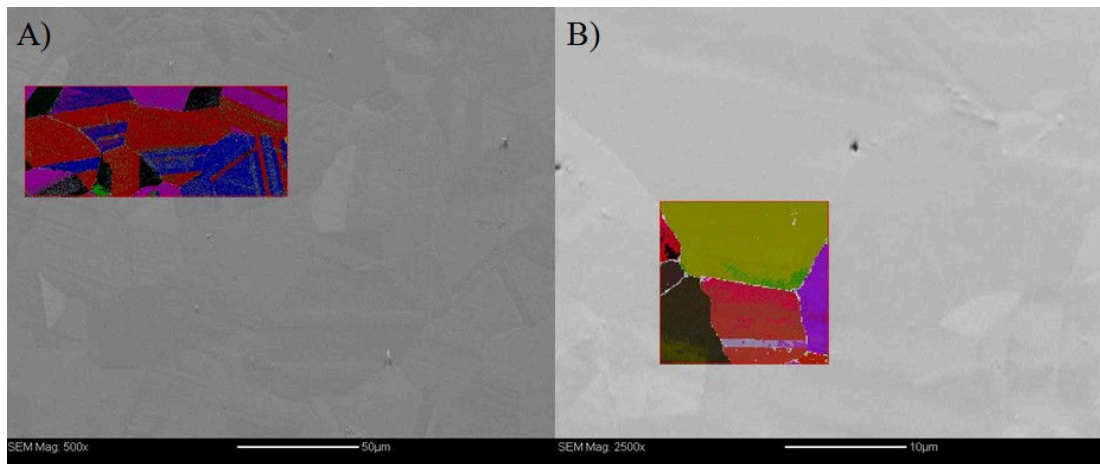
Source: the author.

Figure 31 - EBSD map of the phases for the alloy AL-6XN PLUS™ heat treated at 760 °C for 72 h.
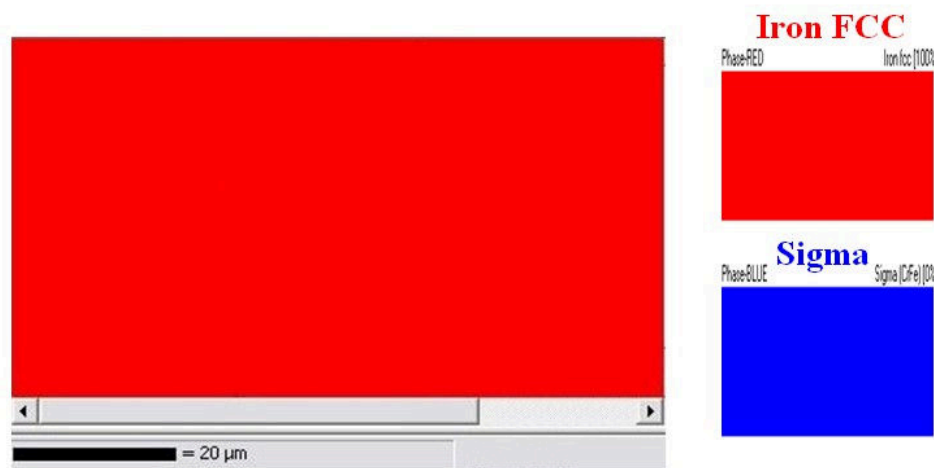
Source: the author.

As no sigma phase was detected for the heat treatment at 760 °c for 72h, another condition was tested. As shown in Figure 26, between 500 °C and 650°C, the sigma content reaches its maximum value. In this case, the new heat treatment was carried out at 600 °C for 120 h. Vach *et al* investigated three austenitic stainless steels (18Cr–8Ni, 18Cr–10Ni, 21Cr–30Ni), used for long-term applications at temperatures between 600 °C and 800 °C. All the steels were used in industry at elevated temperatures for long periods of time (3, 3.5 and 10 years). Sigma phase was found at 600 °C (VACH *et al*, 2008). Thermodynamic predictions combined with experimental techniques were also used by the authors. Time is an important

parameter when working with phase transformations. Villanueva *et al* studied sigma phase precipitation in three different types of stainless steels (austenitic, ferritic and duplex). In ferrite and duplex stainless steels, sigma precipitation is fast but in austenitic stainless steels is very slow (VILLANUEVA *et al*, 2006). The authors observed that the tendency towards precipitation of the sigma phase in the three types of the studied steels is placed in the following sequence: duplex > super ferritic > austenitic. According to the authors, in austenitic stainless steels, the formation of sigma phase occurred at austenite grain boundaries, at triple points and inside delta ferrite islands by eutectoid reaction (delta ferrite → sigma + austenite) as depicted in Figure 32 (VILLANUEVA *et al*, 2006).

In literature, different hypothesis have been put forward to explain the formation of sigma phase in austenite. Decarburization of $M_{23}C_6$ could lead to the sigma phase formation (GOLDSCHMIDT, 1948). Grain boundary $M_{23}C_6$ may coalesces with ageing time and when a critical particle size is reached, the carbide breaks down to form sigma phase (LISMER *et al*, 1952). Sigma phase may be formed via a metastable ferrite phase (α') (RESS *et al*, 1949). By studying a wide range of alloy composition and by comparing the data of other workers, Singhal & Martin concluded that sigma is precipitated directly from austenite in alloys with low Ni + Cr ($\leq$ 45 wt%) content, whereas in alloy of high Ni + Cr ($\geq$ 45 wt%) content, sigma forms via metastable ferrite phase (α') (SINGHAL & MARTIN, 1968). According to this hypothesis, in the 316L, 317L and 904L austenitic stainless steels, sigma phase would form directly from austenite whereas for the AL-6XNPLUS™ super austenitic stainless steel, sigma phase would form from metastable ferrite. Table 8 shows the probable formation of sigma phase with or without prior ferrite formation in austenite for different Ni + Cr contents according to the hypothesis of Singhal & Martin (SINGHAL & MARTIN, 1968).

The samples of the studied alloy were heat treated at 600 °C for 120 h. After the heat treatments, the samples were characterized by XRD using Synchrotron Light at the Brazilian Synchrotron Light National Laboratory (LNLS - Laboratório Nacional de Luz Síncrotron).

Figure 32 - Sigma phase precipitation mechanism in 316L stainless steel.

Source: Villanueva, 2006.

Table 8 - Formation of sigma phase according to the hypothesis of Singhal & Martin.

Alloy	Ni (wt %)	Cr (wt %)	Ni + Cr (wt %)	Intermediate α'
316L	10.7	17.2	27.9	No
317L	12.3	17.8	30.1	No
904L	24.3	19.5	43.8	No
AL-6XNPLUS™	25.8	21.8	47.6	Present

Source: the author.

Some works about sigma phase precipitation on austenitic stainless steels for long-term applications exposed to high temperatures were reported in literature. Terada *et al* investigated the effect of precipitation on the corrosion resistance of AISI 316L(N) stainless steel previously exposed to creep tests at 600 °C for periods of up to 10 years. All tested samples also showed susceptibility to pitting and this effect was attributed to sigma phase precipitation at 600 °C (TERADA *et al*, 2008). Tanaka *et al* studied the microstructural evolution and the change in hardness of a 18Cr–8Ni (type 304H) stainless steel during long-term creep at 550-750 °C for up to 180 000 h. $M_{23}C_6$ carbides and sigma phase were detected and these phases influenced the hardening behavior during creep (TANAKA, 2001). Källqvist and Andrén also reported the presence of sigma phase in an austenitic steel (type 347)

exposed between 500 °C and 700 °C for up to 70 000 h (KÄLLQVIST & ANDRÉN, 1999). In all cited works above, sigma phase was detected for long exposure time at 600 °C but none of the authors could inform the time in which sigma phase started to precipitate. In order to observe the precipitation kinetics of sigma phase, a new heat treatment was carried out at 600 °C for a period of time of 960 h. This was the longest heat treatment of this research.

Energy-dispersive X-ray spectroscopy (EDS) measurements were carried out on the surface of the AL-6XN PLUS™ alloy heat treated at 600 °C for 960 h. The sample treated at 600 °C for 960 h was etched with K(OH) 20% for 50 s to reveal sigma phase at grain boundaries. Three different points on the sample surface were chosen for the measurements as shown in Figure 33. A measurement was carried out at the grain boundary (Figure 33a), at the triple point (Figure 33b) and inside the grain (Figure 33c). The results are shown in Table 9. The contents found are approximately the contents of the main elements of the AL-6XN PLUS™ steel. Sigma phase is rich in elements such as Cr, Mo and Ni and no rich phase of these elements was found. Wasnik *et al* identified sigma phase in a 316L steel treated at 500 °C by EDS. Sigma phase was found as a grain boundary precipitate, typically within 100 nm width and 300 nm length and its composition measured in the sigma phase by EDS was approximately 25–30 wt % chromium, 2–4 wt % molybdenum and iron (WASNIK, 2003).

Table 9 - EDS measurement of the main elements at three different positions on the AL-6XN PLUS™ heat treated at 600 °C for 960 h. The positions are at the grain boundary (GB), at the triple point (TP) and inside the grain (G).

EDS measurement				
Element	Series	Content [wt.%]		
		at GB	at TP	inside the G
Cr	K-series	20.47	20.41	21.43
Fe	K-series	47.57	47.32	45.65
Ni	K-series	26.11	25.46	24.85
Mo	L-series	5.85	6.80	8.08

Source: the author.

Figure 33 - EDS measurements on different points of the AL-6XN PLUS™ steel treated at 600 °C for 960 h: a) at the grain boundary, b) at the triple point and c) inside the grain.
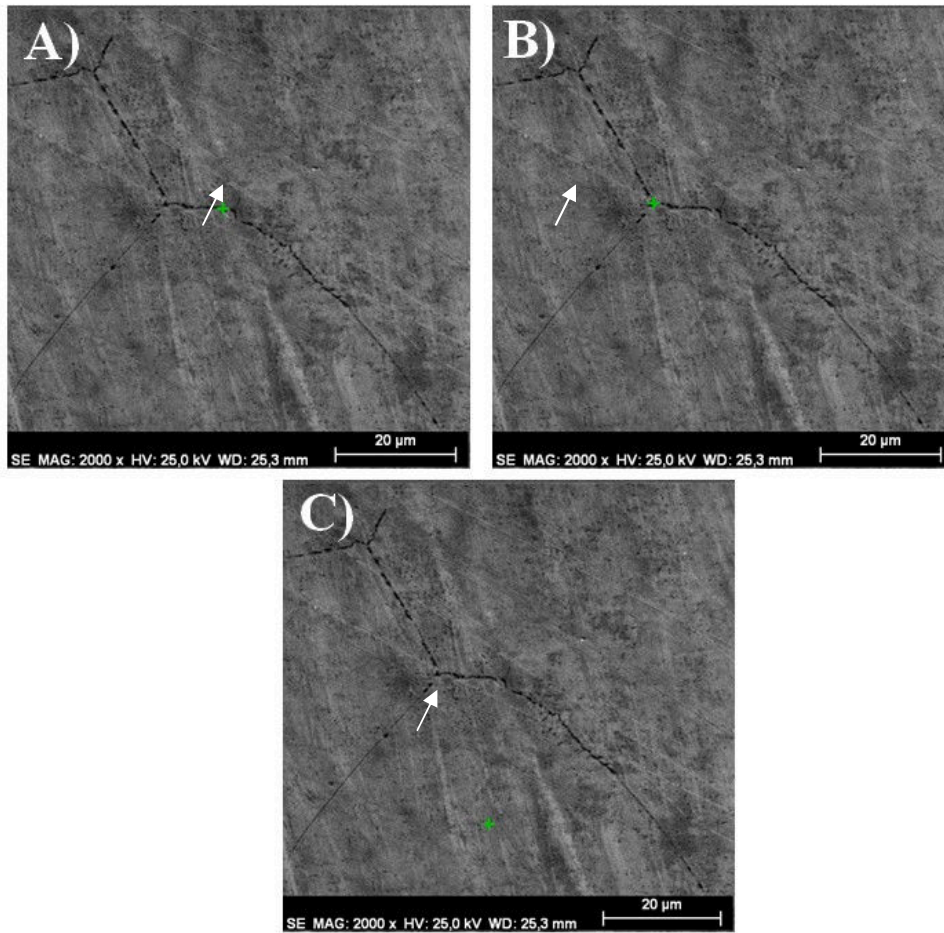
Source: the author.

A region with some grain boundaries and triple points for the measurements was chosen as shown in Figure 34. An EBSD map of the phases of the AL-6XN PLUS™ steel treated at 600 °C for 960 h is shown in Figure 35. No sigma phase was detected confirming the EDS measurements. Only the matrix is present for the selected region. This confirms that the kinetics of the sigma phase is slow in austenitic stainless steels. From the viewpoint of the application of stainless steels, this is a good result because secondary phases as sigma phase are undesirable and decrease the corrosion resistance. This phase has also a detrimental effect on mechanical properties when precipitated on grain boundaries (VACH *et al*, 2008). Sigma phase influences in the mechanical properties by reducing the ductility of the alloys and by

increasing the hardness of high chromium alloy (GILMAN, 1951). This last characteristic caused by sigma phase is a positive one.

Figure 34 - Selected region and the orientation map for the EBSD measurement of the AL-6XN PLUS™ steel heat treated at 600 °C for 960 h.

Source: the author.

Figure 35 - EBSD map of the phases for the AL-6XN PLUS™ steel heat treated at 600 °C for 960 h.
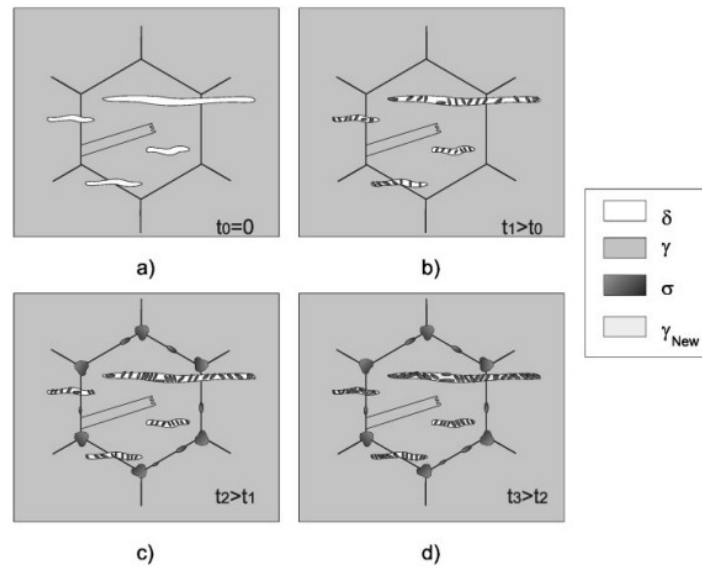

Source: the author.

Figure 36 shows the microstructure of the AL-6XN PLUS™ super austenitic stainless steel after an electrolytic etching with oxalic acid 10 %. It is possible to see the grain boundaries and the twin boundaries. This is a characteristic of the austenitic phase.

As no sigma phase was detected for all the attempts of precipitation, its effect on CO_2 corrosion could not be evaluated.

Figure 36 - SEM image of the microstructure of the AL-6XN PLUS™ super austenitic stainless steel.
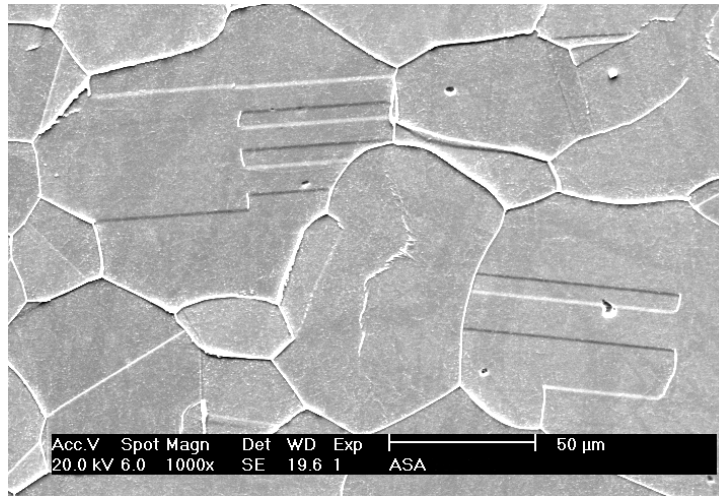
Source: the author.

6.2   X ray diffraction by Synchrotron light

The measurements of XRD using Synchrotron Light were carried out at LNLS. Prior to measurements, the samples of the 316L and AL-6XN PLUS™ steels were heat treated at 600 °C for 120 h in the form of sheet metal. The specimen were manufactured according to TMEC Project - Gleeble. The samples were named J3 and C3, respectively. Figure 37 shows the X-ray diffractogram pattern for the sample J3. The angle 2θ was measured between 20° and 80°. This interval is enough to detect the sigma phase peaks. A synchrotron light radiation source ($\lambda = 0.10332$ nm) was used. Austenite peaks (FCC) and some ferrite peaks (BCC) on the diffractogram pattern of sample J3 were observed as seen in Figure 37. Sigma peaks were supposed to be detected for 2θ between 25° and 35° but no sigma peaks were found. All the peaks on the diffractogram were identified and the result is shown in Table 10. It was used a database called Joint Committee for Powder Diffraction Data (JCPDS) belonging to ICDD database (International Centre for Diffraction Data). The peaks obtained experimentally and the expected peaks were compared in Table 10. The difference between them is in the order of 0.1°- 0.8° and confirms the presence of austenite and ferrite peaks.

Figure 37 - Diffractogram pattern for the sample 316L treated at 600°C for 120 h Synchrotron light radiation source ($\lambda = 0.10332$ nm).
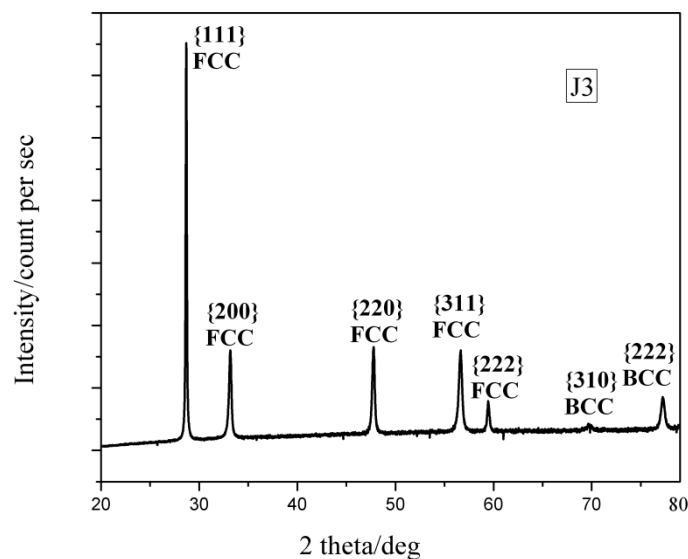
Source: the author.

Table 10 - Comparison between the obtained and expected 2θ for sample 316L treated at 600 °C for 120 h. Synchrotron light radiation source (λ = 0.10332 nm).

Sample/phase	{hkl}	2θ/deg expected	2θ/deg obtained	Δ(2θ/deg) In modulus	PDF number
J3 /Austenite	111	28.76	28.64	0.12	23-0298
	200	33.36	33.21	0.15	
	220	48.00	47.77	0.23	
	311	56.98	56.63	0.35	
	222	60.20	59.40	0.80	
	400	70.06	-	-	
J3 /Ferrite	110	29.53	-	-	06-0696
	200	42.25	-	-	
	211	52.40	-	-	
	220	61.30	-	-	
	310	69.49	69.78	0.29	
	222	77.26	77.23	0.03	

Source: the author (ICDD database, 2000).

The result for the sample C3 heat treated at 600 °C for 120 h is shown in Figure 38. The result is similar to the result of the sample J3. Only austenite and ferrite peaks were found on its diffractogram pattern. No sigma peaks were detected. The presence of ferrite in austenite suggests that the sigma phase could precipitate by an eutectoid reaction as suggested by Villanueva et al (VILLANUEVA et al, 2006). On continued heat treatment, the formation of sigma phase could take place by the dissolution of neighboring ferrite particles. Sigma phase particles could grown and thicken preferentially in those regions lying very close to adjacent ferrite crystals as observed by Singhal and Martin in austenitic stainless steels (SINGHAL & MARTIN, 1968). The authors state that, after a heat treatment of the order of 1500 h, ferrite precipitates at the grain boundaries for austenitic stainless steels and the ferrite is replaced by sigma phase precipitates. Inclusions serve as effective sites for the nucleation of ferrite and this inclusions, according Singhal and Martin, could be mainly $M_{23}C_6$. From their results, it was clear that the prior precipitation of $M_{23}C_6$ is not essential for sigma formation. The authors also state that when sigma particles were observed during the earlier stage of their appearance, these particles present similar shapes and growth directions as some of the ferrite precipitates. This suggests an in situ transformation of some existing ferrite precipitates to sigma (SINGHAL & MARTIN, 1968).

Figure 38 - Diffractogram pattern for the sample AL-6XN PLUS™ treated at 600 °C for 120 h. Synchrotron light radiation source (λ = 0.10332 nm).
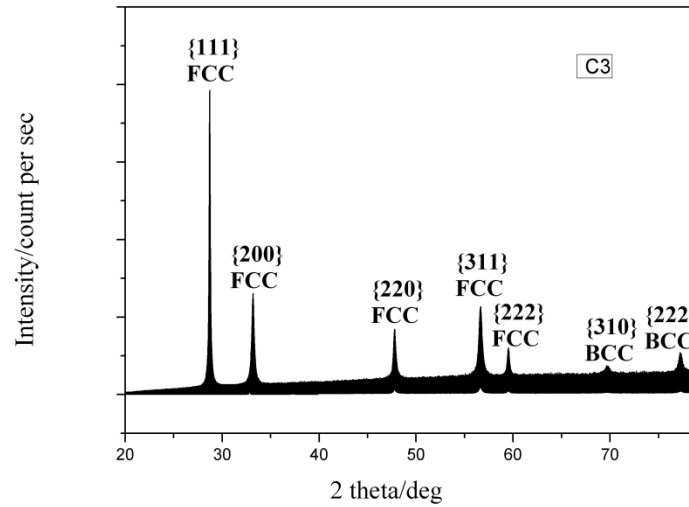
Source: the author.

The peaks obtained experimentally were compared with the expected ones and the result is shown in Table 11.

Table 11 - Comparison between the obtained and expected 2θ for sample AL-6XN PLUS™ treated at 600 °C for 120 h. Synchrotron light radiation source (λ = 0.10332 nm).

Sample/phase	{hkl}	2θ/deg expected	2θ/deg obtained	Δ(2θ/deg) In modulus	PDF number
C3 /Austenite	111	28.76	28.67	0.09	23-0298
	200	33.36	33.12	0.24	
	220	48.00	47.84	0.16	
	311	56.98	56.64	0.34	
	222	60.20	59.54	0.66	
	400	70.06	-	-	
C3 /Ferrite	110	29.53	-	-	06-0696
	200	42.25	-	-	
	211	52.40	-	-	
	220	61.30	-	-	
	310	69.49	69.75	0.26	
	222	77.26	77.19	0.07	

Source: the author (ICDD database, 2000).

A sample of the AL-6XN PLUS™ steel heat treated at 600 °C for 72h was also tested. The sample was named C2. The diffractogram pattern for this sample is shown in Figure 39. The result is similar compared with the heat treated sample C3. It was also detected the matrix (austenite) and also ferrite but no sigma phase was detected. The comparison of the peaks is shown in Table 12.

Figure 39 - Diffractogram pattern for the sample AL-6XN PLUS™ in the as received condition. Synchrotron light radiation source (λ = 0.10332 nm).
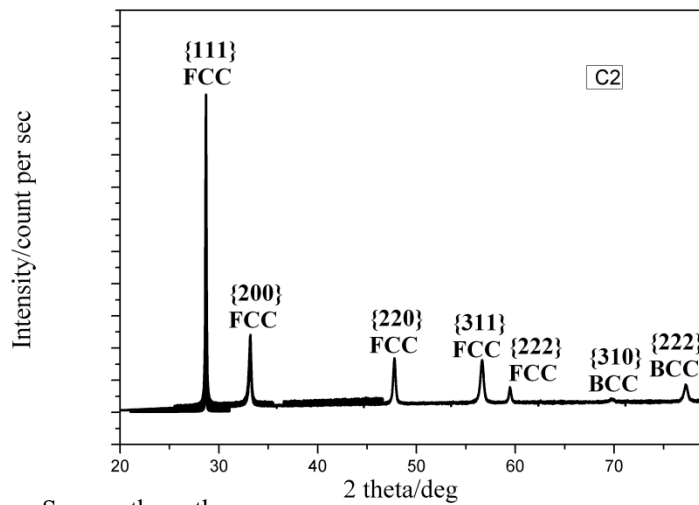
Source: the author.

Table 12 - Comparison between the obtained and expected 2θ for sample AL-6XN PLUS™ in the as received condition. Synchrotron light radiation source (λ = 0.10332 nm).

Sample/phase	{hkl}	2θ/deg expected	2θ/deg obtained	Δ(2θ/deg) In modulus	PDF number
C2 /Austenite	111	28.76	28.67	0.09	23-0298
	200	33.36	33.24	0.15	
	220	48.00	47.84	0.23	
	311	56.98	56.64	0.35	
	222	60.20	59.47	0.80	
	400	70.06	-	-	
C2 /Ferrite	110	29.53	-	-	06-0696
	200	42.25	-	-	
	211	52.40	-	-	
	220	61.30	-	-	
	310	69.49	69.71	0.22	
	222	77.26	77.25	0.01	

Source: the author (ICDD database, 2000).

A new heat treatment was carried out with the samples C3. As the samples was heat treated at 600 °C for 120 h, the new heat treatment was an *in situ* experiment at 700 °C during 10.5 h. The sample C3 was named C4 for the new condition. Two detectors were used to scan the sample during the *in situ* experiment. Ten images acquisition were acquired on the sample during the experiment. The objective of this new heat treatment was to precipitate sigma phase by increasing temperature from 600 °C to 700 °C. The temperature during the *in situ* experiment was measured by a thermocouple type K (alumel–chromel). The heating rate was 100°C/min. The temperature was held constant during all the experiment. Three X-ray measurements were carried out during the experiment. Figure 40 depicts the steps of these measurements. The heat treated sample was heated by joule effect from room temperature to 700 °C. When the temperature reached the value of 700 °C, the first scan was carried out. In the middle of the experiment, around 5 hours, another scan was carried out to compare with the first one. In the end of the *in situ* experiment, a last scan was carried out and the result is shown in Figure 41. The first and the second scans are very similar to the third scan. No sigma phase was detected, only austenite and ferrite. This technique does not detect sigma phase for values less than 5%.

Figure 40 - Behavior of the temperature with time during the *in situ* experiment.
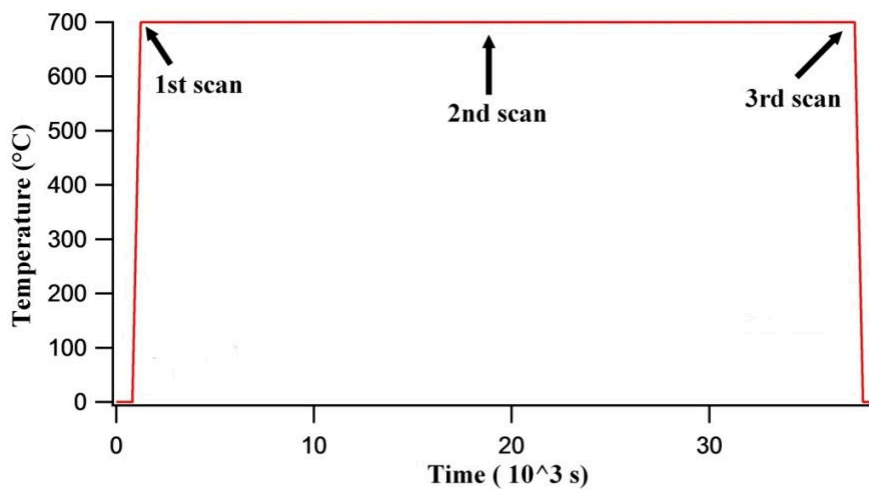
Source: the author.

Figure 41 - Diffractogram pattern of the *in situ* experiment for the third scan (AL-6XN PLUS™). Synchrotron light radiation source ($\lambda = 0.10332$ nm).

Source: the author.
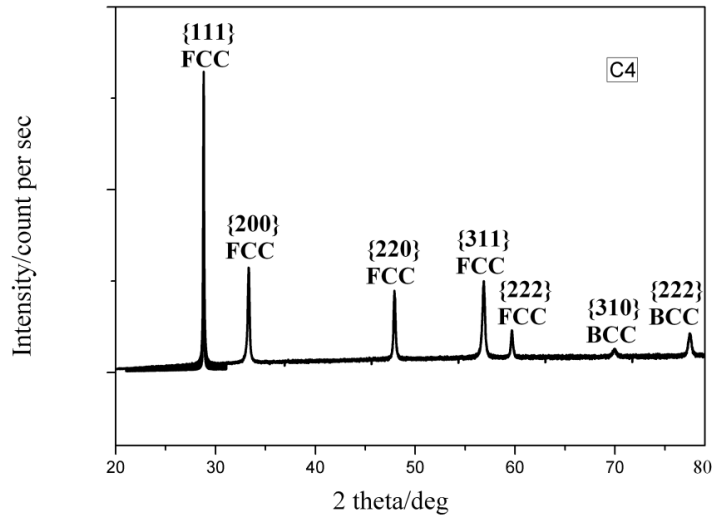
       Figure 42 shows the scheme of the *in situ* experiment plotted by IgorPro6.22A software. It is a map with 4 graphics: the 1st graphic is the diffractogram, the 2nd graphic is the behavior of temperature versus time, the 3rd graphic is a reading cross section as seen by the laser dilatometer, and the 4th graphic is the applied force versus time. As no force was applied in this experiment, the value for the applied force is around zero (the noise on the 4th graphic is due to the dilatation of the sample that causes compression on the gleeble). On the diffractogram pattern one can see the 10 images acquisitions acquired during the experiment. The images acquisitions were acquired by two detectors between 28° and 49°. The 1st detector acquired images between 27° and 38° and the second one between 39° and 49°. The space between the detectors corresponds to an interval of 1°. The identified peaks are shown as a colorful spectra. The more intense the peaks, brighter is the spectrum. The peaks identified on the diffractogram pattern are austenite (111), austenite (200), and austenite (220). Figure 43 shows the diffractogram pattern for the colorful spectrum. No sigma phase and no ferrite phase were detected.

Figure 42 - Map with the graphics of the *in situ* experiment (temperature x time, laser x time, force x time).
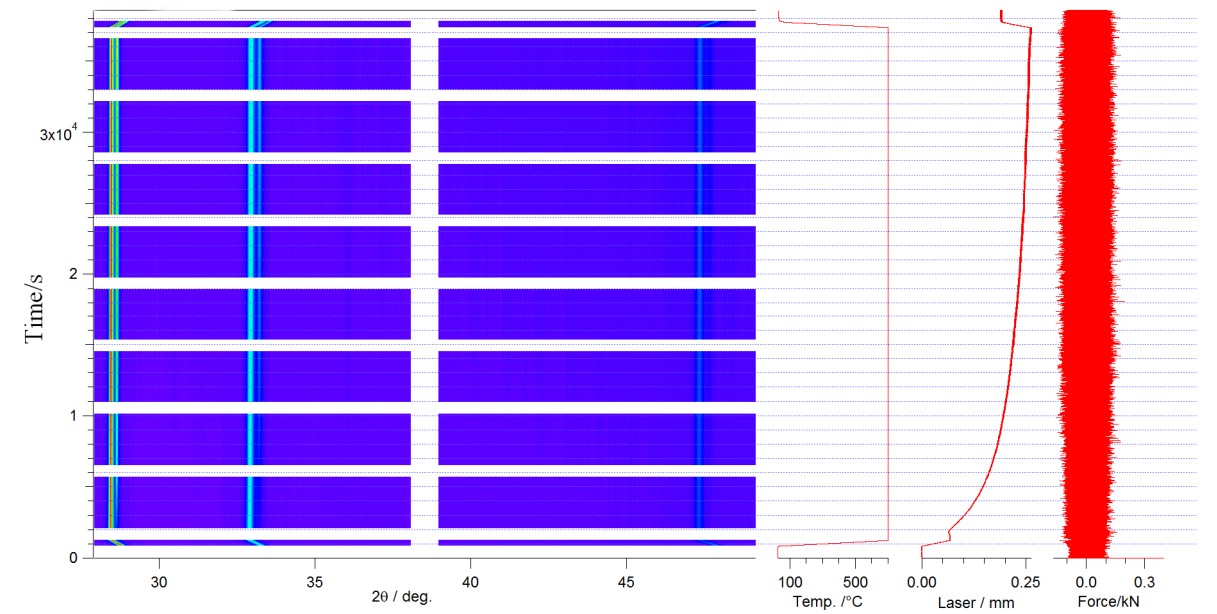
Source: the author.

Figure 44 shows the sample C4 (AL-6XN PLUS™) after the experiment. One can see a colorful spectrum caused by the *in situ* heat treatment.

Figure 43 - Diffractogram pattern of the *in situ* experiment (sample AL-6XN PLUS™) for the region of the colorful spectrum. Synchrotron light radiation source ($\lambda = 0.10332$ nm).
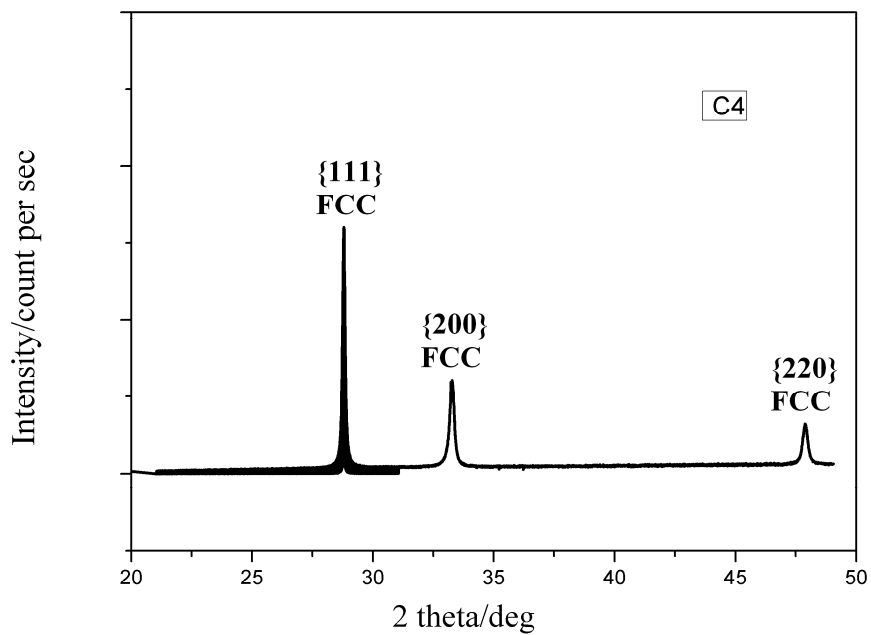
Source: the author.

Figure 44 - Photograph of the sample C4 (AL-6XN PLUS™) after the *in situ* experiment showing the heating zone.
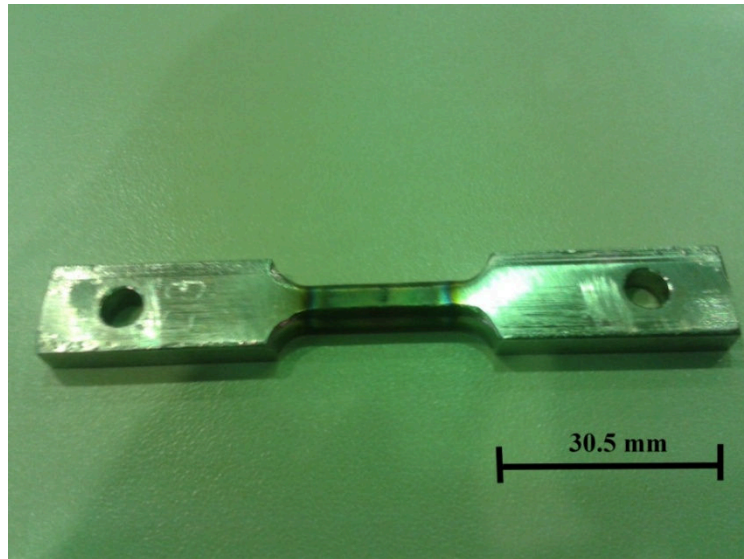
Source: the author.

The results of XRD using Synchrotron Light as source showed the presence of ferrite in the samples suggesting that the hypothesis of sigma phase precipitation could take place if the ferrite phase suffered dissolution. The times of the heat treatments were not enough to give the appropriate driving force for ferrite to precipitate in a considerable amount allowing the sigma phase precipitation. Even present on the microstructure of the alloys, the *in situ* experiment was not enough to continue the ferrite growth and, therefore, the sigma phase precipitation which is a good result when working with austenitic stainless steels at high temperatures for long periods of time that do not reach the time of sigma phase initiation.

6.3   Potentiodynamic cyclic polarization tests

The cyclic polarization tests are designed to evaluate pitting corrosion by the appearance of hysteresis curves during the polarization. This electrochemical technique also has the purpose of comparing the susceptibility to localized corrosion in metallic materials that passivate (STEPHEN TAIT, 1994). Figure 45 shows the cyclic polarization curves for the samples in the as-received condition in aqueous solution of CO_2-saturated synthetic oil field formation water. The potential sweep was from -0.50 V to +1.14 V from OCP.

Figure 45 - Cyclic polarization curves for the alloys in the as-received condition in CO_2-saturated synthetic oil field formation water.
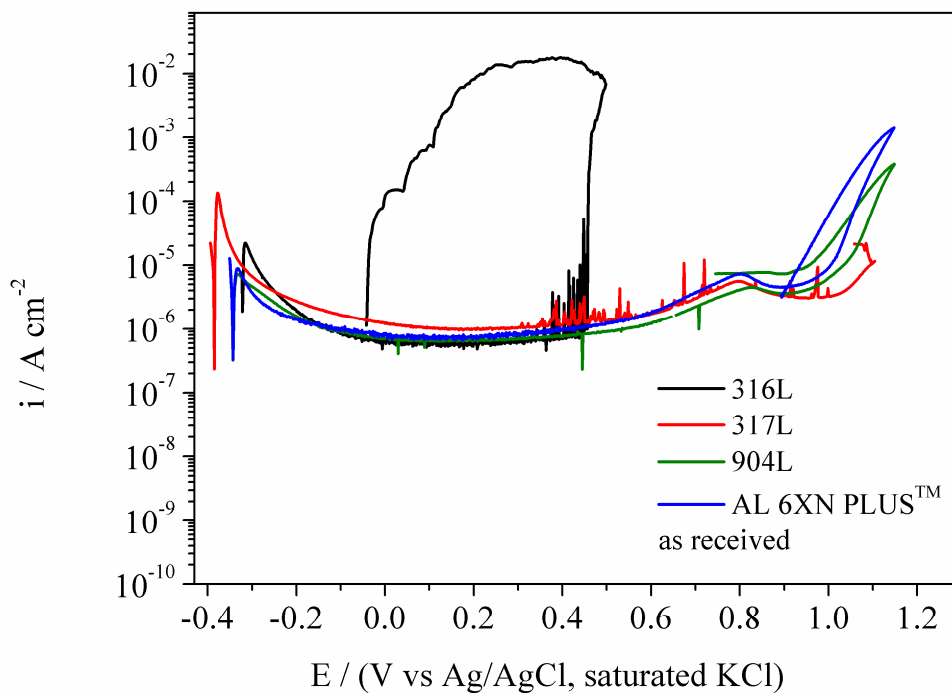
Source: the author.

The AL-6XN PLUS™ and 904L super austenitic stainless steels showed a good resistance to CO_2 corrosion. After reaching the corrosion potential (around -0.34 V), there was the formation of a passive layer. The current density in the passive region for both steels possesses order of magnitude of 10^{-7} A/cm² indicating the passivation for the super austenitic alloys. Around the potential of +0.80 V there was an increase in current density indicating a slight breakdown of the passive film followed by a repassivation. After reaching the potential of +0.97 V, there was an increase of current density, i.e the transpassive region is reached.

The potential is too high (above +1.0 V). It is possible to observe that the electrochemical behavior for the two super austenitic steels in CO_2-saturated aqueous solution are very similar. The passive regions are quite stable. Reverse curves showed no hysteresis indicating no localized corrosion. The increase of current density after the potential of +1.01 V on the cyclic polarization curves for the super austenitic steels is associated with water dissociation (oxygen evolution) according to equation 6. With the release of the oxygen gas from the water molecule, there is the continuation of the oxidation process on the sample surface. According to Bandy & Cahoon (BANDY, R. and CAHOON, J. R, 1977), with this type of reaction occurring, it is impossible to distinguish the current due to the metal corrosion from the current of the water dissociation leaving the electrochemical tests limited for very high potentials (above +1.0 V).

$$2H_2O \rightarrow O_2 + 4H^+ + e^- \qquad \text{(eq. 6)}$$

The cyclic polarization curve for the 316L steel also presented the same passivation like the super austenitic steels (order of magnitude of 10^{-7} A/cm²), however, between the potential of +0.36 V to +0.45 V the curve presented a noise indicating fragility of the passive film. In high chloride concentration solutions, the pit is characterized by a minimum potential, called pitting potential. Below this potential, the metal remains passivated and, above it, pits are formed, which is a criterion used for their detection, although a detailed examination of the passive region shows that the passivation current is noisier in chloride solutions than in solutions in which this ion is absent (PICON *et al*, 2010). This effect can be seen in Figure 45 for the 316L and 317L alloys. After reaching the potential of +0.45 V (pitting potential), the passive film of the 316L alloy was broken and there was a sudden increase in current density with high values (order of magnitude of 10^{-3} A/cm²). The reverse curve showed hysteresis indicating pits formation on the surface of the 316L steel. The hysteresis curve closed at the potential of -0.039 V. Therefore, the formation of a positive hysteresis showed that the 316L steel did not show a good CO_2 corrosion resistance in the electrolyte used.

Cyclic polarization curve of the 317L steel showed a similar behavior like the curves of the super austenitic steels. Its passive region is stable. Between the potentials of +0.35 V and +0.56 V, the passive film showed instability (noise on the polarization curve), but the film resisted well. Next to the potential of +0.80 V there was a slight increase in the current density followed by a repassivation. After the potential of +1.0 V there was an

increase of current density. This increase is related to oxygen evolution as discussed before. There was no hysteresis formation for the 317L steel.

The AL-6XN PLUS™ and 904L super austenitic steels and the conventional AISI 317L stainless steel exhibited a good corrosion resistance in CO_2-saturated aqueous solution. This result showed that the passive film of the AL-6XN PLUS™ , 904L and 317L alloys is more stable. According to Sedriks, in a polarization curve, the greater the difference between the break potential (E_b) and the corrosion potential (E_{corr}), more resistant to several forms of corrosion the material is (SEDRIKS, 1996). Equation 7 shows the relationship described by Sedriks to evaluate the corrosion resistance.

$$\Delta E = E_b - E_{corr} \qquad \text{(eq. 7)}$$

Table 13 shows the values for the corrosion potential, break potential (pitting potential for the 316L steel) and the difference between them for the studied alloys in the as received conditions. These values were taken from the cyclic polarization curves. The values of ΔE are higher for the super austenitic stainless steels confirming their high performance in relation to CO_2 corrosion. 316L steel showed the lowest value for ΔE indicating not be a suitable material for applications requiring good resistance to CO_2 corrosion.

Table 13 – Table with the potentials E(corr), E(b) and ΔE in volts (Ag/AgCl, sat KCl).

Alloys	E(corr)	E(b)	ΔE
316L	-0.32	+0.45	0.77
317L	-0.38	+0.99	1.37
904L	-0.34	+0.98	1.32
AL-6XN PLUS^{TM}	-0.34	+0.98	1.32

Source: the author.

The micrographs of the steels after CO_2 corrosion tests are shown in Figure 46. One can see clearly the pits formed on the surface of the 316L steel. This explains the appearance of hysteresis in its polarization curve. The pits on stainless steels are generally spaced apart and most of the surface is passive. However, the pitting propagation speed is very fast (ISAACS *et al*, 1990; PISTORIUS & BURSTEIN, 1992). The surface of the AL-6XN PLUSTM and 904L super austenitic steels as well as the 317L austenitic steel showed no pits on their surfaces. These results are in agreement with the cyclic polarization curves

with the absence of hysteresis. The pits formed on the surface of the 316L steel are not uniform and their tendency is to grow even more with time. Figure 47 shows a specific pit on the surface of the 316L steel. One can see the total destruction of the material in the center of the pit and around the center, other micro pits in growth state. The direction of pit growth is from the center to the edges.

Figure 46 - SEM images of the alloys surfaces in the as-received condition after the cyclic polarization tests in CO_2-saturated aqueous medium. A) 316L, b) 317L, c) 904L e d) AL-6XN PLUS^{TM}.
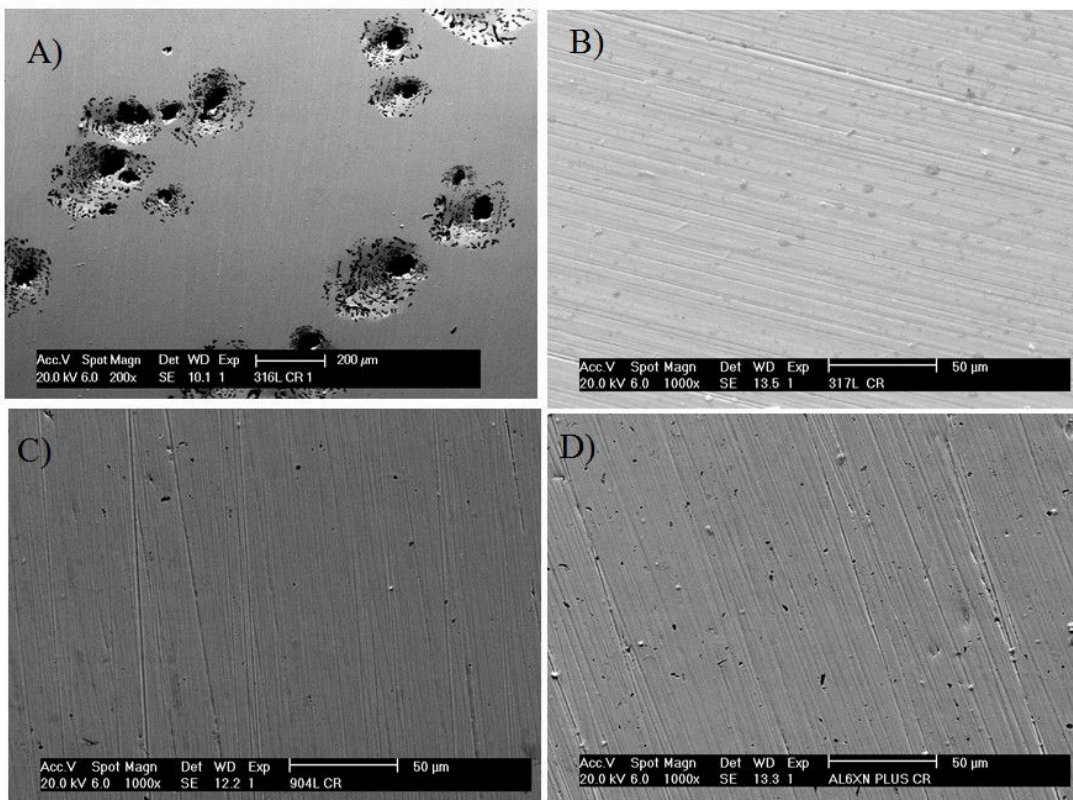
Source: the author.

The pits formed on the surface of the 316L steel sustain by themselves perforating the material. With the breaking of the passive layer, an electrolytic cell is formed. The cathode region is the passive layer while the anode is the exposed metal, more precisely, the center of the pit. The flow of electrons between the anode and cathode is due to a large potential difference between these two regions. The corrosion process in this case is accelerated into the pit.

Figure 47 - SEM image of a specific pit on the surface of the 316L steel after the cyclic polarization tests in CO_2-saturated aqueous medium.
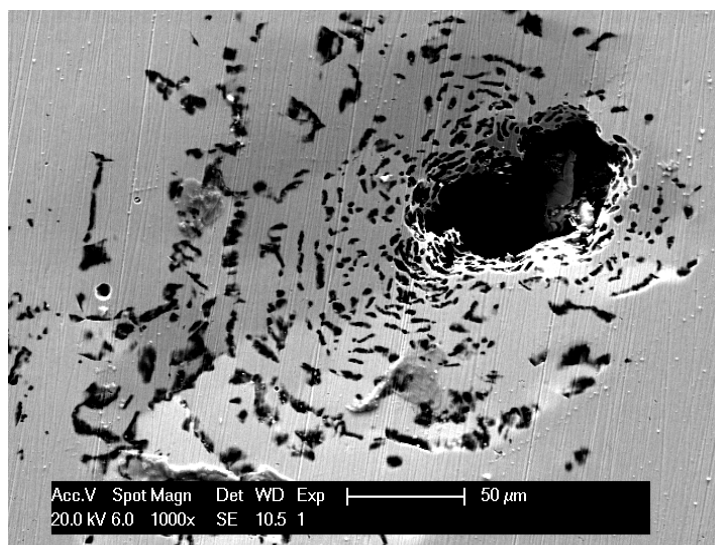
Source: the author.

Figure 48 shows the cyclic polarization curves for the heat treated samples at 760 °C for 72 h. The solution used in this experiment was again CO_2-saturated synthetic oil field formation water deaerated with N_2. The 316L and 317L steels showed similar behavior on their polarization curves. After reaching the corrosion potentials, -0.49 V and -0.40 V respectively, both of the steels suffered passivation. The passive region is the portion of the curves between the passivation potential and the pitting potential. The films broke at +0.44 V and +0.45 V, respectively. After reaching these potentials, the current densities for both of the steels rose abruptly until the current density reached magnitude of 10^{-3} A/cm². After that, there was the hysteresis formation for both of the steels indicating localized corrosion. The 904L and AL-6XN PLUS™ super austenitic stainless steels showed again a good corrosion resistance in CO_2-saturated aqueous solution. There was no hysteresis formation in their cyclic polarization curves.

Figure 49 shows pits on the surface of the 316L steel after the CO_2 corrosion tests. As in the as-received condition, the heat-treated samples of the 316L steel were also susceptible to pitting corrosion in CO_2-saturated aqueous solution. Of all reactants of the TQ3219 solution, the sodium chloride is in larger quantity. Sodium chloride was responsible for pitting corrosion. The CO_2 gas bubbled into the solution accelerated the process.

Figure 48 - Cyclic polarization curves for the heat treated alloys at 760 °C for 72 h. The solution used was CO_2-saturated synthetic oil field formation water.
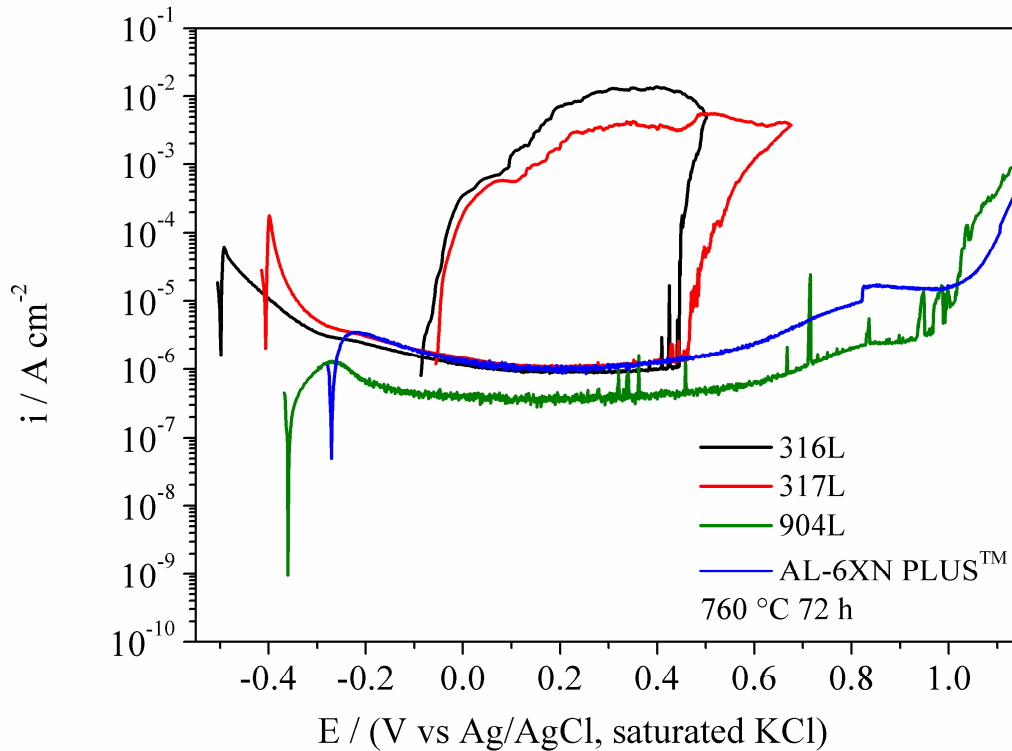
Source: the author.

Figure 50 shows the surface of 317L steel after CO_2 corrosion test. The type of localized corrosion suffered by the steel 317L was crevice corrosion. This is a susceptibility of this steel to this form of corrosion. In this case, the crevice formed between the lacquer used to reduce the active area and the exposed area of the sample as seen in Figure 51. This justifies the hysteresis formed on the polarization curve once this steel is resistant to pitting corrosion. The passive film was broken at the potential of +0.47 V. This is the crevice potential for the 317L steel and it is very close to the pitting corrosion of the 316L steel (+0.44 V). There was no formation of pits on the surface of the 317L steel. The crevice formation is also not related to the heat treatments. Crevice corrosion occurs when there is a potential difference between the metal and the free surface regions with geometric limitations due to the difference in concentration of chemical species between these two regions. The 316L steel is susceptible to pitting corrosion and also to crevice corrosion as shown in Figure 51. Hua-Bing *et al*. studied the effect of nitrogen on pitting and crevice corrosion of austenitic stainless steels in chloride solution and they concluded that the resistance to this type of

corrosion (pitting and crevice) is also attributed to the enrichment of nitrogen on the surface of passive films facilitating repassivation (HUA-BING Li *et al*, 2009). They also concluded that with increasing the nitrogen content in steels, pitting potentials and critical pitting temperature (CPT) increase and the maximum average pit depths and average weight loss decrease. The results showed that the 316L is susceptible to pitting corrosion and also to crevice corrosion. The 317L steel is resistant to pitting corrosion but susceptible to crevice corrosion in chloride-containing environments.

Figure 49 - Optical microscopy image of the surface of the steel 316L heat treated at 760 °C for 72 h after CO_2 corrosion test.
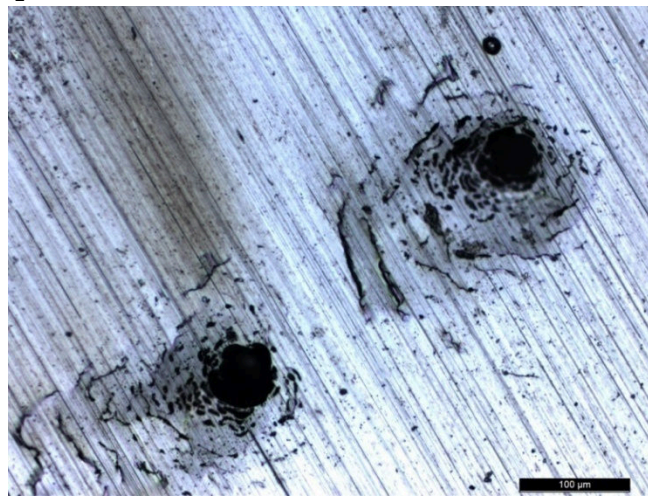
Source: the author.

Figure 50 - Optical microscopy image of the surface of the steel 317L heat treated at 760 °C for 72 h after CO_2 corrosion test. Presence of crevices between the exposed area and the lacquer are shown.
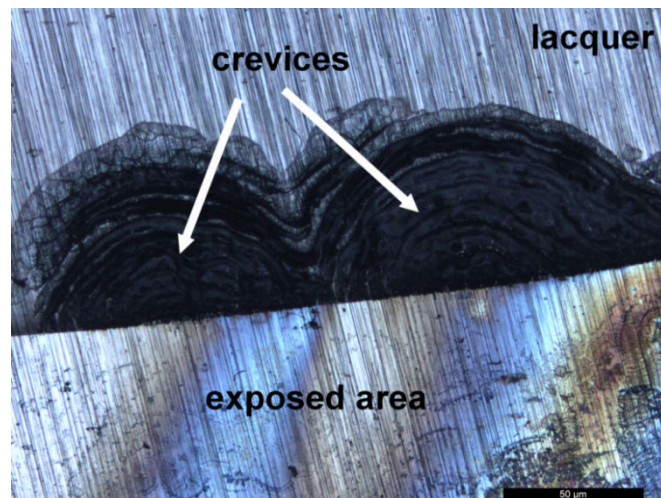
Source: the author.

Figure 51 - Optical microscopy image showing the appearance of pitting (a) and crevice (b) corrosion on the non-protected/protected region covered with lacquer for the 316L steel heat treated at 760 °C for 72 h.
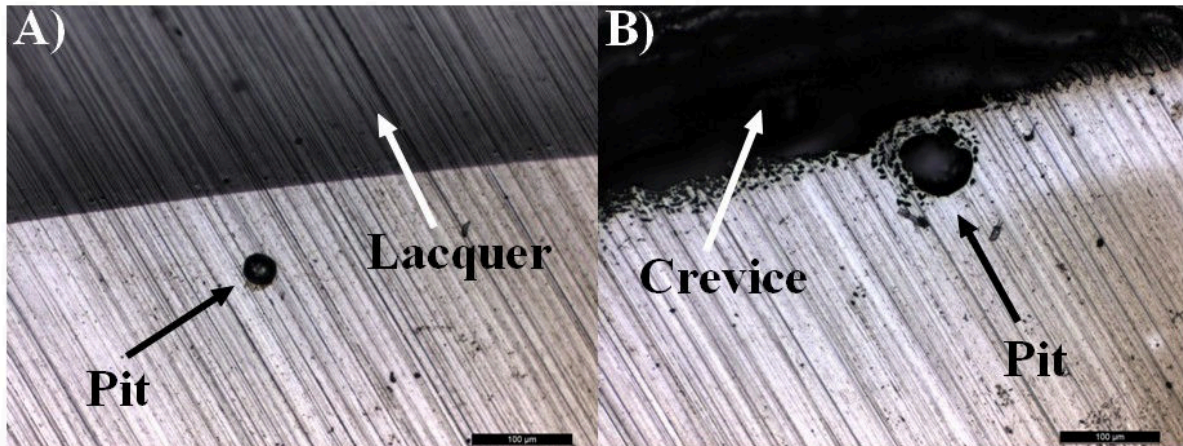
Source: the author.

Figure 52 shows the cyclic polarization curves for the steels in the as-received condition in an aqueous medium of synthetic oil field formation water. The solution was deaerated again with nitrogen, but not saturated with CO_2. The solution was basic (pH = 8.1). All samples suffered passivation with low current densities. The polarization curve for the sample of the 316L steel showed again hysteresis indicating localized corrosion. The absence of CO_2 in the solution caused the displacement of the pitting potential to more noble direction (more positive) leaving the alloy more resistant to localized corrosion. However, at the potential of +0.73 V there was the breakdown of the passive film followed by a high increase of the current density and subsequent formation of pits on the sample surface. The other polarization curves showed no hysteresis indicating no localized corrosion. The AL-6XN PLUS™ and 904L super austenitic stainless steels showed again a good corrosion resistance in the aqueous medium of synthetic oil field formation water. The conventional 317L austenitic steel also exhibited a good corrosion resistance in this medium like the super austenitic ones. Noises on its polarization curve was detected between the potentials of +0.21 V and +0.80 V. These noises are associated with the breakdown of the passive film and its prompt repassivation (GRABKE, 1996).

Figure 52 - Cyclic polarization curves for the alloys in the as-received. The solution used was aerated synthetic oil field formation water without bubbling CO_2.
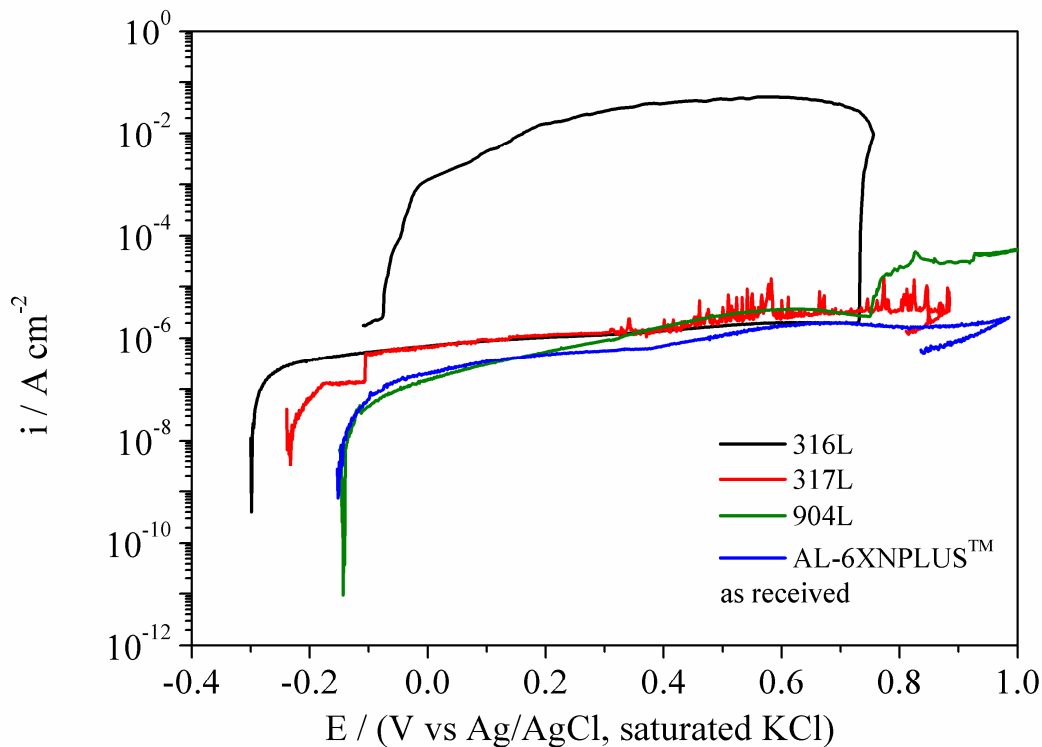
Source: the author.

Figure 53 shows the pits on the surface of the 316L steel after the cyclic polarization test in an aerated aqueous solution without bubbling CO_2. Figure 53a shows an overview of the steel surface and Figure 53b shows the shape of the pit. Even in a basic solution, the 316L steel is still susceptible to pitting corrosion, however the pit density on the surface of the sample in the as-received condition in aqueous solution with no CO_2 is lower than the pit density on the surface of the sample in the same condition in CO_2-saturated aqueous solution as can be seen in Figure 54. The pits tend to grow from the center to the edges. The destruction is confined to small areas on the order of square millimeters or less, resulting in holes that penetrate the metal leaving the most part of the surface intact as can be seen in Figure 53a. The presence of these pits is related to aggressive ions such as chloride (Cl^-) as discussed before. The same metal can present different pitting potential in different anions, but generally, chloride ion is the most aggressive of all, since it takes to low pitting potentials and it is also the most abundant ion in nature (GALVELE, 1983).

Figure 53 - SEM images of pits on the surface of the 316L alloy. The pits are smaller in aqueous medium with no CO_2.
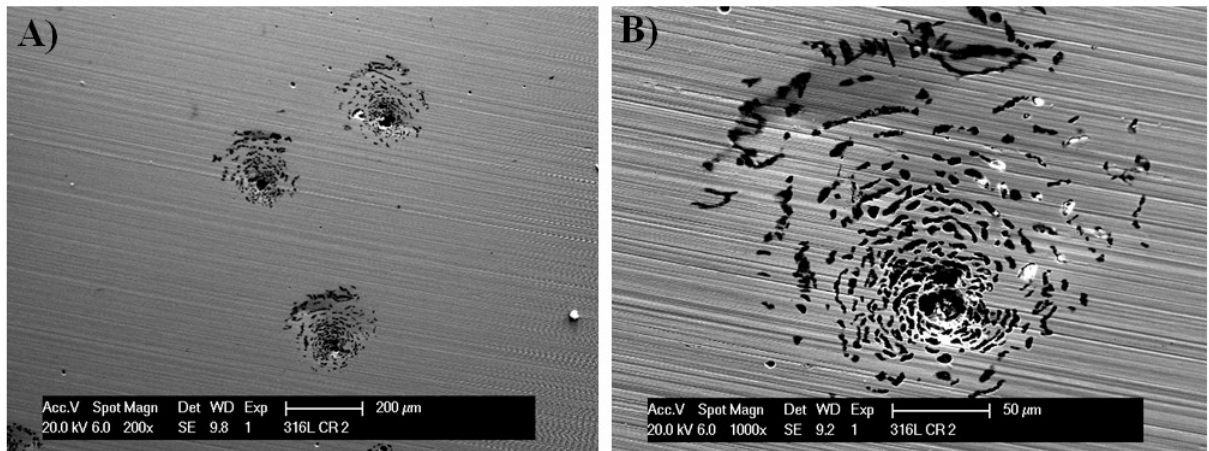
Source: the author.

Figure 54 shows a comparison of pit density on the surface of the 316L steel in the as-received condition in aerated CO_2-saturated aqueous solution (Figure 54a) and without CO_2 (Figure 54b). In the first case, the pit density on the surface of the 316L steel in the as-received condition is greater than the pit density in the second case. Generally, CO_2 dissolves in water to form carbonic acid (H_2CO_3). The pH of the solution changes from basic to acid, so the chloride containing environment turns into more aggressive. The pitting potential also changes as seen in Table 14.

Figure 54 - SEM images of the pit density for the alloy 316L in the as-received condition in an aqueous medium (TQ3219) a) with CO_2 and b) without CO_2.
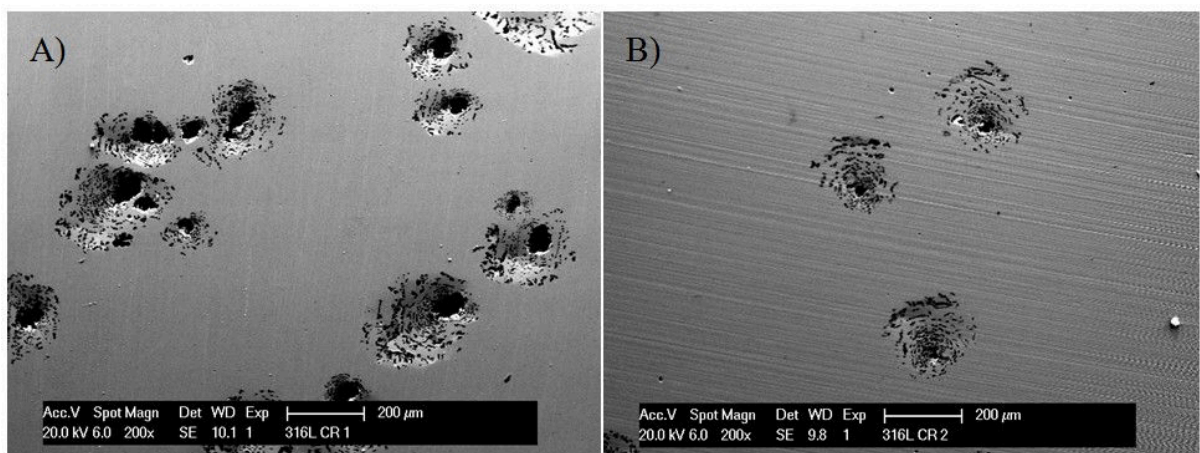
Source: the author.

The pitting potential is a function of the medium composition, concentration of aggressive ions, temperature, alloy composition and the surface treatment (PICON *et al*, 2010). In Table 14, the values of pitting potential (E_p) and pitting corrosion (E_{corr}) for the 316L alloy are shown as a function of the pH and temperature. The pH of 5.2 means that the solution TQ3212 was saturated with CO_2 (acid solution) and for the pH of 8.1, the solution was not bubbled with CO_2 (basic solution). As seen in Table 14, the E_p is greater in basic solutions than in acid ones as expected. It seems that the pH of the solution had also influence on the size and density of the pits as shown in Figure 54. The E_{corr} suffered influence of the heat treatments. For the as-received condition, the E_{corr} was more noble than for the heat treated samples. The E_{corr} is a thermodynamic parameter and indicates when the corrosion processes starts. The heat treatments did not influence the E_p.

Table 14 - Change of the pitting potential and the corrosion potential of the alloy 316L measured in V vs Ag/AgCl sat KCl.

316L alloy			
pH	condition	E_p	E_{corr}
5.2	as-received	+0.45	-0.32
8.1	as-received	+0.72	-0.30
5.2	760 °C for 72 h	+0.43	-0.49
5.2	600 °C for 960 h	+0.44	-0.54

Source: the author.

The pH of the solution is influenced by carbon dioxide gas. The corrosion rate tends to be lower when the solution is basic and this explains the corrosion behavior of the alloys in all polarization curves. When bubbling the solution with carbon dioxide gas, the hydration of carbon dioxide occurs and the carbonic acid (H_2CO_3) is formed. This is the CO_2 corrosion mechanism. The pH of the solution changes from basic to acid values due to carbonic acid presented in the solution. Anselmo *et al* studied the corrosion behavior of super martensitic stainless steel in CO_2-saturated synthetic seawater (ANSELMO *et al*, 2006). The author also studied the effect of bubbling CO_2 in the synthetic seawater and the result can be seen in Figure 55. The same result was found in this work when bubbling the solution with CO_2.

Figure 55 - pH of synthetic seawater as a function of CO_2 bubbling time.
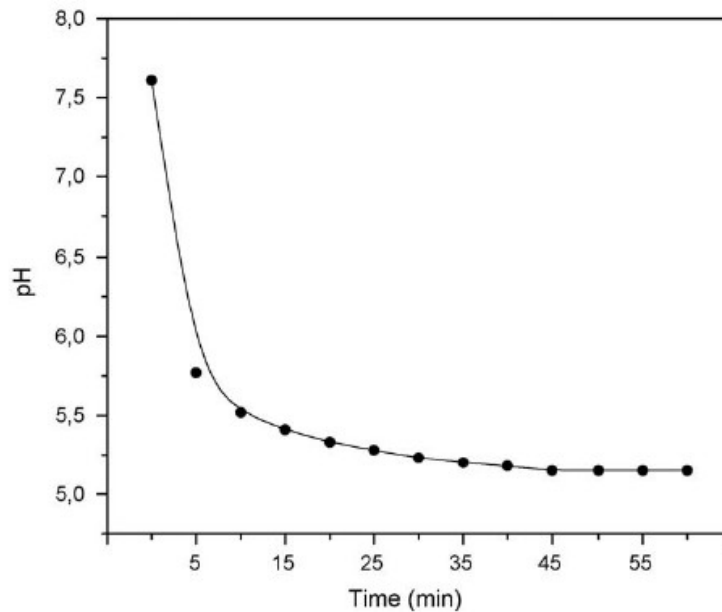
Source: Anselmo, 2006.

After acidifying the solution, carbonic acid reacts with the alloying elements, mainly with iron and, probably, iron carbonate ($FeCO_3$) is formed. According to Anselmo, when working with stainless steels in CO_2-saturated solution, there is an enrichment of the chromium concentration in the passive oxide layer associated with the increasing iron dissolution, due to the acidification promoted by the presence of CO_2 (ANSELMO *et al*, 2006). The composition of the passive layer is dependent on a synergy of the concentration of chloride in the presence of CO_2-saturated solution (ANSELMO *et al*, 2006).

Figure 56 shows the cyclic polarization curves for the samples of the 316L and AL-6XN PLUS™ steels treated at 600 °C for 960 h. After reaching the corrosion potential for the 316L steel (-0.54 V), the current density increased until -0.46 V. So the current density showed a decrease until it passivates. The current density presented low magnitude (10^{-6} mA/cm²). When the potential reached the value of +0.36 V, the passive film presented instability. This can be seen by the noise on the curve. The passive film did not resist and broke at the potential of +0.45 V (pitting potential). So the current density showed an abrupt increase indicating pit formation. The curve of the 316L steel presented hysteresis again. No matter the condition of the samples of the 316L steel, nor the pH of the solution. In all conditions, the 316L steel was susceptible to pitting corrosion.

Figure 56 - Cyclic polarization curves for the two alloys (316L and AL-6XN PLUS™) treated at 600 °C for 960 h. The solution used was TQ3219 saturated with CO2.
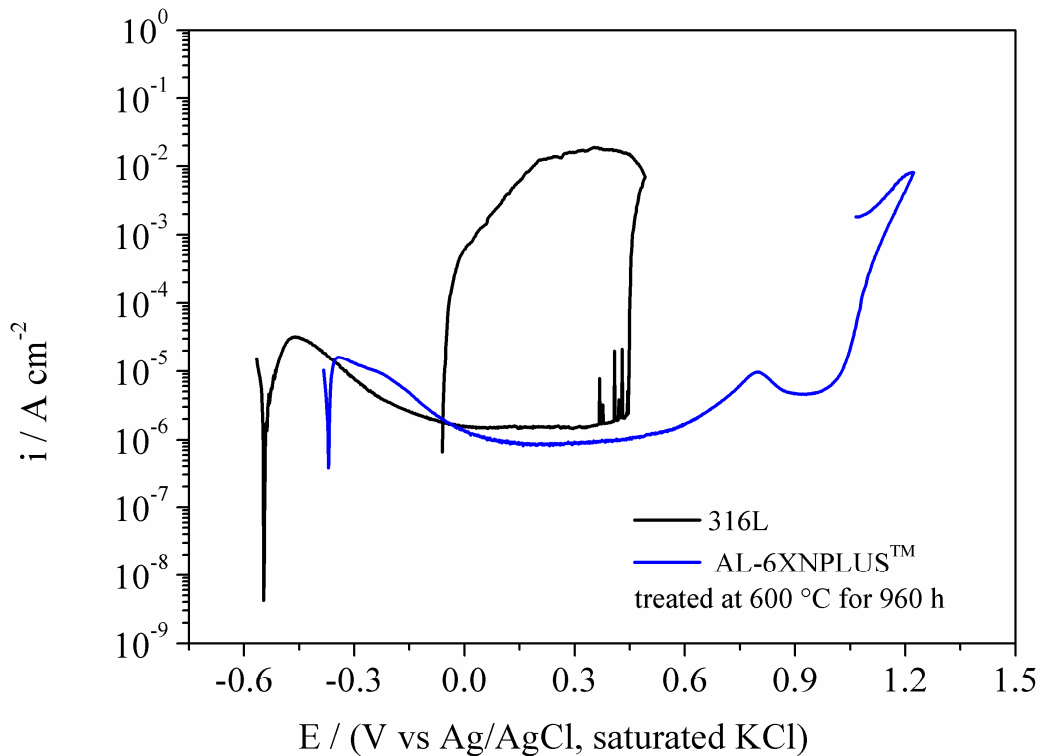
Source: the author.

The AL-6XN PLUS™ steel exhibited good corrosion resistance for this condition. After reaching the corrosion potential (-0.37 V), the alloy passivated by decreasing the current density. When reaching the potential of +0.53 V, there was an increase of the current density until the potential of +0.80 was reached. So the current density dropped down again indicating a second passivation. When the potential of +0.99 V was reached, the current density increased again. This is due to the oxygen evolution discussed before. When the current density reached the magnitude of 1.0 mA/cm², the curve returned but no hysteresis was formed. No pitting corrosion was detected for the the AL-6XN PLUS™ steel as confirmed by the SEM image of its surface.

Figure 57a shows a pit on the 316L surface. The pit shown has the same morphology as the pits of the previous experiments. Figure 57b shows the surface of the AL-6XN PLUS™ steel after the corrosion testing. No pit was found on its surface, only the risks

of sandpaper can be seen. The micrographs are in accordance with the cyclic polarization curves discussed before.

Figure 57 - SEM image of a pit on the a) 316L surface and no pits on the b) AL-6XN PLUS™ surface. The samples were treated at 600 °C for 960 h.
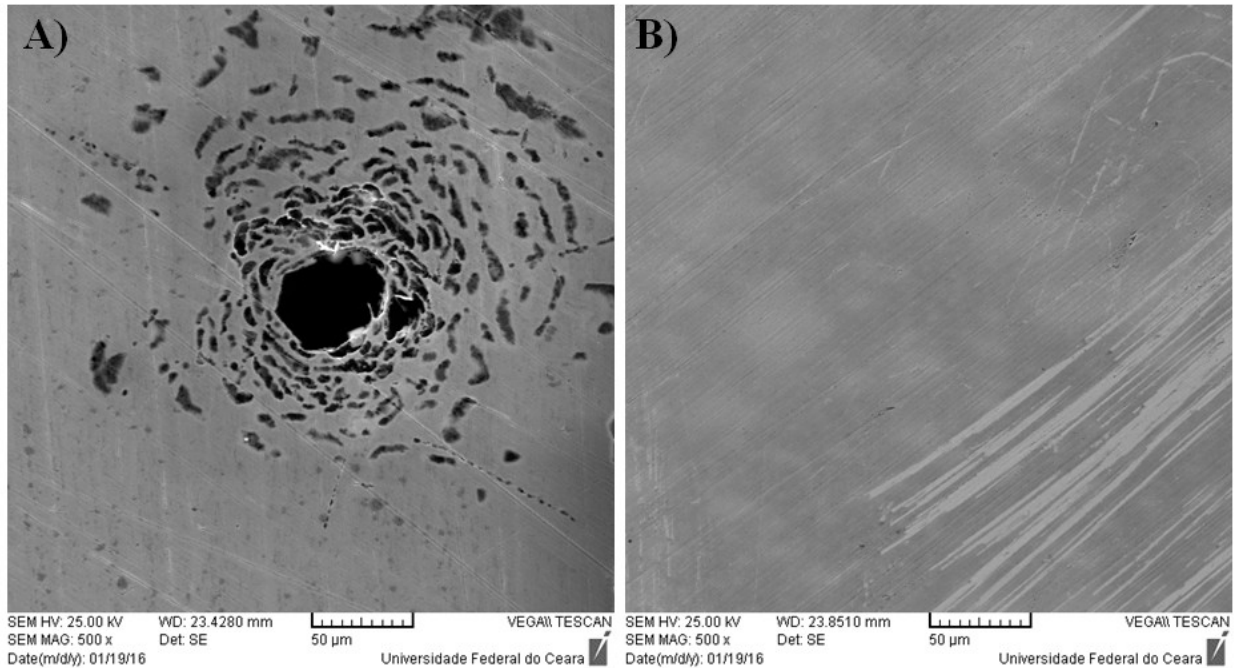
Source: the author.

The good CO_2 corrosion resistance of the super austenitic stainless steels can be attributed to the high content of alloying elements such as chromium, molybdenum and nickel. In literature, many discussion about the effect of alloying elements in austenitic stainless steels were proposed. Malik *et al* studied the relationship between pitting potential and Pitting Resistance Equivalent Number (PRE_N) of some stainless steels (austenitic, ferritic and duplex) at 50 °C in Gulf seawater under salt spray conditions and corrosion rates were determined by applying the electrochemical polarization resistance technique. Their results indicated that the presence of alloying elements such as chromium, molybdenum and nickel have a significant and beneficial influence on the pitting and crevice corrosion resistance of stainless steels (MALIK *et al*, 1995). The superaustenitic stainless steels studied in this work contain in their composition contents of chromium, molybdenum, nickel and nitrogen enough to guarantee a good performance of the passive film. This effect is confirmed with the absence of pits or another form of corrosion on the surface of these alloys.

Chromium and molybdenum are the main alloying elements in austenitic stainless steels. These elements can adhere on the passive film to inhibit localized corrosion. An oxide layer of chromium and molybdenum can form on the surface of these steels and this layer can block the action of chloride ions by inhibiting the formation or pit growth. The element molybdenum on the passive layer can also chance the electronic properties reversing the ion selectivity in the film structure hindering the migration of chloride ions through the film (WILLENBRUCH *et al*, 1990). Molybdenum gives a greater resistance to localized corrosion by forming molybidates that incorporate on the passive film to improve its structure and also reinforces the passive film by increasing its thickness (SUGIMOTO & SAWADA, 1977). According to Anselmo, the molybdenum concentration in the oxide film is also dependent on the temperature and presence of CO_2 (ANSELMO *et al*, 2006). The author also defends that chromium content in passive films increases in solution with CO_2.

6.4 Potential Step

The samples in the as received condition were submitted to another electrochemical technique called Potential Step. The investigation using this technique are in agreement with the cyclic polarization experiments where the 904L and AL-6XN PLUS™ austenitic stainless steels had excellent pitting corrosion resistance when compared with the other austenitic steels (316L and 317L). Figure 58, Figure 59, Figure 60 and Figure 61 show the results for the 316L, 317L, 904L and AL-6XN PLUS™ alloys, respectively. The graphics are of type double Y axis, where the potential (V vs Ag/AgCl, sat KCl) and the current density (mA/cm²) are plotted on the Y axis and the time (s) is plotted on the X axis. Every potential step was maintained during one hour. If nothing happened on the passive film, then a new step was reached by an increment of +50 mV. The pitting potential (E_p) of each alloy was reached when the current density reached values above 0.1 mA/cm² as shown on the graphics. So there was an abrupt increase of the current density indicating the breakdown of the passive film. The time to achieve the pitting potential depends on the film resistance of each alloy. The more resistant the passive film, more time is needed to reach the pitting potential. The pitting potential for the 316L steel presented the lowest value (+0.52 V) while the pitting potential for the 904L and AL-6XN PLUS™ steels presented the highest value (+1.06 V and +1.09 V, respectively). The pitting potential for the 317L steel presented an intermediate value (+0.81 V). Table 15 shows the pitting potential and the necessary time to achieve it for each alloy. It was necessary more than one day for the sample of the AL-6XN PLUS™ steel to reach its pitting potential. This result shows how resistant this material is. On the other hand, the 316L steel presented the lowest time to reach its pitting potential. Even without the presence of CO_2, this steel showed susceptibility to pitting corrosion in chloride containing environments. The 317L steel showed to be more resistant than the 316L steel in chloride containing environments but less resistant than the other two super austenitic steels.

Figure 58 - Plot with the potential steps, the current density and time for the 316L steel in the as-received condition.
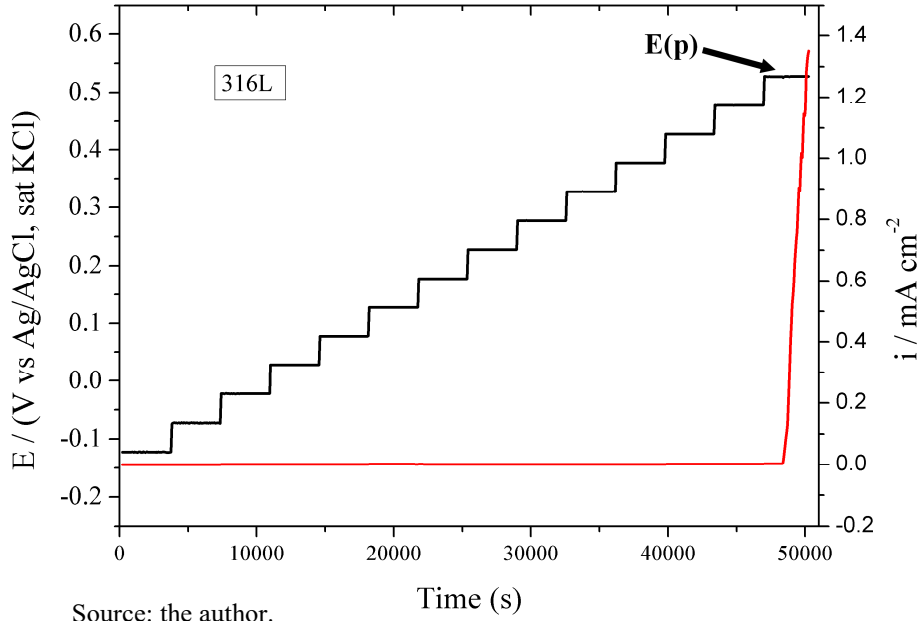
Source: the author.

Figure 59 - Plot with the potential steps, the current density and time for the 317L steel in the as-received condition.
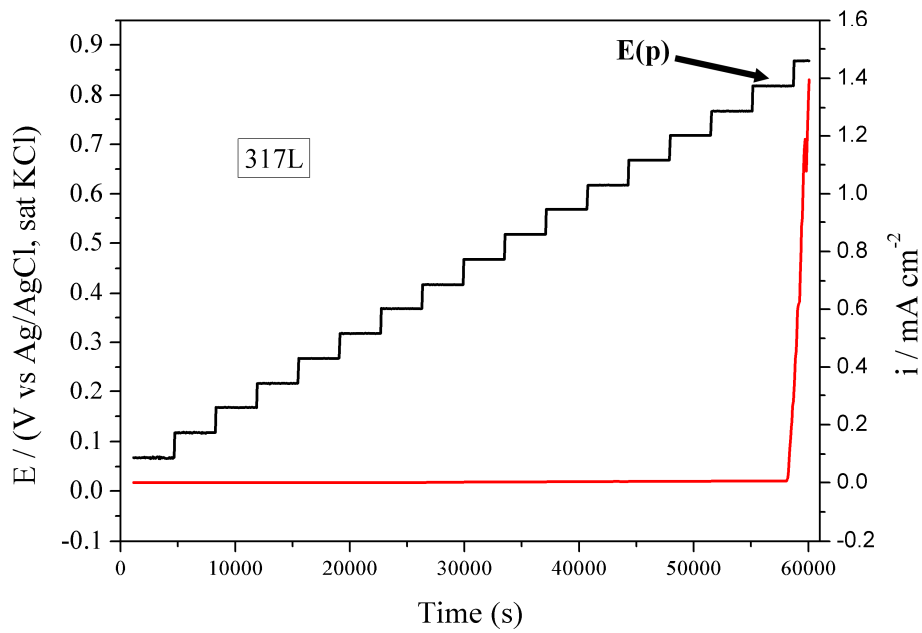
Source: the author.

Figure 60 - Plot with the potential steps, the current density and time for the 904L steel in the as-received condition.
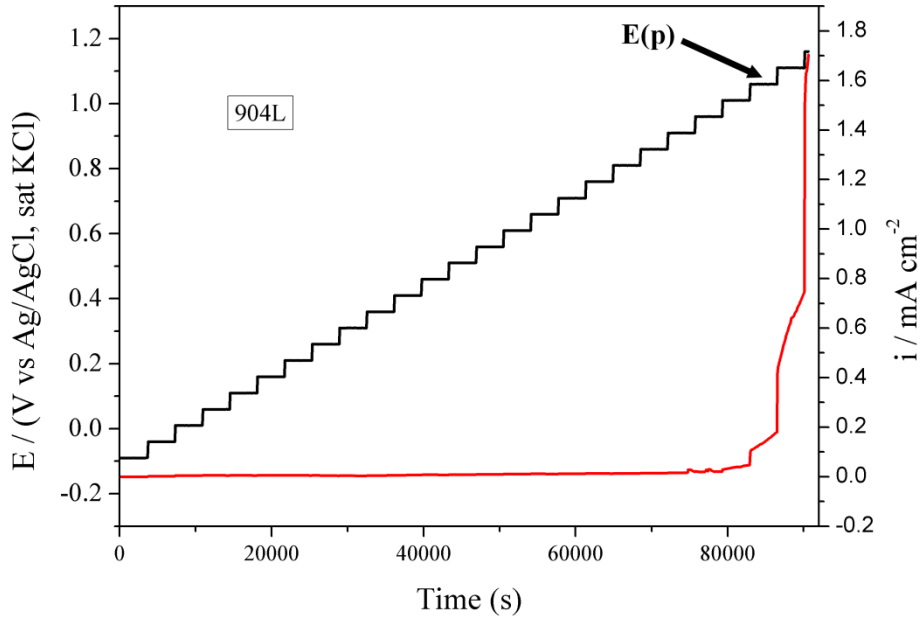
Source: the author.

Figure 61 - Plot with the potential steps, the current density and time for the AL-6XN PLUS™ steel in the as-received condition.
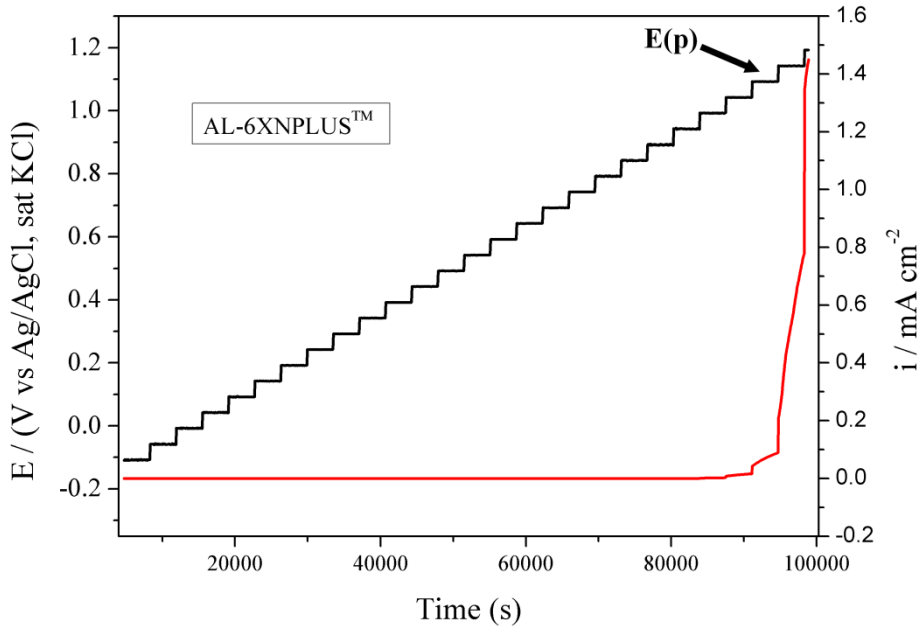
Source: the author.

Table 15 - Measured pitting potential of the studied alloys using the Potential Step technique.

| | Potential Step | |
Alloy	E(pit) (V Ag/AgCl)	time (h)
316L	+0.52	13.5
317L	+0.81	16.2
904L	+1.06	23.1
AL-6XN PLUS™	+1.09	26.2

Source: the author.

The 316L and 317L steels suffered pitting corrosion. Figure 62 shows pits on the 316L surface. The pits have circular shape with a hole in the center. The pit propagated from the center to the edge and tried to grow with time. This effect is attributed to the chloride in the solution. The chloride ion (Cl^-) is very small and can penetrate easily in sites of the 316L surface where the film is broken. A initiation of non-passivating pits starts (Figure 63a). The pits on the 316L steel grew but only in the center as show in Figure 63b. With the absence of CO_2 in the solution, the environment is not so aggressive to permit the growth of the pits.

The 317L steel also suffered pitting corrosion but its pits are so small when compared with the ones of the 316L steel. The pits initiated but they did not grow with time as shown in Figure 64. It can be seen a non uniform pit. This result indicated that the 317L steel in some chloride containing environments is also resistance being also a good choice in some applications where the 316L cannot be used, for example, in the oil and gas industry in chloride containing environments.

Figure 62 - SEM image showing the pits formation on the 316L steel.
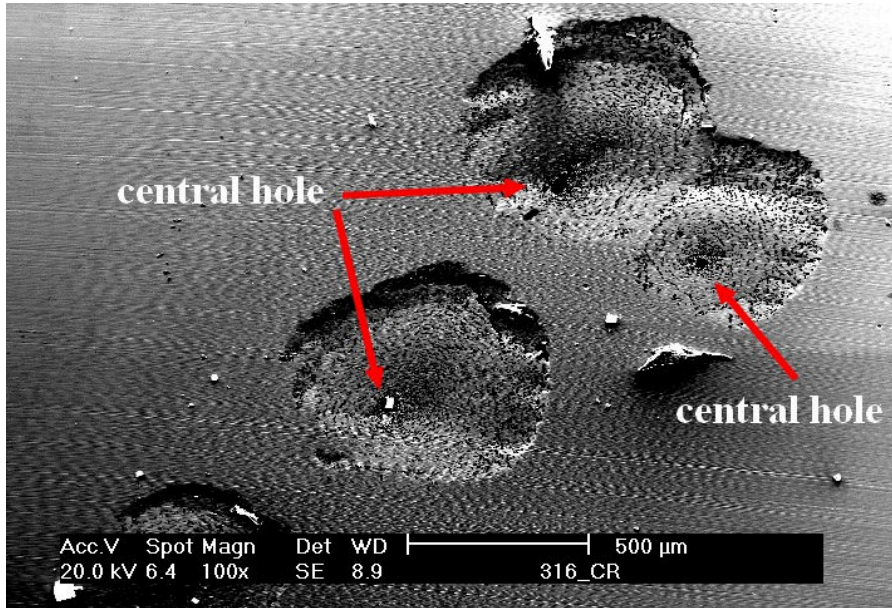
Source: the author.

Figure 63 - SEM images of the same pit on the 316L steel with different magnitudes.
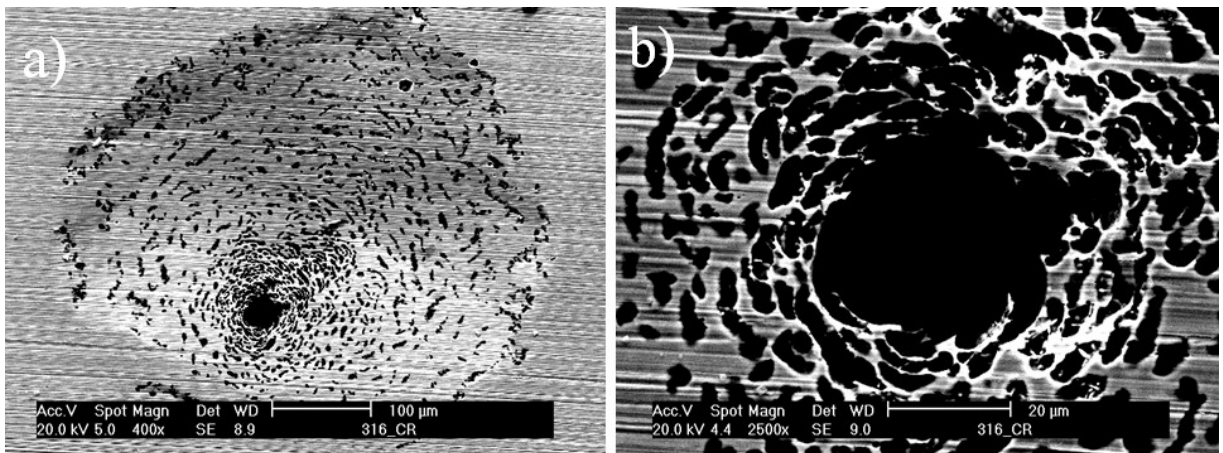
Source: the author.

Figure 64 - SEM image showing the initiating pits on the 317L steel.
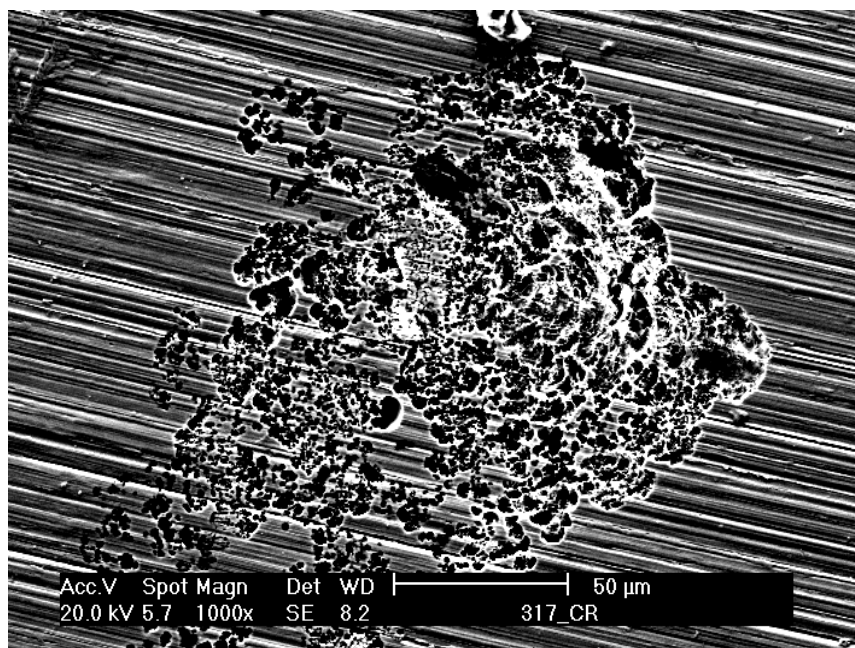
Source: the author.

The pits formed on the surface of the super austenitic stainless steels (904L and AL-6XN PLUS™) are much smaller than the ones found on the surface of conventional austenitic steels as seen in Figure 65. They are micro-pits and after initiating, they repassivate before starting to grow. All the micrographs of the alloys taken after the corrosion tests are in accordance with the graphics shown before. This experimental procedure has previously been used to qualify Ni-based alloys and hyper duplex stainless steel for raw seawater injection (EIDHAGEN & KIVISÄKK, 2012). As explained before, this good resistance is due to the Cr, Mo and Ni contents on the composition of the studied alloys relating to PRE_N of each alloy. This results in combination with the cyclic polarization tests in CO_2-saturated aqueous solution make these materials (the super austenitic stainless steels) excellent option for chloride containing environments with and without CO_2 once they are cheaper than the Ni-based alloys. In some cases, the conventional 317L steel can be also a good option than the conventional 316L steel. This time, none of the alloys suffered crevice corrosion.

Figure 65 - SEM images of micro pits on the surface of a) 904L and b) AL-6XNPLU™ steels.
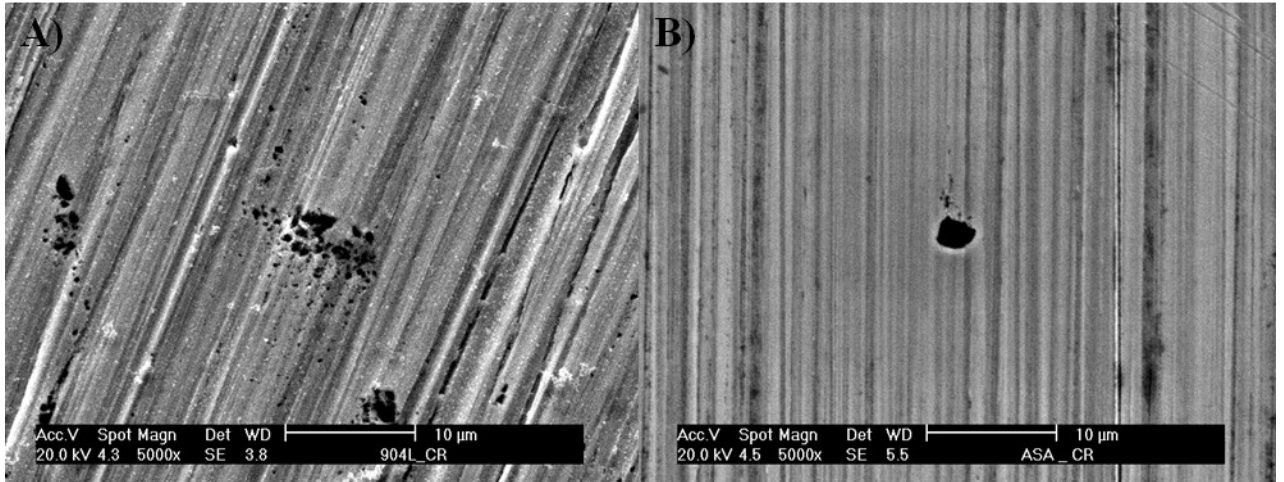
Source: the author.

6.5   Pressurized tests

The samples of the alloys were placed in an autoclave for the pressurized experiments. After the exposure tests under synthetic air pressure of 8 MPa at 80 °C during 168 h, the samples were examined by optical microscope. It was observed some rusts (indicated by white arrows) on the surface of 316L and 317L steels shown in Figure 66. The rust can be considered as the final process of the corrosion and it is located inside the region where there were droplets left on the surface of the samples. It was not found rust on the surface of the AL-6XN PLUS™ steel but some particles of salt were detected. It can be seen that the droplets of the solution act as anodic region and the sites around the droplets act as cathodic region.

Figure 66 - Optical images of rust on the surfaces of the samples of the 316L steel (a, b), 317L steel (c) and salt particles on the surface of the AL-6XN PLUS™ steel (d) after exposure test under synthetic air pressure of 8 MPa at 80 °C for 168 h sprayed with TQ3219 solution.
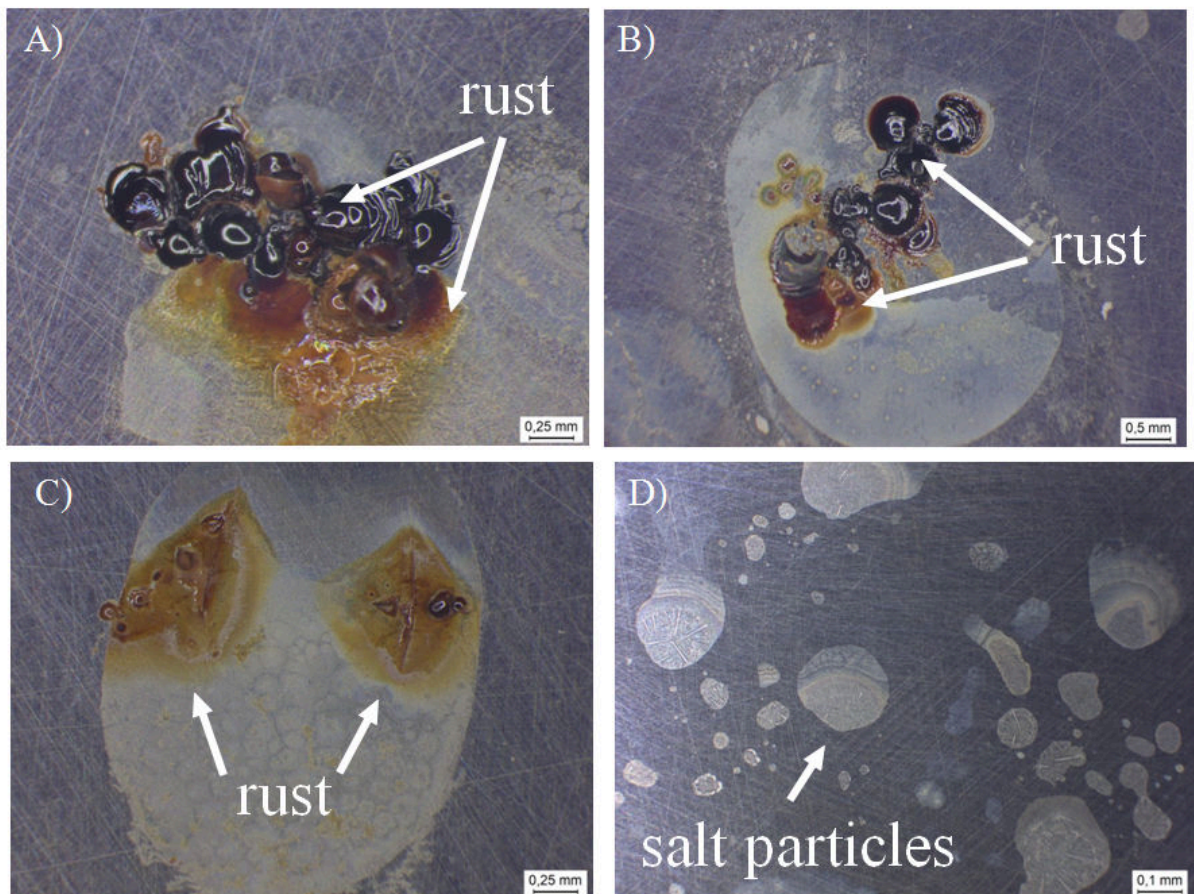
Source: the author.

Figure 67 shows the SEM on the surface of the samples after the exposure test under synthetic air pressure of 8 MPa at 80 °C for 168 h. The corrosion product (rust) was removed before the image acquisition by leaving the samples immersed in a solution of HCl 20%. The kind of corrosion on all the surfaces of the metals was identified as pitting corrosion and all the samples showed pits on their surfaces. The 316L steel was the most damaged steel when compared with the other steels. Its pits are the biggest in diameter. Here there is a combination of factors that resulted on pitting corrosion: presence of chloride, presence of oxygen, synthetic air pressure, temperature and exposure time. The synthetic air pressure acting on the surfaces of the metals compresses the solution against their surfaces enabling more effective action of chloride ions. As the samples were sprayed with the solution, there were sites on the surface with more solution (droplets) than other sites. The presence of pits was detected in sites of the surface where there were droplets of the solution. The chemical reactions that favored the pits formation occurred within these droplets.

Figure 67 - SEM images of the surfaces of the samples after removing the corrosion products. (a, b) 316L, (c) 317L and (d) AL-6XN PLUS™.
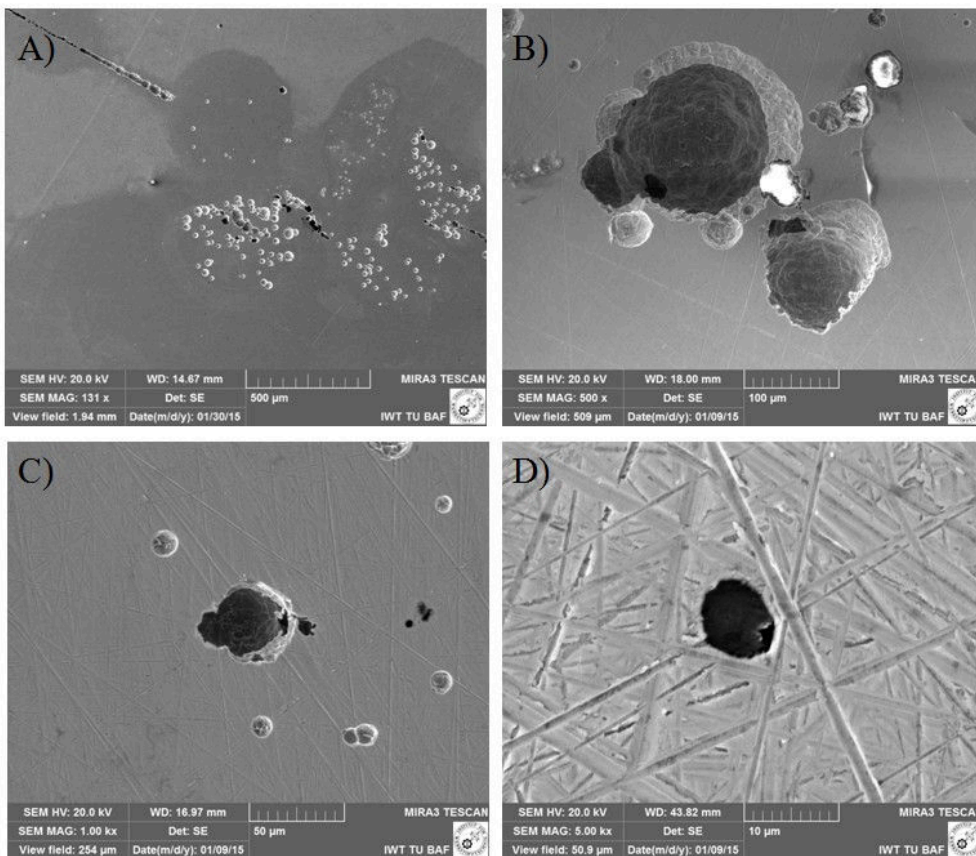
Source: the author.

The pits depth for all samples were evaluated using a Confocal White Light Interferometer. The topographies are shown in Figure 68, Figure 69 and Figure 70. The deepest pits were found on the surface of the 316L steel. This is according to SEM images. The diameters of the pits on the surface of the 316L steel are also the largest ones. The pits density shown in Figure 68 represents the place where there was a droplet. The deepest pit found on the surface of the 316L steel is 3 times deeper than the deepest pit of the 317L steel and 44 times deeper than the deepest pit of the AL-6XN PLUS™ steel. The thickness of the 316L steel is 9 times greater than its deepest pit. The 317L steel was resistant to the aggressive environment. Its pits are not so deep as the pits of the 316L steel. The AL-6XN PLUS™ steel was the most resistant material in this test. Its pits are all micro pits and this result is in accordance with the electrochemical experiments of this work.

Figure 68 - Topography of the 316L steel showing the depth and the distribution of the pits after exposure test under synthetic air pressure of 8 MPa at 80 °C for 168 h and sprayed with the TQ3219 solution.
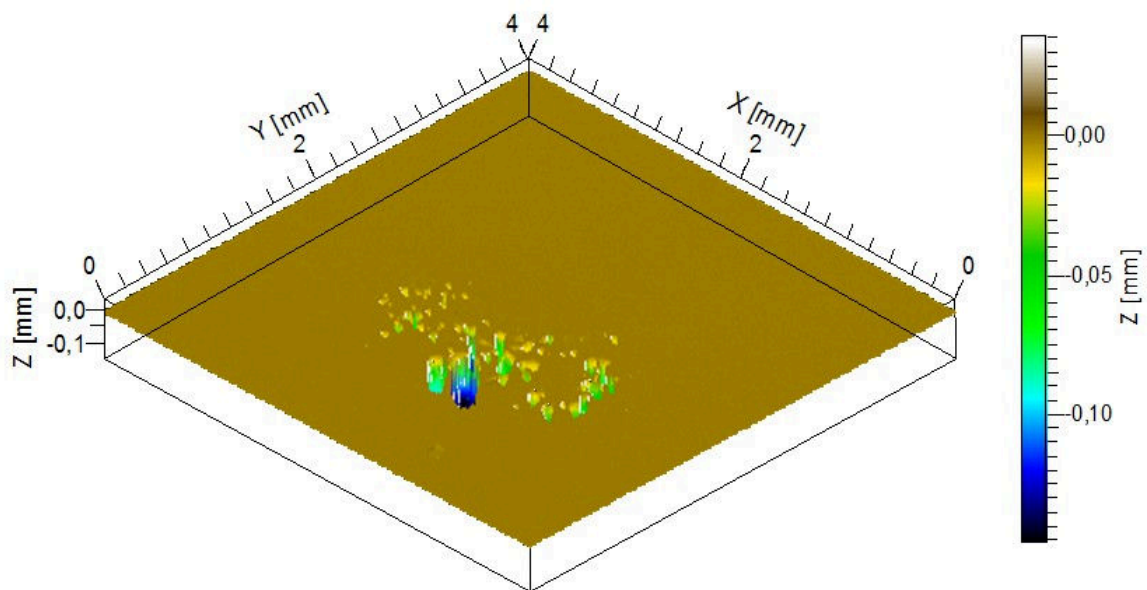
Source: the author.

Figure 69 - Topography of the 317L steel showing the depth and the distribution of the pits after exposure test under synthetic air pressure of 8 MPa at 80 °C for 168h and sprayed with the TQ3219 solution.
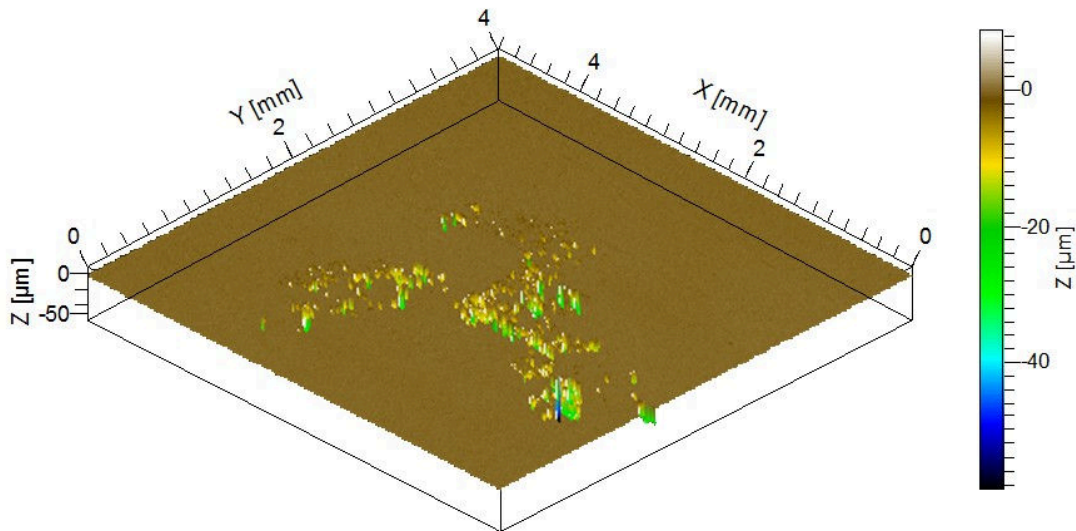
Source: the author.

Figure 70 - Topography of the AL-6XN PLUS™ steel showing the depth and the distribution of the pits after exposure test under synthetic air pressure of 8 MPa at 80 °C for 168 h and sprayed with the TQ3219 solution.
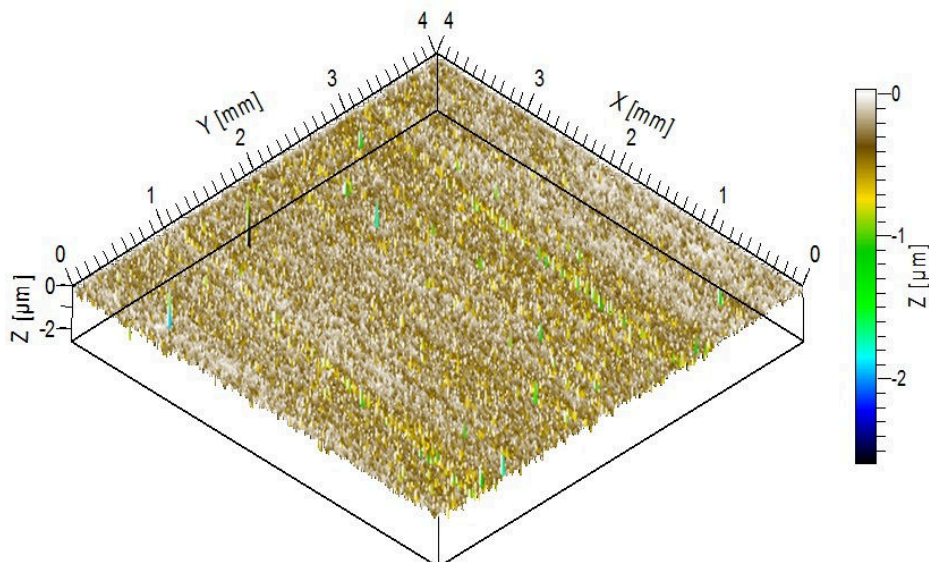
Source: the author.

All the samples were tested in another environment. This time, carbon dioxide was used under a pressure of 5 MPa. Carbon dioxide becomes a supercritical fluid when temperature and pressure exceed the critical point of CO_2 at 31.1 °C and 7.38 MPa

(DOSTAL, 2006). This is the point where there is no distinction between liquid and vapor phases as shown in Figure 71. This phase is known as super critical CO_2 (SC-CO_2). The system (autoclave, gas and samples) used in this experiment allowed a maximum carbon dioxide pressure of 5 MPa to avoid the critical point. Due to this physical problem, the carbon dioxide pressure used in this experiment was 5 MPa while the temperature and the exposure time remained the same. All the samples were sprayed again with the TQ3219 solution.

Figure 71 - Phase diagram for CO_2 showing the critical point where CO_2 becomes SC-CO_2.
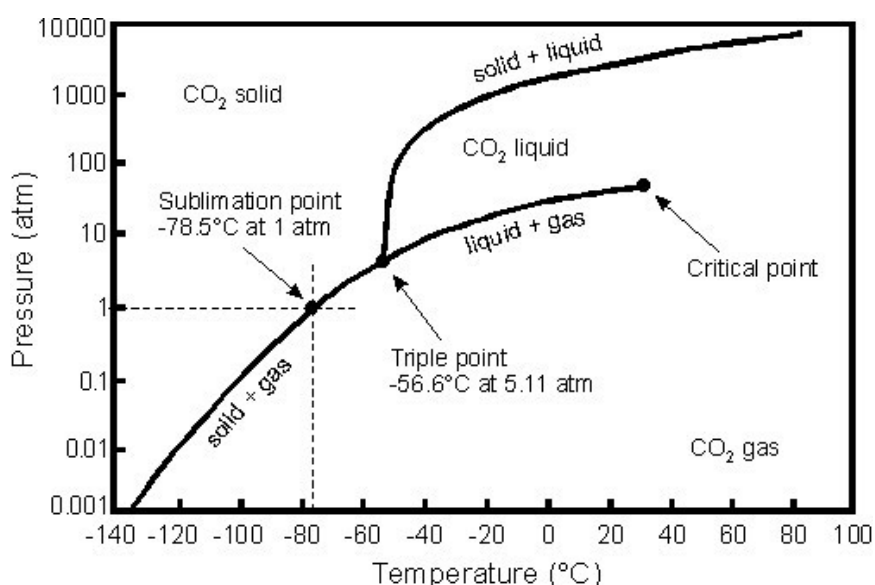
Source: Goddard, 2010.

This time, the results showed that the carbon dioxide atmosphere was not so aggressive as the synthetic air. The 316L steel was the only steel that presented significant corrosion in this medium. There was an oxide layer (rust) and salt particles on its surface (Figure 72a). The pits found were under this layer when the same was removed from the surface. The 317L also presented a little of rust and salt particles on its surface but in smaller amounts (Figure 72b). No pits were detect after removing the rust from its surface. The AL-6XN PLUS™ steel was again the most resistant alloy when CO_2 gas was used. On its surface there were only salt particles (Figure 72c) and no pitting corrosion was found again. Figure 73 shows the surface of the 316L steel after removing the rust. Pits were detected on its surface but they are not so big as the ones when synthetic air was used. Figure 74 shows the

topography of the 316L steel. The depth of the pits found on the surface of 316L steel is 0.2 times smaller than the others found when using synthetic air.

Figure 72 - Optical images of the corrosion products on the surface of the 316L (a), 317L (b) and AL-6XNPLUS™ (c) steels after exposure to CO_2 gas (5MPa at 80 °C for 168 h).
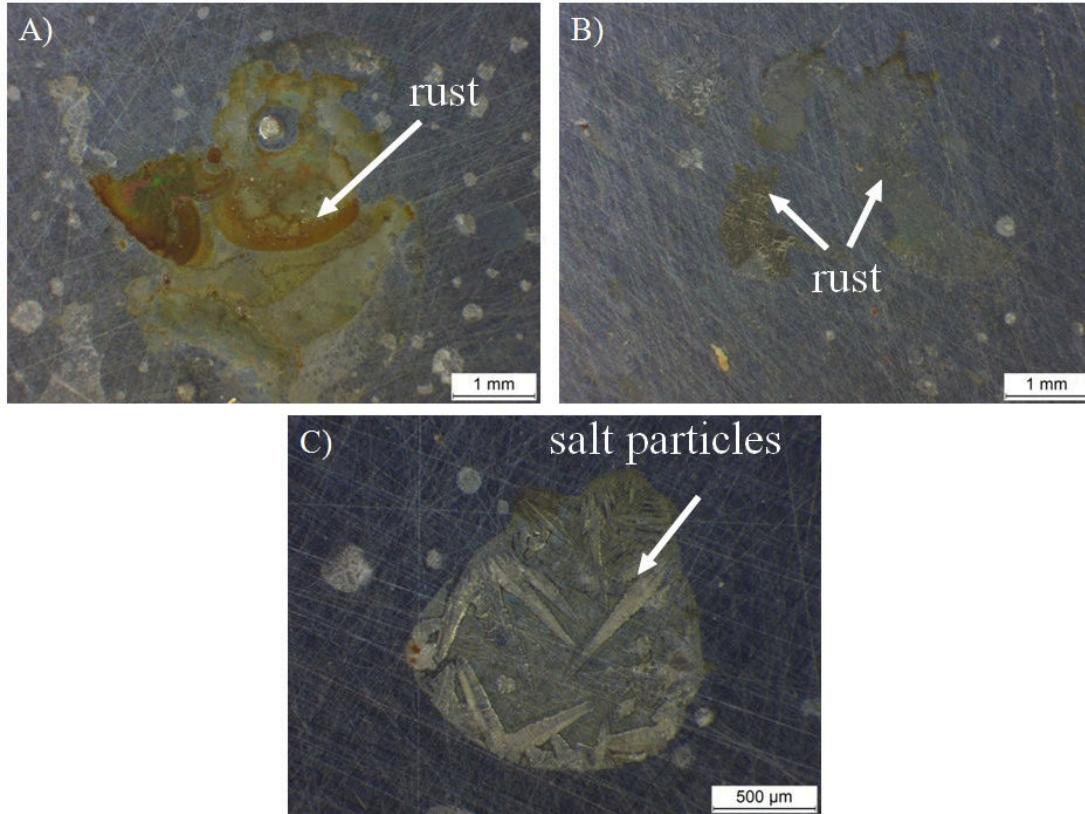
Source: the author

Figure 73 - SEM image of the surfaces of the 316L steel after exposure test under CO_2 pressure of 5 MPa at 80 °C for 168 h and sprayed with TQ3219 solution showing some pits.
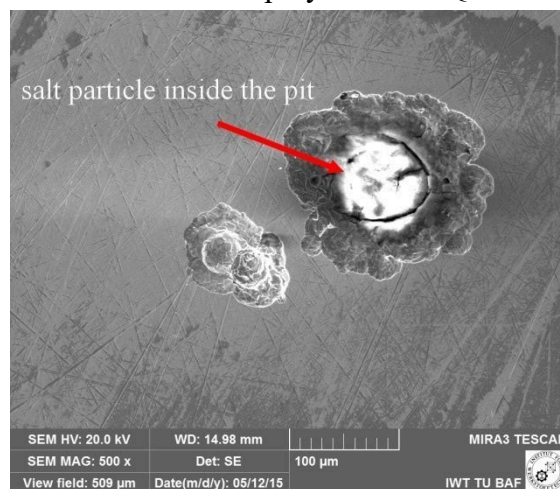
Source: the author.

Figure 74 - Topography of the 316L steel showing the depth and the distribution of the pits after exposure test under CO2 pressure of 5 MPa at 80 °C for 168 h and sprayed with TQ3219 solution.
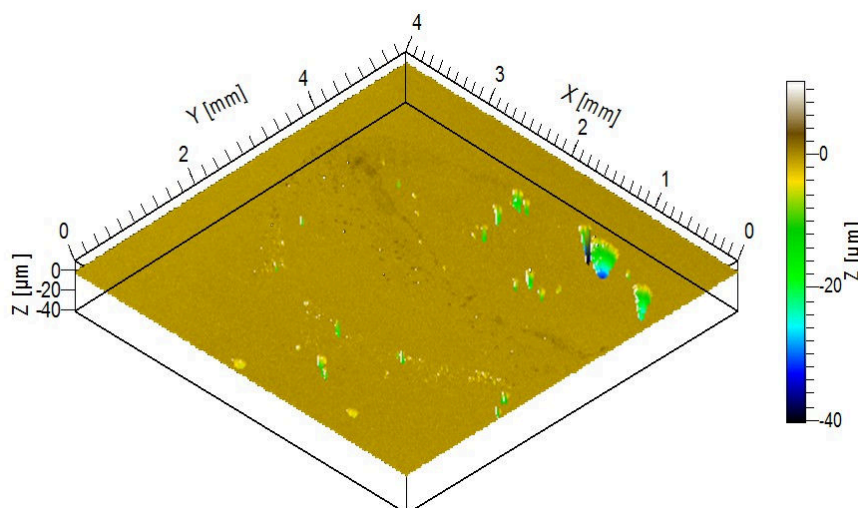
Source: the author.

All the samples were tested again but this time in an environment by mixing the two gases used before. This time, carbon dioxide gas and synthetic air were mixed to create another atmosphere. The combination of this new atmosphere was 5 MPa of carbon dioxide (62.5 %) and 3 MPa of synthetic air (37.5 %) reaching a total pressure of 8 MPa. The samples were sprayed again with the same solution (TQ3219). The temperature and exposure time remained the same. Figure 75 shows the micrographs of the surface of the 316L and 317L steels after exposure test. In Figure 75a for the 316L steel it can be seen the droplet boundary and inside the droplet several pits and near the pits salt particles. Figure 75b shows the shape of the pits for the 316L steel. Some of them are circular and the trend is to form bigger pits. The pits in Figure 75b are surrounded by salt particles left inside the droplet. An overview of the surface of the 317L steel can be seen in Figure 75c. Droplet boundaries can be seen and inside them some pits. A single pit can be seen in Figure 75d. This pit is neither big nor deep. The two conventional austenitic stainless steels (316L and 317L) suffered pitting corrosion but the 317L steel was more resistant to pitting corrosion than the 316L steel for the same conditions. The combination of the two gases and the solution (represented by the droplets) created the conditions to cause pitting corrosion on these steels.

Figure 75 - SEM images of the surfaces of the 316L (a, b) and 317L (c, d) steels after exposure test under the combination of CO_2 and synthetic air pressure (5 MPa and 3 MPa, respectively) at 80 °C for 168 h and sprayed with TQ3219 solution.

A)

SEM HV: 20.0 kV WD: 18.26 mm MIRA3 TESCAN
SEM MAG: 30 x Det: SE 2 mm
View field: 8.48 mm Date(m/d/y): 05/29/15 IWT TU BAF

B)

SEM HV: 20.0 kV WD: 18.37 mm MIRA3 TESCAN
SEM MAG: 150 x Det: SE 500 µm
View field: 1.70 mm Date(m/d/y): 05/29/15 IWT TU BAF

C)

SEM HV: 20.0 kV WD: 17.23 mm MIRA3 TESCAN
SEM MAG: 150 x Det: SE 500 µm
View field: 1.70 mm Date(m/d/y): 05/29/15 IWT TU BAF

D)

SEM HV: 20.0 kV WD: 17.19 mm MIRA3 TESCAN
SEM MAG: 1.00 kx Det: SE 50 µm
View field: 254 µm Date(m/d/y): 05/29/15 IWT TU BAF
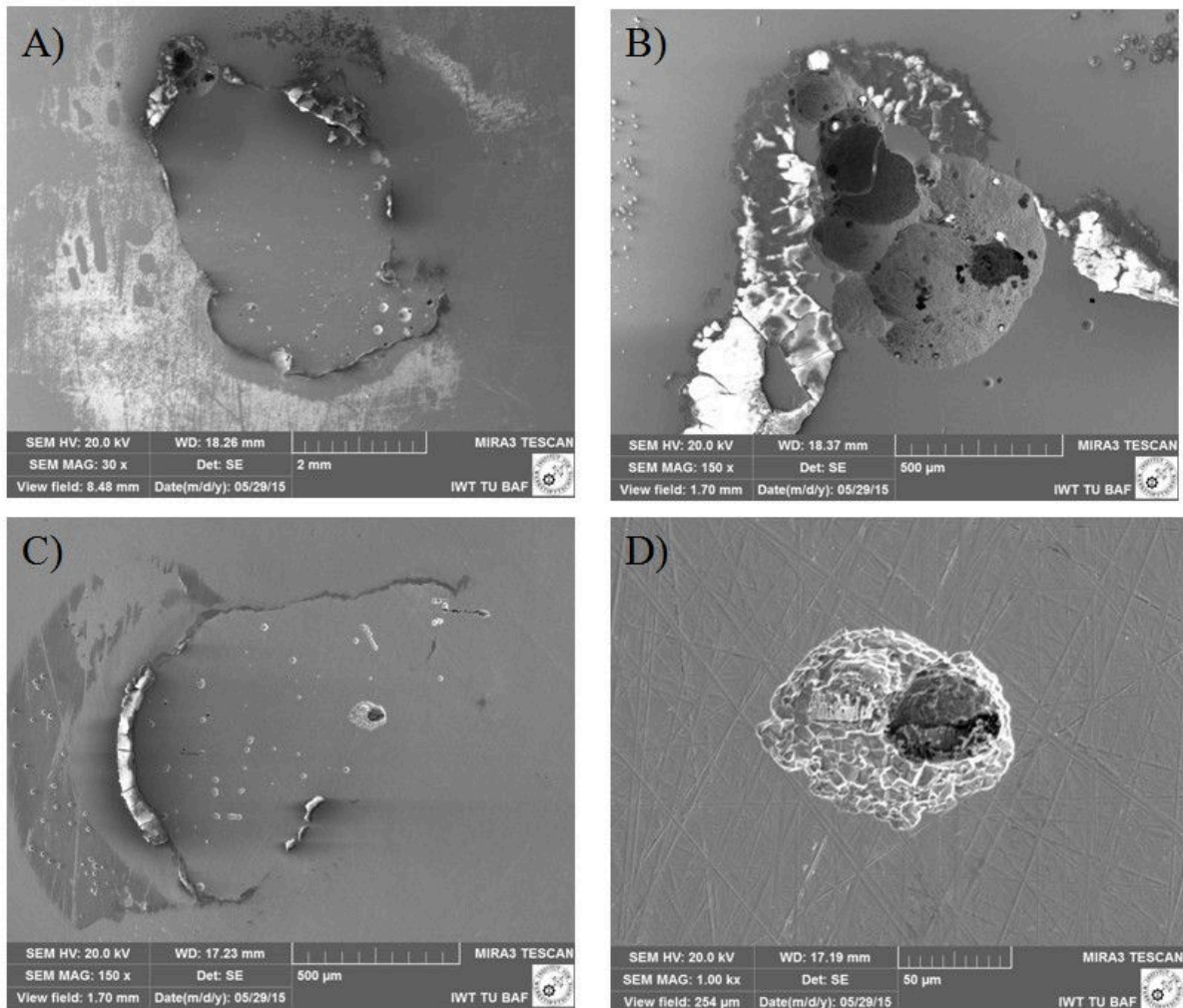
Source: the author.

No pits were detected on the surface of the AL-6XN PLUS™ steel as can be seen in Figure 76. Super austenitic stainless steels are very resistant to pitting corrosion, CO2 corrosion, crevice corrosion. This good resistance is attributed to the alloying elements present in its composition, manly chromium, molybdenum and nickel. The 904L was not tested in the pressurized experiments but it is believed that this steel would present a similar performance like the performance of the AL-6XN PLUS™ steel, once the composition of this alloy is similar to the composition of the AL-6XN PLUS™ steel. These results confirm the good performance that this class of steel showed in the electrochemical tests used in this work.

In all the experiments, the AL-6XN PLUS™ superaustenitic stainless steel showed a good corrosion resistance. The 316L steel presented the lowest corrosion resistance in all experiments. It was detected pits on its surface in all tests. The 317L steel also presented a good resistance but not so good as the resistance of AL-6XN PLUS™ steel.

Figure 76 - SEM images of the surfaces of the AL-6XN PLUS™ steel after exposure test under the combination of CO2 and synthetic air pressure (5 MPa and 3 MPa, respectively) at 80 °C for 168 h and sprayed with TQ3219 solution.

SEM HV: 20.0 kV	WD: 14.51 mm		MIRA3 TESCAN
SEM MAG: 200 x	Det: SE	200 µm	
View field: 1.27 mm	Date(m/d/y): 05/29/15		IWT TU BAF
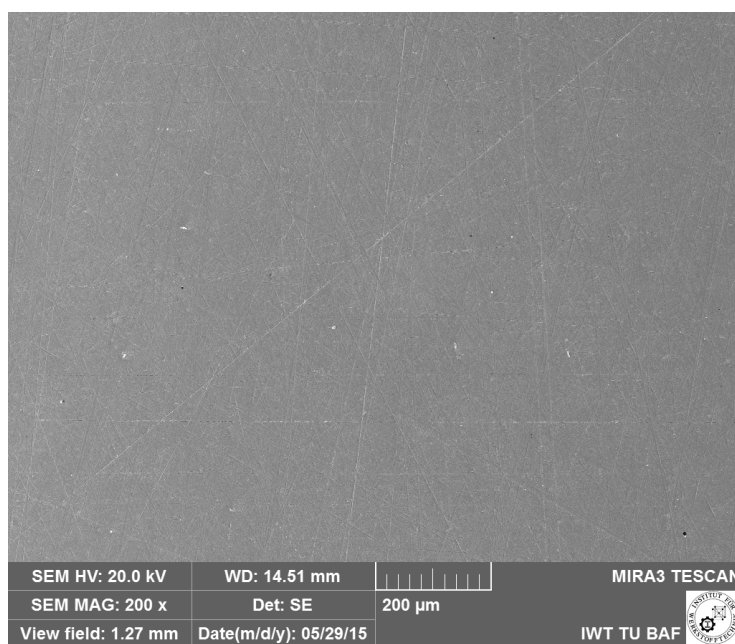
Source: the author.

Figure 77 and Figure 78 show the topography only for the samples with pits on their surfaces. It can be seen that the pits density is greater for the 316L than for the 317L. On the topography of the 316L steel, it is also possible to see the droplet boundary and all the pits inside it confirming what was observed in the SEM micrographs. Outside of the droplet no pit was detected. The same particularity can be seen on the topography of the 317L. The pits of the 316L steel are deeper when comparing with the pits of the 317L steel. It is believed that for higher pressures and higher temperatures for larger exposure times, these pits would be bigger in diameter and also in depth for both conventional alloys (316L and 317L). For more severe conditions, the pits on the 316L could even exceed the thickness of the alloy in long-term service if this alloy was used in CO_2 containing environment in the oil and gas industry in severe conditions.

Figure 77 - Topography of the 316L steel after exposure test under the combination of CO_2 and synthetic air pressures (5 MPa and 3 MPa, respectively) at 80 °C for 168 h and sprayed with TQ3219 solution showing the depth and the distribution of the pits.
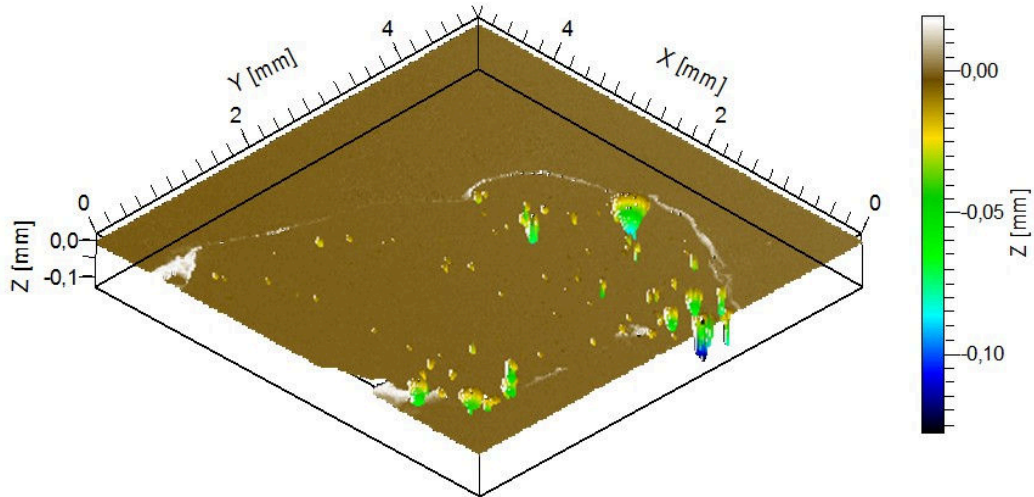
Source: the author.

Figure 78 - Topography of the 317L steel after exposure test under the combination of CO_2 and synthetic air pressures (5 MPa and 3 MPa, respectively) at 80 °C for 168 h and sprayed with TQ3219 solution showing the depth and the distribution of the pits.
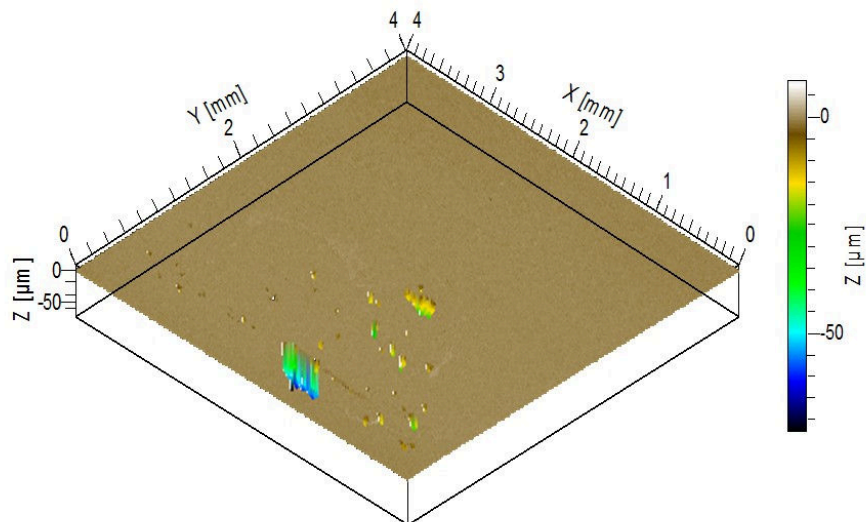
Source: the author.

Choi *et al* studied the effect of impurities on CO_2 corrosion of carbon steel and a 13Cr steel in CO_2-saturated medium to simulate the condition of CO_2 transmission pipeline in the carbon capture and storage (CCS) applications (CHOI *et al*, 2010). The authors studied

the influence of some impurities (O_2 and SO_2) in the solution along with dissolved CO_2. They concluded that the corrosion rate is low when only CO_2 is used in the solution. The addition of O_2/0.33 MPa and SO_2/0.08 MPa in the system dramatically increases the corrosion rates as seen in Figure 79 for the carbon steel. The authors also state that no corrosion was observed in dry conditions. This results are consistent with the results of this work. Outside the droplets (dry condition), no corrosion for all alloys was not observed. The increase of the corrosion effect by adding synthetic air in the system is also consistent with the results of Choi *et al*.

Figure 79 - Effect of impurities (O_2 and SO_2) on the corrosion rates of carbon steel in CO_2 containing environment.
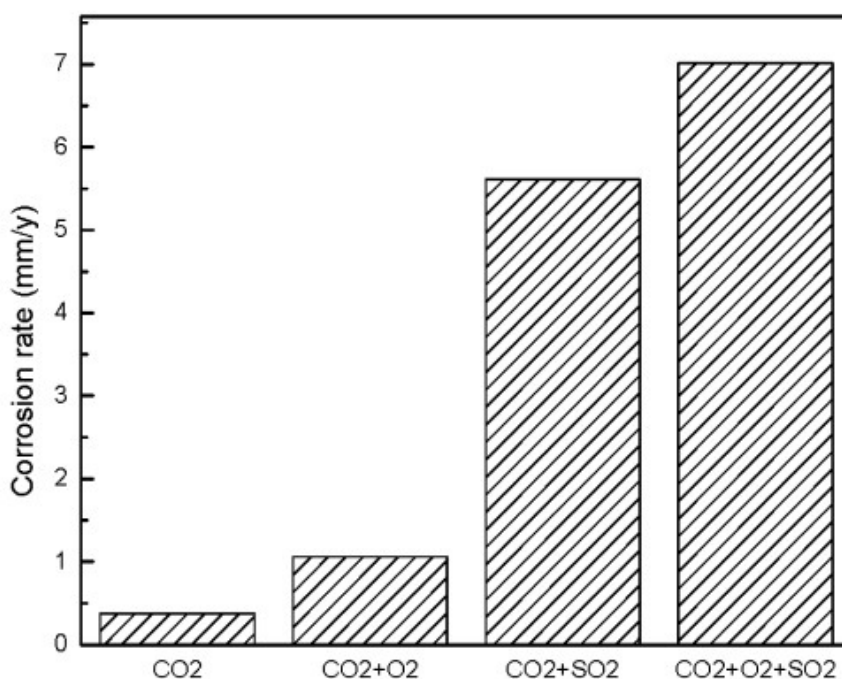
Source: Choi *et al*, 2010

Regarding corrosion, water plays an important role as electrolyte by dissolving gases providing several of the cathodic reactions for corrosion to occur. All the chemical reactions occurred inside the droplets. The chloride ions of the TQ3219 solution in the droplets reacted with the surface of the metal breaking the passive layer causing pits. Austenitic stainless steels are iron based alloys and equation 8 presents a possible anodic reaction inside the pit after the breakdown of the passive layer for iron based alloys (LOTO, 2013).

Inside the pit occurs the following anodic reaction (dissolution of iron)

$$Fe(s) \leftrightarrow Fe^{2+}(aq) + 2e^- \qquad (8)$$
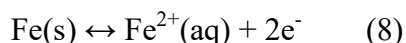
In the cathodic reaction, electrons flow to the cathode to be discharged. This occurs on the passive layer according to equation 9 (CHARNG, 1982).

$$\frac{1}{2} O_2 + H_2O + 2e^- \leftrightarrow 2(OH^-) \qquad (eq.\ 9)$$
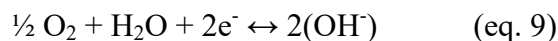
As a result of these reactions, the charge inside the pit is positive and the charge surrounding the pit is negative. The positive charge into the pit (Fe^{2+}) attracts the negative ions of chloride (Cl^-) and this increases the chloride activity into the pit according to equation 10 (CHARNG, 1982).

$$FeCl_2 + 2H_2O \leftrightarrow Fe(OH)_2 + 2HCl \qquad (eq.\ 10)$$
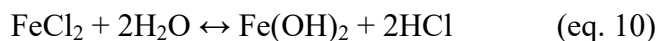
Due to the formation of HCl, the pH inside the pit decreases which causes further acceleration of pitting corrosion. This acid can also reacts with Cr forming $CrCl_2$ according to equation 11:

$$Cr + 2HCl \rightarrow CrCl_2 + H_2 \qquad (eq.\ 11)$$
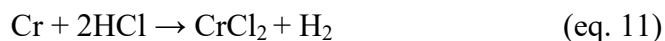
Schematic drawings were made to depict the mechanism of the pitting corrosion for the pressurized tests (Figure 80, Figure 81 and Figure 83). Figure 80 depicts the pitting initiation inside the droplet. Sodium chloride is separated in two ions. The negative ion (Cl^-) breaks the passive film. This penetration mechanism involves the migration of aggressive Cl^- ions from the solution through the passive layer under the influence of pressure and temperature. The breakdown of the passive film starts when cracks appear in the passive film under induced corrosion activity. This is enough to expose small areas on the surface of the metal to the solution. The cations from the metal are transferred from the passive film to the solution due to chromium depletion. This leads to the dissolution of the metal causing the thinning and final removal of the passive layer. The pits initially grow in the metastable condition (LOTO, 2013).

Figure 80 - Schematic drawing of the mechanism of pitting initiation on the surface of stainless steels.
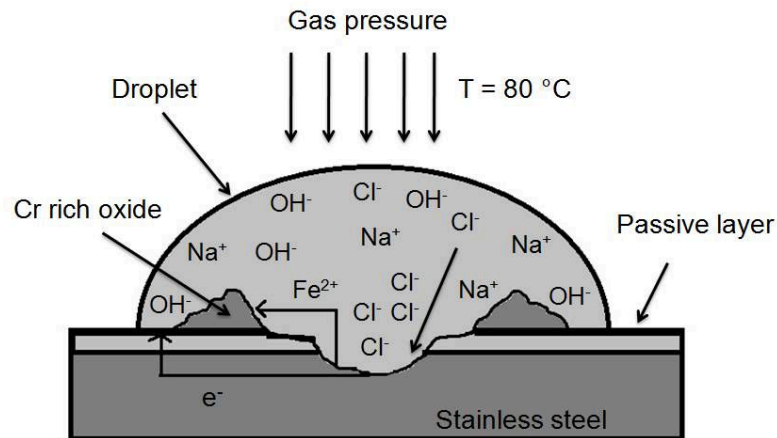
Source: the author. (adapted from Schubert, 2014).

Figure 81 depicts the next stage of pit growth on the surface of the metal. The pit becomes deeper with time while the droplet dries. A corrosion product (rust) forms on the surface of the metal and becomes more thicker with time. The rust on the surface of the samples was identified by XRD ($Cu_{K\alpha}$ = 0.15406 nm) as a chromium rich oxide as shown in Figure 82. The oxide layer is primarily composed by $Cr_{1.3}Fe_{0.7}O_3$ or Cr_2O_3 and $FeCr_2O_4$. According to Rothman *et al*, this is typical for Fe-Cr-Ni stainless steels due to the greater diffusion coefficients of chromium and iron (ROTHMAN, 1980). According to equation 10, inside the pit there is a formation of HCl leaving the pH acidic within the pit. This accelerates the corrosion process in the bottom of the pit.

Figure 81 - Schematic drawing for the mechanism of pit growth and the increase of Cr oxide layer.
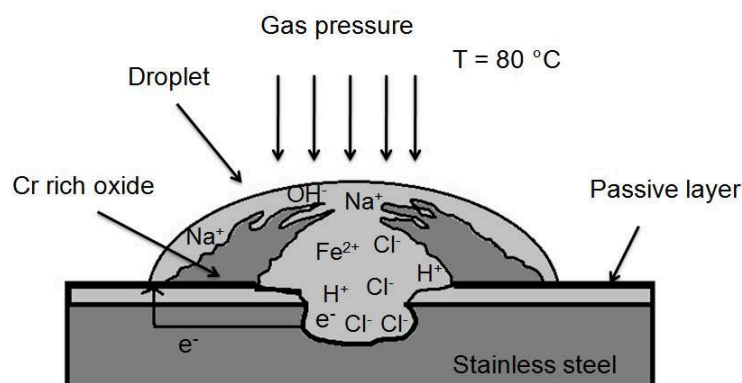
Source: the author. (adapted from Schubert, 2014).

Figure 82 - A comparison between the XRD patterns of the corrosion product of the 316L and 317L alloys after exposure tests to CO_2 and synthetic air.
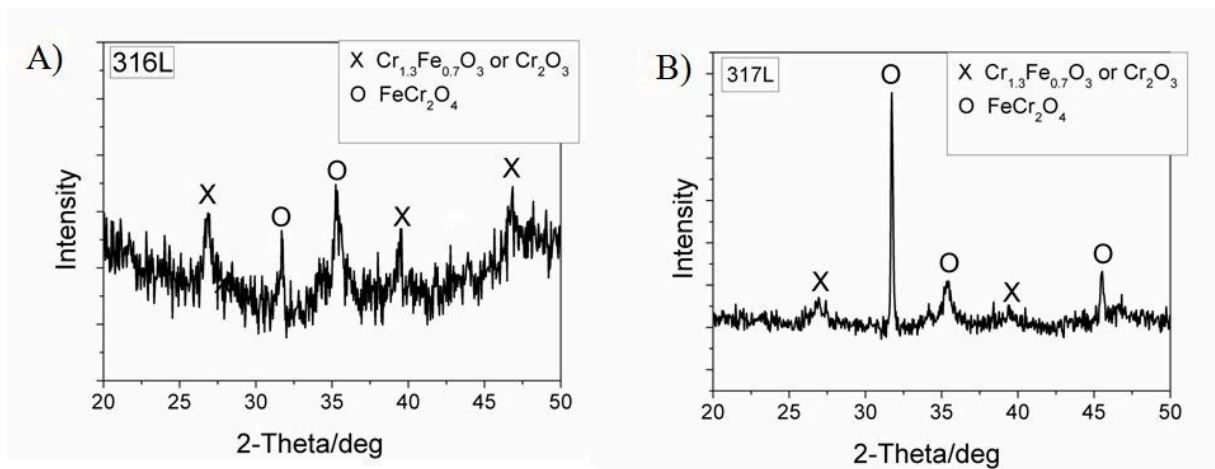
Source: the author.

Figure 83 depicts the last stage of the growing pit on the surface of the metal. The Cr-oxide layer is covering all the pit isolating the pit from the environment. The pit is stabilized. The Cr-oxide layer can be a protective layer or not. The droplet is nearly dry reducing the moisture and the possibility for new pits to grow. Only the pressure and temperature would not be enough to cause this kind of corrosion on the surface of the samples. An aqueous medium is necessary and it seems to be the driving force for corrosion to occur.

Figure 83 - Schematic drawing for the last stage of pit growth during pressurized tests.
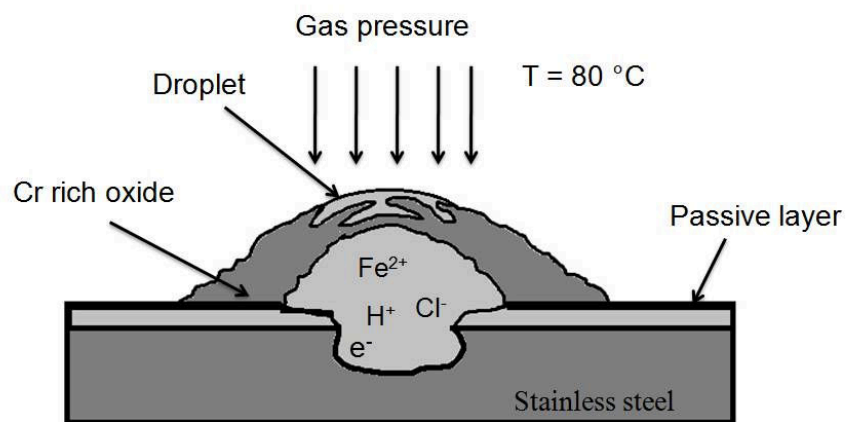
Source: the author. (adapted from Schubert, 2014)

Table 16 summarizes the results for pressurized tests. It can be seen the depths of the deepest pits found on each sample. For the 316L steel, the most aggressive atmospheres were caused by synthetic air and the combination of synthetic air plus carbon dioxide. For the 317L and AL-6XN PLUS™ steels, the most aggressive atmosphere was caused only by synthetic air. This result can be attributed to the oxygen presented in the atmosphere created for the experiment. This element has a great electron affinity to form hydroxyl (OH^-).

Table 16 - The depth of the deepest pits in all tests.

Alloy	deepest pit of the alloys (mm)		
	Synthetic air	CO_2	Synthetic air + CO_2
316L	0.2010	0.040	0.200
317L	0.0640	-	0.026
AL-6XN PLUS^{TM}	0.0045	-	-

Source: the author.

Table 17 shows the estimated time of useful life for each alloy in the first experiment when only synthetic air was used. The estimated time was calculated considering a thickness of 1.9 mm for each alloy. This was the thickness of the 316L steel used in the pressurized experiments. The estimated time took into account that the deepest pit was reached in seven days, approximately. In this case, if the pit growth was not interrupted in the first pressurized experiment using synthetic air.

Table 17 - Estimated time of useful life for each alloy in the 1st experiment (synthetic air 8 MPa at 80 °C).

Alloy	Thickness (mm)	Deepest pit (mm) reached in 7 days	Estimated time for the pit to reach the sample thickness (days)
316L	1.9	0.2010	66.7
317L	1.9	0.0640	207.8
AL-6XN PLUS™	1.9	0.0045	2955.5

Source: the author.

For the estimated time shown in Table 17, the 316L steel would fail in 66.7 days (two months and 6 days, approximately). The 317L steel would fail in 207.8 days (nearly seven months) as the AL-6XN PLUS™ steel would fail in 2955.5 days (eight years approximately). Super austenitic stainless steels are the best choice to be used in applications where there are aggressive environments when gases such as CO_2, O_2, SO_2, H_2S are present. The CPT for this type of steel is higher than the temperature used in the pressurized experiments of this work. Table 18 shows the CPT of the studied alloy (in the as received condition) that were used in the pressurized experiments. The values were taken from the literatures. The CPT was not reached for the AL-6XN PLUS™ but it was estimated by Evaristo Reis to be above 93 °C (Reis, 2015). The temperature used in the pressurized experiments of this work was 80 °C and it is higher than the CPT for the 316L and 317L steels.

Table 18 - CPT for the studied alloys used in the pressurized experiments (ASTM G 150-13).

Alloy	CPT (°C)	Reference
316L	12-15	Liu *et al*, 2015
317L	33 ± 3	Outokumpo (ultra 317L)
AL-6XN PLUS™	> 93	Reis, 2015

Source: the author.

In all experiments of this work, the 904L and AL-6XN PLUS™ super austenitic stainless steels presented a good performance indicating that this class of material is more suitable for the use in severe environments, mainly in CO_2 containing environments than the conventional 316L and 317L austenitic stainless steels.

7   CONCLUSIONS

The conventional 316L and 317L austenitic stainless steels presented susceptibility to pitting and crevice corrosion in CO_2-containing environment. The 316L steel presented pits on its surface in all experiments. The 317L steel was more resistant to pitting corrosion but susceptible to crevice corrosion.

The AL-6XN PLUS™ and 904L super austenitic stainless steels presented a good performance in CO_2-containing environment. In the cyclic polarization tests, they did not present pits on their surface. In the Potential Step, micro pits were detected on their surface but they are too small to be considered as a damage on their surface.

The pH of the solution shifted the pitting potential of the 316L steel to lower values. This effect was caused by the presence of CO_2 dissolved in the solution. When CO_2 gas was bubbled in the solution, the pH shifted from basic to acid leaving the environment more aggressive.

The pressurized experiments using CO_2 gas and synthetic air showed that the effect of pressure on the surface of the samples were not so harmful. Only when impurities were presented on the surface of the alloys the effect of pressure can be considered.

Dry CO_2 caused no damage on the surface of the studied alloys. All the pits formed on the alloys were found inside the droplets showing that the effect of CO_2 or synthetic air pressure or the combination of both gases is considered only when these gases reacted with an aqueous medium.

The presence of chloride in the solution combined with the pressure of both gases at 80 °C was the driving force to cause pitting corrosion on the studied alloys. The 316L steel was the most damage one. Several pits were observed on its surface after the pressurized experiments. The 317L steel was more resistant than the 316L steel in the pressurized experiments. The pits found on its surface were shallow and the pit density inside the droplets was lower than that for the 316L steel. The AL-6XN PLUS™ steel was the most resistant material in all experiments. When using only synthetic air pressure, the pits detected on its surface were very small. No pit was detected on its surface for the other pressurized experiments.

The 904L steel was not tested in the pressurized experiments but it is believed that its performance tends to be similar when compared with the performance of the AL-6XN PLUS™ steel. Both of them are super austenitic stainless steels and the content of alloying elements such as Cr, Mo and Ni is high for these steels to create a barrier against localized corrosion enabling a good corrosion resistance even in CO_2-containing environment.

Sigma phase was not detected for the heat treated alloys at high temperatures (600 °C - 760 °C) even after a long exposure time of 960 h. This proves that the precipitation kinetics of sigma phase in austenitic steels is very slow making advantageous the use of these alloys in applications involving high temperatures when the operating time is not so long.

The peaks of ferrite on the diffractogram pattern of the 316L and AL-6XNPLUS™ steels can be an indication that the sigma phase precipitates by an eutectoid reaction as defended by some authors. The temperatures used for the heat treatments are in accordance with the temperatures used by some authors who found sigma phase after a long time of exposure of the samples in the heat treatments. The time of the heat treatments used in this research was not enough to allow sigma precipitation and this is in accordance with literature when it is stated that sigma precipitation in austenitic stainless steels takes long time.

The electrolytic etching and the EDS and EBSD measurements showed no sigma precipitation on the heat treated samples confirming the absence of peaks of sigma phase on the diffractogram pattern of the samples.

The results of this work showed that in aggressive environments mainly in CO_2-containing environment, the best choice is to use corrosion resistant alloys such as super austenitic stainless steel than the conventional ones. The metallurgical improvements of this type of steel showed to be an important feature when selecting materials for this purpose.

8 REFERENCES

ANSELMO, N., MAY, J. E., MARIANO, N. A., NASCENTE, P. A. P., & KURI, S. E. Corrosion behavior of supermartensitic stainless steel in aerated and CO_2-saturated synthetic seawater. Materials Science and Engineering: A, v. 428, n. 1, p. 73-79, 2006.

AL-HASSAN, S., MISHRA, B., OLSON, D. L., & SALAMA, M. M. Effect of microstructure on corrosion of steels in aqueous solutions containing carbon dioxide. Corrosion, v. 54, n. 6, p. 480-491, 1998.

ALLEGHENY-LUNDLUM. AL-6XN PLUS™ Alloy Technical Data Blue Sheet, 2002.

AMAYA, H., KONDO, K., HIRATA, H., UEDA, M., & MORI, T. Effect of chromium and molybdenum on corrosion resistance of super 13Cr martensitic stainless steel in CO2 environment. NACE International, Houston, TX (United States), 1998.

ANBURAJ. J., NAZIRUDEEN. S. S. M., NARAYANAN . R, ANANDAVEL . B, and CHANDRASEKAR. A: Ageing of forged superaustenitic stainless steel: Precipitate phases and mechanical properties. Materials Science and Engineering A 535, 99-107, 2012

ASM Handbook. 9, Metallography and Microstructures. ASM International, Materials Park, OH, v. 644, 2004.

ASM Speciality Handbook: Stainless Steels, ed. by J. R. Davis, ASM International, Materials Park, OH, 13, 1994.

ASTM G150-13. Standard Test Method for Electrochemical Critical Pitting Temperature Testing of Stainless Steels. Originally approved in 1997.

BANDY, R., CAHOON, J. R. Effect of composition on the electrochemical behavior of austenitic stainless steel in Ringer's solution.Corrosion, v. 33, n. 6, p. 204-208, 1977.

BARBOSA, Bruno. A. R .S., TAVARES, Sérgio. S. M., PARDAL, Juan. M., SILVA; Verônica. A. Influence of the solution annealing on corrosion resistance coating type clad of the 904L stainless steel (original in Portuguese). INTERCORR 2012, Salvador-BA, May, 2012.

BOSCH, C., & POEPPERLING, R. K. Influence of Chromium Contents of 0.5 to 1.0% on the Corrosion Behavior of Low Alloy Steel for Large Diameter Pipes in CO2 Containing Aqueous Media. In: CORROSION 2003. NACE International, 2003.

BURKE; P. A "Synopsis: Recent Progress in the Understanding of CO2 Corrosion", Advances in CO2 Corrosion, Vol. 1, NACE, pp. 3-9, Houston, TX, 1984

B. Weiss and R. Stickler, Metallurgical Transactions, Vol. 3, p.851, 1972.

CHARNG, T.; LANSING, F. Review of corrosion causes and corrosion control in a technical facility. NASA Technical Report, TDA Progress Report, p. 42-69, 1982.

CHILINGAR, G.V., MOURHATCH, R. and AL-QAHTANI, G. D. The Fundamentals of Corrosion and Scaling for Petroleum and Environmental Engineers. Houston: Gulf Publishing Company, 2008.

CHOI, Yoon-Seok; NESIC, Srdjan; YOUNG, David. Effect of impurities on the corrosion behavior of CO2 transmission pipeline steel in supercritical CO2− water environments. Environmental science & technology, v. 44, n. 23, p. 9233-9238, 2010.

COPPE - INSTITUTO ALBERTO LUIZ COIMBRA DE PÓS-GRADUAÇÃO E PESQUISA DE ENGENHARIA. Race to the sea: the technological and environmental challenges of the pre-salt. Available in:< http://www.coppe.ufrj.br/sites/default/files/coppe_pre-sal.pdf >. (original in Portuguese - access: November 2012).

COSTA & SILVA, André Luiz V., MEI, Paulo Roberto. Steels and special alloys (original in Portuguese), 2º Ed. Sumaré, SP: Blucher, 1988.

CUI, Z.D., WU, S.L., ZHU, S.L., YANG, X.J. Study on corrosion properties of pipelines in simulated produced water saturated with supercritical CO2. Applied Surface Science. Vol. 252, p. 2368-2374, 2006.

DA SILVA, M. J. G., HERCULANO, L. F., URCEZINO, A. S., ARAÚJO, W. S., de ABREU, H. F., & DE LIMA-NETO, P. Influence of Mo content on the phase evolution and corrosion behavior of model Fe–9Cr–xMo (x= 5, 7, and 9 wt%) alloys. Journal of Materials Research, v. 30, n. 12, p. 1999-2007, 2015.

DAS, G.S; KHANNA, A.S. Corrosion behaviour of pipeline steel in CO_2 environment. Trans, India institute. Met, vol. 57, nº 3, pp 277-281. July 2004.

DE WAARD, C.; LOTZ, U. Prediction of CO_2 corrosion of carbon steel. In:corrosion-national association of corrosion engineers annual conference. Nace, 1993.

DOSTAL, Vaclav; HEJZLAR, Pavel; DRISCOLL, Michael J. The supercritical carbon dioxide power cycle: comparison to other advanced power cycles.Nuclear technology, v. 154, n. 3, p. 283-301, 2006.

DUGSTAD, A; HEMMER, H and SEISESTEN, M. "Effect of steel microstructure on corrosion rate and protective iron carbonate film formation," Corrosion, Vol.57, pp.369-378, 2001

DUGSTAD, A; HEMMER, H & SEISESTEN, M. Effect of steel microstructure upon corrosion rate and protective iron carbonate film formation. In: CORROSION 2000. NACE International, 2000.

DUGSTAD, Arne; LUNDE, Liv; VIDEM, K. Influence of Alloying Elements upon the CO2 Corrosion Rate of Low Alloyed Carbon Steels, CORROSION'91, NACE International, , paper no. 473, Houston, TX, 1991.

DUGSTAD. Mechanism of protective film formation during CO2 corrosion of carbon steel. Corrosion, paper nº 31, 1998.

DUGSTAND, HEMMER. H, SEIERSTEN, M. Effect of steel microstructure on corrosion rate and protective Iron Carbonate film formation. Corrosion, vol. 57, nº 4, 2001.

DUTRA, Aldo Cordeiro; NUNES, Laerce de Paula. Cathodic protection (original in Portuguese). 3º ed. interciência publishing company, 1999.

EIDHAGEN. J, KIVISÄKK. U. Crevice corrosion properties for Sandvik SAF 3207^{TM} HD during injection of natural and chlorinated seawater. AB Sandvik Materials Technology, Tube R&D, Sandvik. Eurocorr conference, September 4-8:th, Stockholm, Sweden, 2011.

FERREIRA ITALIANO, Wilman E., DE LIMA-NETO, Pedro., ARAUJO, Walney. S., CARDOSO, Amanda. S., MIRADO, Hélio. C. Corrosion Behavior of nickel superalloy coatings in CO_2-saturated oil field formation water (original in Portuguese). Intercorr. Salvador, 2012.

FERREIRA, Pedro A. & FERREIRA, Cristiana V. M. "Myths and truths about CO_2 corrosion in oil and gas production systems - wells, pipelines and plants" (original in Portuguese). 7th COTEQ – from 09th to 12th of September, Florianópolis, Santa Catarina, Brazil, 2003

GALVELE, JOSE R. Pitting corrosion. Treatise on materials science and technology, v. 23, p. 1-57, 1983.

GENTIL, Vicente. Corrosion. 6th ed. Rio de Janeiro. technical and scientific books publishing company, 2011.

GILMAN, Jahn J. Hardening of high-chromium steels by sigma phase formation.Transactions of the American Society for Metals, v. 43, p. 161-192, 1951.

GOLDSCHMIDT, H. J. The structure of carbides in alloy steels. 1. General steel. Journal of The Iron and Steel Institute, v. 160, n. 4, p. 345-362, 1948.

GOMES SILVA; Victor. Evaluation of the stress corrosion susceptibility of the UNS S32750 super duplex stainless steel welded by orbital TIG process in Cl⁻, CO_2 and H_2S- containing media. (thesis in Portuguese). Universidade Federal Fluminense. Niterói, 2012.

GONTIJO, L. C., MACHADO, R., CASTELETTI, L. C., KURI, S. E., & DE PAULA NASCENTE, P. A. Comparison of the behavior of AISI 304L e AISI 316L stainless steel nitrided with plasma (original in Portuguese). Brazilian Journal of Vacuum Applications, v. 26, n. 3, 145-150, 2008.

GODDARD, Steven <stevengoddard.wordpress. /2010/09/05/the-freezing-point-and-the-dew point-part-2/> (acesse: January, 2015)

GRABKE, H. J. "The role of nitrogen in the corrosion of iron and steels." ISIJ international 36, no. 7, 777-786, 1996.

GUILLÉN NÚÑES, Milagros Mabel. Evaluation of corrosion behavior of the API 5LX70 and API 5LX80 steels in CO_2-containing medium by surface technique and electrochemical analysis (MSc thesis in Portuguese) Pontifícia Universidade Católica (PUC), Rio de Janeiro, 2006.

ISAACS, H., BECK, T. R., BERTOCCI, U., KRUGER, J., & SMIALOWSKA, S. Advances in localized corrosion. NACE. Houston, Texas, p.393, 1990.

KÄLLQVIST, J.; ANDRÉN, H.-O. Microanalysis of a stabilized austenitic stainless steel after long term ageing. Materials Science and Engineering: A, v. 270, n. 1, p. 27-32, 1999.

KERMANI, B., GONZALES, J. C., TURCONI, G. L., SCOPPIO, L., DICKEN, G., & EDMONDS, D. Development of superior corrosion resistance 3% Cr steels for downhole applications. In: CORROSION 2003. NACE International, 2003.

KERMANI, B., GONZALES, J. C., TURCONI, G. L., PEREZ, T. E., & MORALES, C. In-field corrosion performance of 3% Cr steels in sweet and sour downhole production and water injection. In: CORROSION 2004. NACE International, 2004.

KERMANI, B., GONZALES, J. C., TURCONI, G. L., PEREZ, T. E., & MORALES, C. Materials optimisation in hydrocarbon production. In: CORROSION 2005. NACE International, 2005.

KERMANI, M.B and MORSHED. A. Carbon dioxide corrosion in oil and gas production – A Compendium. Corrosion, vol 59. Nº 8, 2003.

KIMURA, M., SAKATA, K., & SHIMAMOTO, K. Corrosion resistance of martensitic stainless steel OCTG in severe corrosion environments. In: CORROSION 2007. NACE International, 2007.

KIMURA, Mitsuo., SAITO, Yoshiyuki., NAKANO, Yoshifumi. Effects of alloying elements on corrosion resistance of high strength linepipe steel in wet CO2 environment. NACE International, Houston, TX (United States), 1994.

LEWIS, A. C., BINGERT, J. F., ROWENHORST, D. J., GUPTA, A., GELTMACHER, A. B., & SPANOS, G. Two- and three-dimensional microstructural characterization of a super-austenitic stainless steel, in Materials Science and Engineering vol. 418, pp. 11-18 Washington, Sept. 2006.

Li HB, Jiang ZH, Yang Y, Cao Y, Zhang ZR. Pitting corrosion and crevice corrosion behaviors of high nitrogen austenitic stainless steels. International journal of minerals, metallurgy and materials, 31;16(5):517-24, 2009.

LING, S., CHOI, Y. S., NESIC, S. Effect of H2S on the CO2 corrosion of carbon steel in acid solutions. Electrochemica Acta. V. 56. pag. 1752-1760, 2011.

LISMER, R. E.; PRYCE, L.; ANDREWS, K. W. Occurrence of σ Phase in a High Chromium-Nickel Steel and the Effect of Carbon Content. J. Iron Steel Inst, v. 171, p. 49-58, 1952.

LIU, J., ZHANG, T., MENG, G., SHAO, Y., & WANG, F. Effect of pitting nucleation on critical pitting temperature of 316L stainless steel by nitric acid passivation. Corrosion Science, v. 91, p. 232-244, 2015

LOPEZ, D.A; PÉREZ, T; SIMISON, S. N. The influence of microstructure and chemical composition of carbon and low alloy steel in CO2 corrosion. A state of the art Appraisal, Materials and Design 24, pp561-575, 2003.

LOTO, Roland Tolulope. Pitting corrosion evaluation of austenitic stainless steel type 304 in acid chloride media. J. Mater. Environ. Sci, v. 4, n. 4, p. 448-459, 2013.

MALIK, A. U., SIDDIQI, N. A., AHMAD, S., & ANDIJANI, I. N. The effect of dominant alloy additions on the corrosion behavior of some conventional and high alloy stainless steels in seawater. Corrosion science, v. 37, n. 10, p. 1521-1535, 1995.

MITCHELL, D. R. G. Some applications of analytical TEM to the characterisation of high temperature equipment. Micron, v. 32, n. 8, p. 831-840, 2001.

MOISSEVA, L.S and KUKSINA, O.V. On the dependence of steel corrosion in oxigen-free aqueous media on pH and the pressure of CO2. Protection of metals, vol. 39, nº 5. pp 490-498. 2003.

MURRAY, J. L. ASM handbook: alloy phase diagrams, vol. 3. ASM, Metals Park, Ohio, v. 226, 1992.

NESIC, N; LUNDE, L. Carbon Dioxide Corrosion of Carbon Steel in Two Phase Flow. NACE international, Corrosion vol. 9. Nº 50, 1994.

NESIC, S., LUNDE, L. Carbon dioxide corrosion of carbon steel in two-phase flow. Corrosion, v. 50, n. 9, p. 717-727, 1994.

NESIC, S., POSTLETHWAITE, J., OLSEN, S. An electrochemical model for prediction of corrosion of mild steel in aqueous carbon dioxide solutions.Corrosion, v. 52, n. 4, p. 280-294, 1996.

NICE, Perry Ian., UEDA, Masakatsu. The effect of microstructure and chromium alloying content to the corrosion resistance of low-alloy steel well tubing in seawater injection service. NACE International, Houston, TX (United States), 1998.

NORDSVEEN, M; NESIC, S. A mechanistic model for carbon dioxide corrosion of mild steel in the presence of protective iron carbonate films – part 1: Theory and Verification. NACE international, Corrosion, p444-456, May, 2003.

NOSE, K., ASAHI, H., NICE, P. I., & MARTIN, J. W. Corrosion properties of 3% Cr steels in oil and gas environments. In: CORROSION 2001. NACE International, 2001.

NUNES, Laerce de Paula. Corrosion resistance Fundamentals (original in Portuguese). Rio de Janeiro: ABRACO, 2007.

OLIVEIRA SILVA, Paulo Maria. Influence of the cold deformation on microstructure, mechanical and magnetic properties, texture and pitting corrosion of AISI 316L and 301LN (MSc thesis in Portuguese), Federal University of Ceará, Fortaleza, 2005.

OUTOKUMPO. http://steelfinder.outokumpu.com (access: January 2015)

PADILHA, A. F; RIOS, P. R. Decomposition of austenitic stainless steel. ISIJ International. 325-337, April 2002.

PALACIOS, C. A.; SHADLEY, J. R. Characteristics of corrosion scales on steels in a CO2-saturated NaCl brine. Corrosion, v. 47, n. 2, p. 122-127, 1991.

PEAK OIL. peakoil.com/consumption/the cost of blunting peak oil (access: April 2013)

PETROBRAS. petrobras.com.br/en/our-activities/performance areas/oil and gas exploration and production/pre-salt/ (access: May 2015)

PETROBRAS/ CENPES. Water characterization collected in the Terminal tanks of São Sebastião (report 93 008-205/ in Portuguese): 4th collect. Technological Research Institute. São Paulo, 2007.

PICON, C. A., FERNANDES, F. A. P., TREMILIOSI-FILHO, G., RODRIGUES, C. A. D., & CASTELETTI, L. C. Study of pitting corrosion mechanism of supermartensitic stainless steels microalloyed with Nb and ti in sea water.Rem: Revista Escola de Minas, v. 63, n. 1, p. 65-69, 2010.

PISTORIUS, P. C.; BURSTEIN, G. T. Metastable pitting corrosion of stainless steel and the transition to stability. Philosophical Transactions of the Royal Society of London A: Mathematical, Physical and Engineering Sciences, v. 341, n. 1662, p. 531-559, 1992.

PLAUT, R. L., HERRERA, C., ESCRIBA, D. M., RIOS, P. R., & PADILHA, A. F. A short review on wrought austenitic stainless steels at high temperatures: processing, microstructure, properties and performance. Materials Research, v. 10, n. 4, p. 453-460, 2007

RAMÍREZ-LONDOÑO, A.J. Study of chromium nitride and sigma phase precipitation by thermal simulation of the heat affected zone in the multipass welding of duplex stainless steels (MSc thesis in Portuguese). University Polytechnic School of São Paulo: São Paulo. 1997.

REES, W. P.; BURNS, B. D.; COOK, A. J. Constitution of iron nickel chromium alloys at 650 °C to 800 °C. Journal of the iron and steel institute, v. 162, n. 3, p. 325-&, 1949.

REIS, Francisco Evaristo Uchôa. Evaluation of mechanical properties and corrosion resistance of alloys Model of 25Cr 6Mo 5Ni stainless steel with and without addition of boron (thesis in Portuguese), Federal University of Ceará, Fortaleza, 2015

ROTHMAN, S. J.; NOWICKI, L. J.; MURCH, G. E. Self-diffusion in austenitic Fe-Cr-Ni alloys. Journal of Physics F: Metal Physics, v. 10, n. 3, p. 383, 1980.

SCHMITT, G., & HORSTEMEIER, M. Fundamental aspects of CO_2 metal loss corrosion-Part II: Influence of different parameters on CO_2 corrosion mechanisms. In:CORROSION 2006. NACE International, 2006.

SCHMITT; G and HÖRSTEMEIER, M. FUNDAMENTAL aspects of CO_2 metal loss corrosion – part ii: influence of different parameters on CO_2 corrosion mechanisms. Corrosion NACExpo, 61st annual conference and exposition, 2006.

SCHMITT; G. "Fundamental Aspects of CO2 Corrosion", Advances in CO_2 Corrosion, Vol. 1, NACE, pp. 10-19, Houston, TX, 1984

SCHUBERT, Carsten. Investigation of the electrochemical corrosion behavior of a super duplex steel under extreme climatic conditions (Monograph in German), TU Bergakademie Freiberg, 2014.

SEDRIKS, A.J., Corrosion of Stainless Steels, 2a edição, Nova York: John Wiley & Sons Inc., 1996.

SEQUEIRA, C.A.C. Austenitic Stainless Steel for Desalination Processes, European Federation of Corrosion Publications, 33, pp. 97, 2001.

SINGHAL, L. K.; MARTIN, J. W. The formation of ferrite and sigma-phase in some austenitic stainless steels.Acta Metallurgica, v. 16, n. 12, p. 1441-1451, 1968.

SMITH, L., CELANT, M. Martensitic stainless steels in context. In: Supermartensitic, 2002, Bruxelas. In:*Anais.* Bruxelas, 2002. p. 14-20.

SONG, F. M. A comprehensive model for predicting CO2 corrosion rate in oil and gas production and transport systems, Electrochemica Acta. Vol. 55. pag. 689-700, 2010.

SONG, F. M., KIRK, D. W., GRAYDON, J. W., & CORMACK, D. E. CO_2 corrosion of bare steel under an aqueous boundary layer with oxygen. Journal of The Electrochemical Society, v. 149, n. 11, p. B479-B486, 2002.

SONG, F. M., KIRK, D. W., GRAYDON, J. W., & CORMACK, D. E. Predicting carbon dioxide corrosion of bare steel under an aqueous boundary layer.Corrosion, v. 60, n. 8, p. 736-748, 2004.

SONG, F. M; KIRK, D.W; GRAYDON, J.W; CORMACK, D.E. Prediction for CO_2 corrosion of active steel under a precipitate. Corrosion, paper nº 04382, 2004.

SPECIFICATION SHEET: Alloy 316/316L (http://www.sandmeyersteel.com, access: May 2015)

SPECIFICATION SHEET: Alloy 317/317L (http://www.sandmeyersteel.com, access: May 2015)

SPECIFICATION SHEET: Alloy 904L (http://www.sandmeyersteel.com, access: May 2015)

STEPHEN TAIT, W. An introduction to electrochemical corrosion testing for practicing engineers and scientists. Ed PairODocs Publications, 1994.

SUGIMOTO, K.; SAWADA, Y. The role of molybdenum additions to austenitic stainless steels in the inhibition of pitting in acid chloride solutions.Corrosion Science, v. 17, n. 5, p. 425-445, 1977.

TANAKA, H., MURATA, M., ABE, F., & IRIE, H. Microstructural evolution and change in hardness in type 304H stainless steel during long-term creep. Materials Science and Engineering: A, v. 319, p. 788-791, 2001.

TERADA, M., ESCRIBA, D. M., COSTA, I., MATERNA-MORRIS, E., & PADILHA, A. F. Investigation on the intergranular corrosion resistance of the AISI 316L (N) stainless steel after long time creep testing at 600 °C. Materials characterization, v. 59, n. 6, p. 663-668, 2008.

UEDA, M., & IKEDA, A. Effect of microstructure and Cr content in steel on CO2 corrosion. In: CORROSION 96. NACE International, 1996.

UEDA, M., & TAKABE, H. Effect of environmental factor and microstructure on morphology of corrosion products in CO2 environments. NACE International, Houston, TX (United States), 1999.

VACH, M., KUNÍKOVÁ, T., DOMÁNKOVÁ, M., ŠEVC, P., ČAPLOVIČ, Ľ., GOGOLA, P., & JANOVEC, J. Evolution of secondary phases in austenitic stainless steels during long-term exposures at 600, 650 and 800 °C. Materials Characterization, v. 59, n. 12, p. 1792-1798, 2008.

VILLANUEVA, D. E., JUNIOR, F. C. P., PLAUT, R. L., & PADILHA, A. F. Comparative study on sigma phase precipitation of three types of stainless steels: austenitic, superferritic and duplex. Materials science and technology. vol.22, nº 9, pp 1098-1104, 2006.

WASNIK, D. N., DEY, G. K., KAIN, V., & SAMAJDAR, I. Precipitation stages in a 316L austenitic stainless steel. Scripta Materialia, v. 49, n. 2, p. 135-141, 2003.

WILLENBRUCH, R. D., CLAYTON, C. R., OVERSLUIZEN, M., KIM, D., & LU, Y. An XPS and electrochemical study of the influence of molybdenum and nitrogen on the passivity of austenitic stainless steel. Corrosion science, v. 31, p. 179-190, 1990.

ZHANG, G. A and CHENG, Y. F. Localized corrosion of carbon steel in a CO2 – saturated oifield formation water. Electrochemica Acta. Vol. 56, pp 1676-1685, 2011.